Assessment and Prediction of the Transformation Kinetics Determining the Environmental Fate of Contaminants of Concern

Part I. Remediation of 1,2,3-Trichloropropane with Zerovalent Zinc

Part II. Prediction of the Environmental Fate of Novel Munitions Compounds

by

Alexandra J. Salter-Blanc

A DISSERTATION

presented to the Division of Environmental and Biomolecular Systems
and the Oregon Health & Science University
School of Medicine
in partial fulfillment of
the requirements for the degree of

Doctor of Philosophy
in
Environmental Science and Engineering

May 2014

School of Medicine

Oregon Health & Science University

CERTIFICATE OF APPROVAL

This is to certify that the PhD dissertation of

Alexandra J. Salter-Blanc

has been approved

_____

Paul G. Tratnyek, Thesis Advisor

Professor, Oregon Health & Science University

_____

Richard L. Johnson, Thesis Committee Member

Professor, Oregon Health & Science University

_____

Joseph A. Needoba, Thesis Committee Member

Assistant Professor, Oregon Health & Science University

_____

Eric J. Bylaska, Thesis Committee Member

Research Scientist, Pacific Northwest National Laboratory

Table of Contents

List of Tables

List of Figures

List of Abbreviations

1,2-DNB	1,2-dinitrobenzene
1,3-DNB	1,3-dinitrobenzene
1,4-DNB	1,4-dinitrobenzene
2-ADNT	2-amino-4,6-dinitrotoluene
2-CH_3-NB	2-methylnitrobenzene
2-CHO	2-nitrobenzylaldehyde
2,4-DANT	2,4-diamino-6-nitrotoluene
2,4-DNT	2,4-dinitrotoluene
2,6-DNT	2,6-dinitrotoluene
3-CH_3-NB	3-methylnitrobenzene
3-Cl-NB	3-chloronitrobenzene
3-$COCH_3$-NB	3-acetylnitrobenzene
4-ADNT	4-amino-2,6-dinitrotoluene
4-CH_2OH	4-nitrobenzyl alcohol
4-CH_3-NB	4-methylnitrobenzene
4-CHO	4-nitrobenzylaldehyde
4-Cl-NB	4-chloronitrobenzene
4-$COCH_3$-NB	4-acetylnitrobenzene
4-NH_2-NB	4-aminonitrobenzene
A	Arrhenius pre-exponential factor
a_s	specific surface area
B3LYP	an exchange-correlation functional

B3LYP*	a dataset (see text for context)
CCL3	Contaminant Candidate List 3
CL-14	5,7-diamino-4,6-dinitro-2,1,3-benzoxadiazol-1-ium-1-olate
CL-20	hexanitrohexaazaisowurtzitane
CoC	contaminant of concern
COSMO	a solvation model (COnductor-like Screening MOdel)
DFOB	desferrioxamine B
DFT	density functional theory
DI	deionized
DO	dissolved oxygen
DO/DI	deoxygenated/deionized water
$E_{(abs)}$	absolute potential
E^0	standard potential
E^0_H	absolute potential of the standard hydrogen electrode
E^1	one-electron reduction potential
$E^{1\prime}$	E^1 measured under standard environmental conditions
E^1_7	E^1 measured at pH 7
E^1_{NAC}	E^1 for nitroaromatic compound
E^1_{red}	E^1 for reductant
$E^1_{NAC,B3LYP*}$	E^1_{NAC} determined using the "B3LYP*" method (described in text)
EDS	electron-dispersive X-ray spectroscopy
E_{LUMO}	energy of the lowest unoccupied molecular orbital
EPA	U.S. Environmental Protection Agency

Fe(II)P	Fe(II) porphyrin
FER	free energy relationship
GC	gas chromatography
h	height
h	Planck's constant
HPLC	high performance liquid chromatography
I.D.	inner diameter
K	equilibrium constant
k'	pseudo-first-order rate constant
k_0	neutral hydrolysis rate constant
k_B	Boltzmann constant
k_{CoW7-}	rate constant for reduction by $Co^{(II)}W_{12}O_{40}^{7-}$
k_d	diffusion rate constant (Marcus theory)
K_d	equilibrium constant for precursor formation (Marcus theory)
k_{DFOB}	rate constant for reduction by DFOB
$k_{Fe(II)P}$	rate constant for reduction by Fe(II) porphyrin
k_H	acid hydrolysis rate constant
k_{JUG}	rate constant for reduction by juglone
k_{LAW}	rate constant for reduction by lawsone
k_M	mass normalized rate constant
$k_{M,B}$	k_M measured in batch reactor
k_{obs}	experimentally observed rate constant
$k_{obs,C}$	k_{obs} measured in column experiment

$k_{obs,C*}$	$k_{obs,C}$ predicted from $k_{M,B}$
k_{OH}	alkaline hydrolysis rate constant
K_{ow}	octanol-water partitioning coefficient
k_{red}	reduction rate constant
k_{SA}	surface area normalized rate constant
k_{tiron}	rate constant for reduction by tiron
LDA	an exchange-correlation functional
LFER	linear free-energy relationship
M06-2X	an exchange-correlation functional
M06-2X*	a dataset (see text for context)
MAD	mean absolute deviation
MC@	Meisenheimer complex formation at…
MCL	maximum contaminant level
MP2	Møller-Plessent perturbation theory, second order
M_s	mass dry solid (for determining bulk density)
n	number of electrons
n	order of the reaction
NAC	nitroaromatic compound
NB	nitrobenzene
NMR	nuclear magnetic resonance
NOM	natural organic matter
NTO	3-nitro-1,2,4-triazole-5-one
nZVI	nano zerovalent iron

ORP	oxidation-reduction potential
PA@	proton abstraction at…
PAR	property activity relationship
PATO	3-picryl amino 1,2,4-triazole
PAX-21	Picatinny Arsenal Explosive 21
PBE	an exchange-correlation functional
PHG	public health goal
PRB	permeable reactive barrier
PVC	polyvinyl chloride
Q	volumetric flow rate
QSAR	quantitative structure-activity relationship
R	gas constant
r	radius
RMSD	root mean square deviation
SAR	structure activity relationship
SCE	saturated calomel electrode
SHE	standard hydrogen electrode
SMD	a solvation model—(Solvation Model D, D = density)
SSA	specific surface area
Sub@	direct nitro substitution at…
S_w	aqueous solubility
SWM	Site Water “M”
SWP	Site Water “P”

SWQ	Site Water "Q"
T	temperature
t	time
TCE	trichloroethylene
TCP	1,2,3-trichloropropane
$[TCP]_0$	TCP concentration at $t = 0$
$[TCP]_{eff}$	TCP concentration of column effluent
$[TCP]_{inf}$	TCP concentration of column influent
TEM	transmission electron microscopy
TNT	2,4,6-trinitrotoluene
t_R	residence time
$v(t)$	reaction rate
V_c	volume of column
VOC	volatile organic compound
V_s	volume occupied by solid (for determining bulk density)
V_w	volume of water in column
W	electrostatic term in the Marcus equation
XPS	X-ray photoelectron spectroscopy
XRD	X-ray diffraction
Z	universal frequency factor (Marcus theory)
Zn1210	Zinc Powder 1210 (Horsehead Corporation)
Zn1239	Zinc Powder 1239 (Horsehead Corporation)
Zn64	Zinc Dust 64 (Horsehead Corporation)

ZVI	zerovalent iron
ZVM	zerovalent metal
ZVZ	zerovalent zinc
γ	tangent (to the Marcus curve)
ΔG° or ΔG°_{rxn}	standard molar free energy of the reaction
$\Delta G^{\circ\prime\prime}$	corrected standard molar free energy of the reaction
$\Delta G^{\circ\ddagger}$	standard molar free energy of activation
$\Delta G^{\circ\prime}_{B3LYP*}$	$\Delta G^{\circ\prime\prime}$ determined using $E^1_{NAC,B3LYP*}$
$\Delta H^\ddagger$	molar enthalpy of activation
$\Delta S^\ddagger$	molar entropy of activation
η	porosity
λ	reorganization energy
ρ_a	surface area concentration
ρ_d	bulk density
ρ_M	mass concentration
$\rho_{M,C}$	ρ_M in column
ρ_s	specific density
σ	Hammett parameter

Acknowledgements

First and foremost, I would like to thank my advisor Dr. Paul G. Tratnyek for his mentorship, encouragement, and approachability, and for all the opportunities he has provided me throughout the course of this work. I also owe special thanks to Dr. James T. Nurmi and Dr. Richard L. Johnson for their scientific contributions, advice, and technical assistance over the years. I am also indebted to those who have contributed to this work, including Dr. Eric J. Bylaska, the NESDI project team—particularly Dr. Eric J. Suchomel, and two summer interns: Julia J. Ritchie and Hayley Johnston. In addition, I am thankful to my committee members—Drs. Paul G. Tratnyek, Richard L. Johnson, Eric J. Bylaska, and Joseph A. Needoba—for their time in reviewing this dissertation. I am also grateful for all the input and support from fellow students Amanda Mather, Dimin Fan, and Miranda Bradley, and all the people who have passed through the Tratnyek lab in my time at OHSU.

This work was supported by the Strategic Environmental Research and Development Program (SERDP) and the Navy Environmental Sustainability Development to Integration Program (NESDI). Details regarding these contributions are given throughout this work, as appropriate. I also received support as an OHSU Graduate Research Scholar during the 2013-2014 academic year.

I am at this point in my educational career because of the enthusiasm and encouragement of my many science teachers and professors. I owe particular thanks to my undergraduate advisor, Dr. R. Carlisle Chambers, for believing in my potential, providing me with my first research opportunity, and encouraging my continued scientific pursuits. On a personal note, I would like to thank my parents, grandparents,

and great aunts for all the love and support they have given me over the years. Finally, I am immensely grateful to my husband, Andy, for his love, encouragement, support, and sacrifice, especially in the months since the birth of our beautiful daughter, Leah. He makes it possible for me to achieve so much more than I could alone.

Abstract

Assessment and Prediction of the Transformation Kinetics Determining the Environmental Fate of Contaminants of Concern:
Part I. Remediation of 1,2,3-Trichloropropane with Zerovalent Zinc
Part II. Prediction of the Environmental Fate of Novel Munitions Compounds

Alexandra J. Salter-Blanc

Doctor of Philosophy
Division of Environmental and Biomolecular Sciences within
the Institute of Environmental Health
School of Medicine
Oregon Health & Science University

May 2014
Thesis Advisor: Paul G. Tratnyek

The environmental fate of contaminants of concern (CoCs) is controlled—in part—by chemical degradation reactions. Often these reactions are not well understood, hindering efforts to limit associated risks to human health and the environment. In this study, the kinetics of CoC degradation are studied with respect to addressing two aspects of contamination mitigation: remediation and prevention. Part I concerns the legacy and emerging contaminant 1,2,3-trichloropopane (TCP) and the prospects for remediating contaminated groundwater by reduction (i.e., dechlorination) with zerovalent zinc (ZVZ). Part II concerns the development of kinetic models to evaluate the environmental persistence of novel energetic compounds under consideration for use in munitions formulations.

Part I—The kinetics of TCP reduction by ZVZ were studied in both bench-top and pilot-scale experiments in order to evaluate the prospects for treating TCP-contaminated groundwater with ZVZ. The kinetics of the reaction were found to be highly dependent on solution chemistry, especially pH and the presence of certain groundwater constituents. The results indicated that this influence is related to morphological and solubility-related changes to a ZnO shell on the surface of the ZVZ. The kinetics of TCP reduction using commercially-available, industrial-grade ZVZ were measured in batch-reactor and column experiments and, in most cases, found to be on the order of those produced by more expensive reagent-grade materials. The results of material testing were used to design and execute large, pilot-scale column experiments comparing the use of two ZVZ formulations at a TCP-contaminated site. Analysis of TCP removal kinetics during column operation, and assessment of the column fill material post-operation, support the viability of ZVZ for treating TCP-contaminated groundwater in an engineered treatment system such as a permeable reactive barrier.

Part II—Progress was made toward developing models to predict the environmental degradation kinetics of energetic nitroaromatic compounds (NACs) by two fate processes, alkaline hydrolysis and reduction. For alkaline hydrolysis, it was determined that model development is hindered by lack of understanding regarding reaction mechanisms. To address this, potential mechanisms for 2,4,6-trinitrotoluene (TNT) and 2,4-dinitroanisole (DNAN) were evaluated using coordinated experimental kinetic measurements and molecular modeling calculations. The results suggest that the initial step in alkaline hydrolysis is Meisenheimer complex formation or abstraction of a methyl proton for TNT and Meisenheimer complex formation for DNAN.

For the reduction pathway, a predictive model in the form of a free energy relationship (FER) based on the Marcus theory of outer-sphere electron transfer was developed. The FER relates the rate constant for NAC reduction to the free energy of the reaction, which was calculated from one-electron reduction potentials (E^1) determined using molecular modeling. The FER accurately describes NAC reduction kinetics for non-energetic compounds. The model was found to accurately predict newly measured rate constants for TNT and 2,4-dinitrotoluene, but not for DNAN. The inconstancy of the DNAN results was proposed to be related to the calculation of E^1.

Chapter 1. Introduction: Kinetics of Environmental Organic Contaminant Transformation

Organic contaminants are present in the environment, often as a result of anthropogenic activities. In some cases, these contaminants pose known or potential threats to ecosystems and/or to human health, in which case they are termed "contaminants of concern" (CoCs). CoCs in the environment are subject to a number of physical and chemical processes that determine their fate. These processes control the transport of CoCs within and between different media and the transformation of CoCs in chemical reactions.

Information regarding CoC fate can be gained by studying the kinetics of reactions affecting CoCs in the environment. The study of kinetics involves understanding the rate at which chemical reactions take place and the factors affecting these rates. It also often involves examination of the mechanisms and products of the reactions. Understanding the kinetics of relevant reactions gives information about the persistence of CoCs in the environment that is useful, for instance, in developing strategies to remediate existing contamination and informing decisions aimed at avoiding future contamination.

This chapter gives an overview of the study of CoC transformation kinetics, with particular emphasis on processes relevant to organic contaminants in groundwater systems. It gives background on (*i*) the description of reaction kinetics, (*ii*) environmental factors influencing CoC reaction rates, (*iii*) measurement of reaction rates in the laboratory, (*iv*) normalization of rate constants to facilitate comparison, and (*v*) the theory

and practice of predicting reaction rates. Aspects particularly relevant to this dissertation are highlighted throughout.

1.1 Rates of Chemical Reactions

1.1.1. Reaction Rate, Definition

For the reaction,

$$aA + bB \rightarrow cC + dD \tag{1.1}$$

where capital letters represent reactant and product species and lower-case letters represent stoichiometric coefficients, the rate of the reaction ($v(t)$) is defined as

$$v(t) = -\frac{1}{a}\frac{d[A]}{dt} = -\frac{1}{b}\frac{d[B]}{dt} = \frac{1}{c}\frac{d[C]}{dt} = \frac{1}{d}\frac{d[D]}{dt} \tag{1.2}$$

where molar concentrations are denoted as capital letters in brackets (*1, 2*). At constant temperature, $v(t)$ is proportional to the concentrations of the chemical species present at time t. This relationship is represented as a rate law, which generally takes the form

$$v(t) = k[A]^{\alpha}[B]^{\beta}\cdots \tag{1.3}$$

where k is the rate constant for the reaction and α, β, $\cdots$ are the order of the reaction with respect to each species (i.e., the reaction is α^{th} order in A, β^{th} order in B, etc.) (*2*). The overall order of the reaction, n, is equal to $\alpha + \beta + \cdots$. k has units of $(\text{concentration})^{1-n}$ $(\text{time})^{-1}$. Under most circumstances n and k must be determined experimentally (*1*). In practice, n and k are usually determined by analyzing plots of the change of concentration of a chemical of interest (e.g., "A") over time.

1.1.2. Experimental Determination of Reaction Order and Rate Constant

While n can be any integer or fraction, in most processes, elementary reactions are described as zero-, first-, or second-order. Zero-order reactions depend only on k, and are independent of the concentration of the reactant. First-order and second-order reactions depend on k and the concentration the reactant(s). Table 1.1 summarizes rate laws for each of these reaction orders along with other details. Included in Table 1.1 are:

- Rate laws for zero-, first-, and second-order reactions.
- Integrated rate laws for use in fitting concentration vs. time data to obtain k.
- Diagnostic plots on which data can be fit to a straight line, if the reaction is of the specified order.
- Units of k.
- Equations for determining the time required for half of the initial concentrations to be consumed (the half-life, $t_{1/2}$).

As seen in Table 1.1, the equations describing $v(t)$ become increasingly complex with increasing order, especially for second order reactions involving two different reactants (i.e., $A + B \xrightarrow{k} C$, where k is the second-order rate constant). In some cases, this complexity can be overcome with the pseudo-first-order approximation. If $[B]_0$ can be considered to be at steady-state (e.g, if it is sufficiently in excess of $[A]_0$) consumption of B will be negligible and [B] will not change significantly over the course of the reaction. [B] can therefore be treated as a constant and factored into k (*3, 4*). The resulting rate constant, k', is defined as

$$k' = k[B] \tag{1.4}$$

and the rate law for the reaction can be written as

$$\frac{d[A]}{dt} = -k'[A] \tag{1.5}$$

where k' is the pseudo-first-order rate constant. k can then be calculated from k' using Equation 1.4 and assuming $[B] = [B]_0$. Additionally, if k' is determined at multiple $[B]_0$, a plot of k' vs. $[B]_0$ can be fit to a straight line having a slope of k and an intercept of 0 (i.e., $k' = 0$ at $[B]_0 = 0$).

Table 1.1. Summary of information regarding reaction orders. $[A]_0$ and $[B]_0$ are the concentrations of [A] and [B] at t = 0 (*1, 4, 5*).

	Zero order	**First order**	**Second order**
Reaction	$A \xrightarrow{k} P$	$A \xrightarrow{k} P$	$A + A \xrightarrow{k} P$ $A + B \xrightarrow{k} P$
Rate law	$\frac{d[A]}{dt} = -k$	$\frac{d[A]}{dt} = -k[A]$	$\frac{d[A]}{dt} = -k[A]^2$ $\frac{d[A]}{dt} = -k[A][B]$
Integrated rate law	$[A] = [A]_0 - kt$	$[A] = [A]_0 e^{-kt}$	$[A] = \frac{[A]_0}{1 + k[A]_0 t}$ $\ln\left(\frac{[A]}{[B]}\right) = ([A]_0 - [B]_0)kt + \ln\left(\frac{[A]_0}{[B]_0}\right)$
Experimental straight line plot	[A] vs. t	ln[A] vs. t [a]	1/[A] vs. t ln([A]/[B]) vs. t [b]
Units of *k*	$M\ s^{-1}$	s^{-1}	$M^{-1}\ s^{-1}$
Half life determination	$t_{1/2} = \frac{[A]_0}{2k}$	$t_{1/2} = \frac{\ln(2)}{k}$	$t_{1/2} = \frac{1}{k[A]_0}$ $t_{1/2}(A) = \frac{1}{k([A]_0 - [B]_0)} \ln \frac{[B]_0}{2[B]_0 - [A]_0}$

a) or log[A] vs. t

b) or log([A]/[B]) vs. t

1.1.3. Experimental Determination of Rate Constants for Complex Reactions

In some cases, the kinetics of the disappearance of a CoC are not well described by zero-, (pseudo-)first-, or second-order models. This is often due to the disappearance of the CoC being affected by multiple elementary reactions. Three examples are given below although others have been detailed previously (e.g., ref. (*1*)).

Reactions in series. A simple case of reactions in series is the overall reaction

$$\mathrm{A} \xrightarrow{k_1} \mathrm{B} \xrightarrow{k_2} \mathrm{C}$$

in which each elementary reaction is first-order. In this reaction the rate of change, or disappearance, of A depends on [A] and k_1 according to Equation 1.6.

$$\frac{d[\mathrm{A}]}{dt} = -k_1[\mathrm{A}] \tag{1.6}$$

The rate of change of B, however, is affected by both the formation of B (which is the product of the disappearance of A) and the disappearance of B to form C. The rate of change for B is described as follows,

$$\frac{d[\mathrm{B}]}{dt} = k_1[\mathrm{A}] - k_2[\mathrm{B}] \tag{1.7}$$

In order to determine k_1 and k_2 from a plot of [B] vs. t, the data can be fit to the following analytical solution to Equations 1.6 and 1.7 (*6*)

$$[B] = \frac{k_1[A]_0}{k_2 - k_1}\left(e^{-k_1 t} - e^{-k_2 t}\right) \tag{1.8}$$

Alternatively, concentration vs. time data can be fit with the differential equations defining [A] and [B] directly using numerical methods(*7*). This is useful, for instance, if concentration vs. time data is available for species A but not species B. An example of an

environmentally relevant series of reactions is the sequential dechlorination of the CoC carbon tetrachloride (*8*).

Reactions in parallel. In some cases, the chemical fate of a CoC is affected by multiple, simultaneous reactions. A simple case is the reaction of A with B or C to form the products P_1 and P_2 (*6*):

$$A + B \xrightarrow{k_1} P_1 \qquad \text{(Scheme 1.1)}$$

$$A + C \xrightarrow{k_2} P_2 \qquad \text{(Scheme 1.2)}$$

For these reactions, the disappearance of A and appearance of P_1 and P_2 are described by the following differential equations:

$$\frac{d[A]}{dt} = -\left(k_1[B] + k_2[C]\right)[A] \qquad (1.9)$$

$$\frac{d[P_1]}{dt} = k_1[A][B] \qquad (1.10)$$

$$\frac{d[P_2]}{dt} = k_2[A][C] \qquad (1.11)$$

Fitting of concentration vs. time data (for the disappearance of A, or for the appearance of P_1 and P_2) is most easily determined using numerical methods. However, analytical solutions to the differential equations are available (*1*) if the reactions can be treated as first-order based on the pseudo-first-order approximation. Modeling reactions in parallel can be useful in determining the dominant pathway in competing reaction processes. An example of competing reaction processes are the dechlorination of trichloroethylene (TCE) by hydrogenolysis or reductive β-elimination (*9, 10*).

Reversible reactions. Some environmental reactions are affected by reversible reaction kinetics. A simple case is,

$$\mathrm{A} \underset{k_{-1}}{\overset{k_1}{\rightleftharpoons}} \mathrm{B} \qquad \text{(Scheme 1.3)}$$

where k_1 and k_{-1} are the rate constants for the forward and reverse processes. In cases where the system is far from equilibrium, the reversible portion of the reaction can often be ignored because the concentration of B is small (*6*). In cases close to equilibrium, the reverse process becomes significant and the rates of change of A and B are defined as,

$$\frac{d[\mathrm{A}]}{dt} = -\frac{d[\mathrm{B}]}{dt} = -k_1[\mathrm{A}] + k_{-1}[\mathrm{B}] \qquad (1.12)$$

which can be integrated to obtain

$$[\mathrm{B}] = \frac{k_1[\mathrm{A}]_0}{k_1 + k_{-1}}\left(1 - e^{-(k_1+k_{-1})t}\right) \qquad (1.13)$$

An example of a reversible reaction (as part of a series of reactions) is the alkaline hydrolysis of TNT. In Chapter 5 (and ref. (*11*)) it is hypothesized that this reaction proceeds according to the following set of elementary reactions,

$$\mathrm{TNT} + \mathrm{OH^-} \underset{k_{-1}}{\overset{k_1}{\rightleftharpoons}} \mathrm{P1} \xrightarrow{k_2} \mathrm{P2} \qquad \text{(Scheme 1.4)}$$

where P1 is the first product, P2 is the second product, k_1 is the second-order rate constant for the forward portion of the first reaction, k_{-1} is the rate constant reverse portion of the first reaction, and k_2 is the rate constant for the second reaction. In the experiments described in Chapter 5 (and ref. (*11*)), disappearance of TNT is measured in a pH-buffered system (i.e., $[OH^-]$ is assumed to be constant), so the forward reaction of TNT to P1 is treated with the pseudo-first-order approximation to obtain:

$$\text{TNT} \underset{k_{-1}}{\overset{k_{1,obs}}{\rightleftharpoons}} \text{P1} \xrightarrow{k_2} \text{P2} \qquad \text{(Scheme 1.5)}$$

where $k_{1,obs}$ is the observed pseudo-first-order rate constant for formation of P1. The kinetics for this process are then fit to the following differential equations

$$\frac{d[\text{TNT}]}{dt} = -k_{1,obs}[\text{TNT}] + k_{-1}[\text{P1}] \qquad (1.14)$$

$$\frac{d[\text{P1}]}{dt} = k_{1,obs}[\text{TNT}] - k_{-1}[\text{P1}] - k_2[\text{P1}] \qquad (1.15)$$

using numerical methods (which were used to facilitate global fitting of certain constants). Analytical solutions to the differential equations describing reversible reactions available for the example described (*12*) and certain other reversible reactions (*7*).

1.2. Other Factors Affecting Reaction Rates in Natural Environments

1.2.1. Temperature

Temperature is an environmental factor that can significantly influence the rates of chemical reactions. The range of temperature variation in groundwater is typically small, but may be altered in certain engineered remediation systems. The effect of temperature on k is usually described by the Arrhenius equation (*4, 7*),

$$k = A \cdot e^{-E_a/RT} \qquad (1.16)$$

where A and E_a are the Arrhenius parameters (specifically, the pre-exponential factor (A) and the activation energy (E_a)), R is the ideal gas constants, and T is temperature. A is given the same units as the rate constant. Equation 1.16 can also be written as

$$\ln k = \ln A - \frac{E_a}{RT} \tag{1.17}$$

or

$$\log k = \log A - \frac{E_a}{2.303RT} \tag{1.18}$$

Conventionally, Equation 1.17 or 1.18 are used to fit plots of ln(k) or log(k) vs. T^{-1} (Arrhenius plots) in order to determine the Arrhenius parameters (e.g., in a plot of ln(k) vs. T^{-1}, the slope is equal to $-E_a/RT$ and the intercept is equal to ln(A)). Alternatively, the Arrhenius parameters can be determined using nonlinear fitting of Equation 1.16 directly.

An example of an Arrhenius plot displaying data from Chapter 5 (and ref. (*11*)) is given in Figure 1.1. In Figure 1.1, measured data for the alkaline hydrolysis of TNT (*11*) is compared to data gathered from the literature (*13, 14*). The combined data are fit to Equation 1.17 in order to determine A and E_a, which describe the effect of temperature on k.

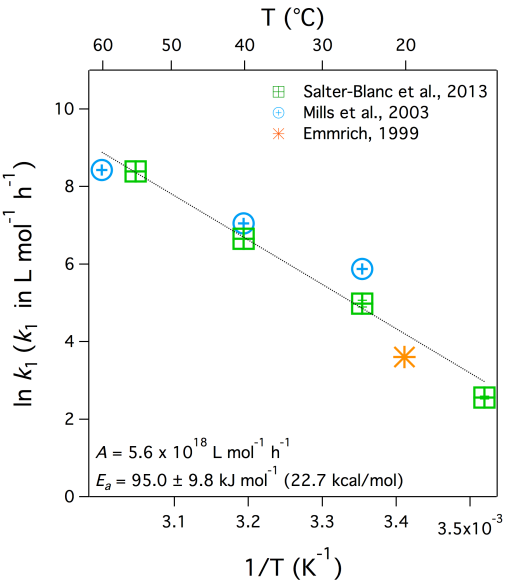

Figure 1.1. Arrhenius plot for the alkaline hydrolysis of TNT as reported by various sources (*11, 13, 14*) with a linear fit to the combined data. The corresponding Eyring plot is discussed in Chapter 5.

1.2.2. pH

The kinetics of many environmental reactions can be highly sensitive to pH. One important reaction pathway that shows particular sensitivity to pH is hydrolysis. Hydrolysis is defined as the reaction of an organic molecule with water, resulting in cleavage of a carbon bond to a leaving group (X) and formation of a new carbon-oxygen bond, typically resulting in direct displacement of X by OH (*15*). Hydrolysis is affected by three processes, (*i*) nuceophilic attack by water ("neutral hydrolysis"), (*ii*) catalysis of this process by the hydronium ion (H^+) at sufficiently acidic pH ("acid hydrolysis"), and (*iii*) nucleophilic attack by the hydroxide ion (OH^-) at sufficiently alkaline pH ("alkaline hydrolysis").

Because $[H^+]$ and $[OH^-]$ normally do not change significantly over the course of the reaction, hydrolysis reactions are generally treated as pseudo-first-order (*15*), therefore the following rate law can be written

$$\frac{d[\mathrm{RX}]}{dt} = -k_{obs}[\mathrm{RX}] \tag{1.19}$$

where k_{obs} is the observed rate of the reaction. k_{obs} in this case is dependent on the three processes affecting disappearance of the CoC. This dependence is shown in Equation 1.20,

$$k_{obs} = k_{\mathrm{H}}[\mathrm{H}^+] + k_0 + k_{\mathrm{OH}}[\mathrm{OH}^-] \tag{1.20}$$

where k_{H} is the rate of acid hydrolysis, k_0 is the rate of neutral hydrolysis, and k_{OH} is the rate of alkaline hydrolysis.

An example of a plot of log k_{obs} vs. pH for the hydrolysis of the CoC *tert*-butyl formate (a degradation product of methyl *tert*-butyl ether (MTBE)) is shown in Figure 1.2 (*16*). This example shows a U-shaped plot where the bottom of the U is defined by k_0.

Such plots may also be V-shaped if k_0 is smaller than the point at which the lines representing acid and alkaline hydrolysis cross.

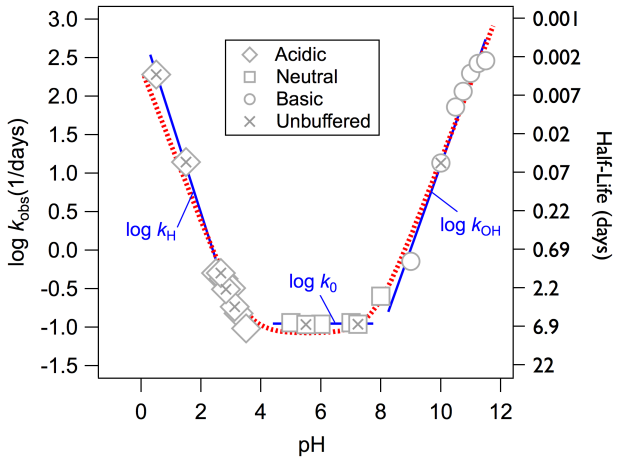

Figure 1.2. Kinetics of the hydrolysis of *tert*-butyl formate showing the effect of pH on k_{obs}. Solid blue lines are separate linear regressions of data in regions primarily influenced by k_H, k_0, or k_{OH}. The red dashed line is a nonlinear regression on all of the data. Adapted with permission from Church et al., 1999 (*16*). Copyright 1999 SETAC.

Another group of environmentally relevant reactions that show sensitivity to pH are reduction reactions involving zerovalent metals (ZVMs) such as ZVI and ZVZ. The reductive reactivity of ZVMs is highly influenced by corrosion of the metal and the presence and morphology (e.g., thickness, uniformity, etc.) of oxide shells. Both corrosion and oxide shell solubility are highly affected by pH. One example of this is the pH dependence of k_{obs} for the reduction of carbon tetrachloride by ZVI (*8*). Experiments show that k_{obs} for this process decreases with increasing pH in the pH range of 5-10 (Figure 1.3). It is hypothesized that this trend is related to oxidative dissolution (i.e., corrosion) of the iron (*8, 17*).

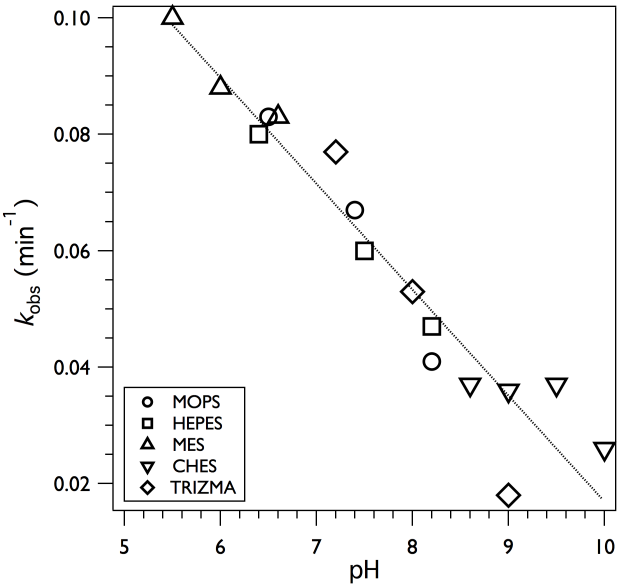

Figure 1.3. Effect of pH on rate constants for the degradation of carbon tetrachloride by ZVI measured in buffered solutions. Adapted with permission from Matheson and Tratnyek, 1994 (*8*). Copyright 1994 American Chemical Society.

Another example is the reduction of 1,2,3-trichloropropane (TCP) by ZVZ (*18*). In this case the k_{obs} vs. pH trend is U-shaped with a minimum from a pH of about 8-10 with increased k_{obs} at higher and lower pH (Figure 1.4A). Comparison of this trend with zinc corrosion trend (not shown) and the zinc oxide (ZnO) solubility trend (Figure 1.4B) show that the k_{obs} trend is most similar to the ZnO solubility trend (*18*). This suggests k_{obs} is highly influenced by solubility related changes to the ZnO shell on the ZVZ particles (*18*). Further discussion on these observations can be found in Chapter 2.

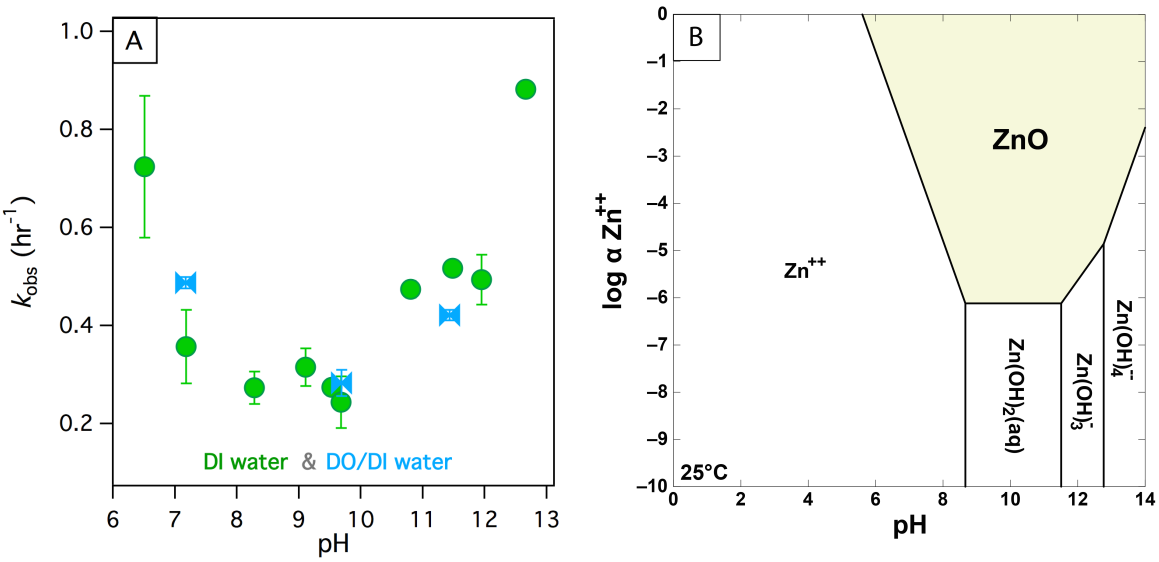

Figure 1.4. (A) Observed reaction rate constants (k_{obs}) versus pH for reduction of TCP by ZVZ in DI water and deoxygenated DI water (DO/DI water) (see Chapter 2 or ref. (*18*) for more details). (B) Solubility diagram for Zn^{2+} solid species in DI water. Adapted with permission from Salter-Blanc and Tratnyek, 2011 (*18*). Copyright 2011 American Chemical Society.

1.2.3. Co-contaminants and Groundwater Solutes

Many environmental organic reactions relevant to groundwater systems are initially studied in deionized (DI) water in order to avoid species interactions affecting the reaction kinetics. However, in natural and engineered remediation systems, these reactions take place in the presence of various groundwater constituents and, at times, co-contaminants. These solutes play a particularly important role in reactions involving ZVMs because of influences on the formation, dissolution, or attack of passivating oxide shells and/or the availability of active sites. The influence of these solutes on the reduction of CoCs by ZVMs is often complex and has been subject to a great deal of investigation. These investigations typically focus on ZVI, as it is the most commonly used ZVM in engineered remediation solutions.

Studies of ZVI reduction of trichloroethylene (TCE) have shown decreased reaction rates in the presence of co-contaminants chromate and nitrate, likely due to competitive reduction (*19, 20*). Decreased rates of chlorinate solvent reduction have also been measured in the presence of natural organic mater (NOM) (*21*), and silica (*21-23*) due to adsorption to the metal surface. Mixed results (both increased and decreased rates) have been observed in the presence of various carbonate species (*21, 24, 25*) and sulfate (*20, 25*). These species are thought to either form protective salts on the surface of the ZVI or to promote dissolution of iron oxide passive films (*20*). Chloride has been observed to increase rates of CoC reduction by ZVI (*25*) presumably due to removal of passivating oxides and promotion of pitting corrosion (*26*), but its long-term effects are somewhat unclear (*21*).

Chapter 2 of this dissertation explores the effects of groundwater solutes on ZVZ reduction of the chlorinated solvent TCP. The application of these findings to field-scale remediation is explored in Chapters 3 and 4.

1.2.4. Electron Transfer Mediators in Redox Reactions

Environmental redox reactions are sometimes catalyzed by substances that shuttle electrons between a bulk electron donor and the CoC. These catalysts are known as electron transfer mediators or electron shuttles (*27, 28*). A scheme showing the flow of electrons in a typical mediated CoC reduction reaction is shown below.

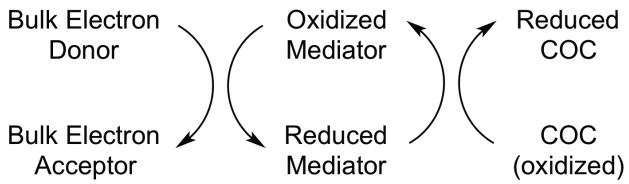

This process requires that (*i*) the overall reaction (reduction of the CoC by the bulk donor) be energetically favorable, (*ii*) both steps in the reaction be energetically favorable (i.e., the reduction potential of the mediator must fall between the values for the electron donor and CoC), and (*iii*) both steps in the reaction must be kinetically fast compared to the unmediated reaction between the electron donor and CoC (*29*).

Generally, the kinetics of a mediated reduction reaction are observed to be second order in the concentration of the CoC and reduced mediator. Because the bulk electron donor continuously reduces the mediator, it can be assumed that the rate of change of the mediator concentration is zero (by the steady-state approximation). The concentration of the mediator can be treated as a constant and the kinetics can be treated with the pseudo-first-order approximation.

Many electron transfer mediators have been studied with regard to the reduction of nitroaromatic compounds (NACs). These include (*i*) model quinone species juglone (*30-32*), lawsone (*30*), and anthrahydroquinone-2,6-disulfonate monophenolate (*33*), (*ii*) Fe(II) adsorbed to iron oxides (*31, 32*), and (*iii*) the biologically-relevant (and model environmental mediator) iron porphyrin (*30*). The kinetics of NAC reduction by juglone, lawsone, and iron porphyrin is explored in more detail in Chapter 6.

1.3. Measuring Rate Constants in the Laboratory

1.3.1. Batch Reactor Experiments

Kinetic analysis of CoC reactions is often performed under relatively controlled laboratory conditions in what are known as batch reactors. The term batch reactor can be used to describe a wide range of experimental setups, but typical usage of the term in the environmental literature refers to closed, no-flow experiments (*7*) often performed in small bottles or serum vials (usually 10-300 mL). A basic setup involves an aqueous phase (e.g., DI water, buffer, site water) with some concentration of CoC. Reagent additions or changes to temperature conditions can be made to test various effects. Over the course of the experiment, aliquots of the aqueous or gaseous phases are removed and analyzed to determine the concentration of CoC at a given time. The results are than be plotted on a concentration vs. time plot and analyzed to determine *k*.

There are many advantages to measuring kinetics in batch reactors. One major advantage is the ability to control variables to a high degree. This facilitates the study of many different reaction conditions and allows the researcher to limit complicating variables. The experiments can also be performed relatively quickly, often on the scale of hours to weeks. In addition, the experiments require only small quantities of reagents making them relatively inexpensive compared to column experiments (described below). A disadvantage of batch reactor experiments when studying groundwater processes is that they do not closely mimic field conditions. They are, however, well suited for studying fundamental kinetic processes because of the degree to which variables can be controlled.

1.3.2. Column Experiments

Column experiments are a useful tool for studying chemical kinetics in a system that more closely mimics groundwater conditions. These experiments consist of columns filled with material representative of the system of interest (e.g., naturally occurring sediments or material for use in engineered treatment system, such as ZVI which is often used in permeable reactive barriers (*34*)). An aqueous phase is then pumped across the column. The concentration of CoC is measured in the column effluent and, ideally, in aliquots removed from ports along the length of the column. k can be determined from concentration vs. time plots where time is the residence time (t_R) at the position of sampling.

t_R can be determined from the following equation

$$t_R = \frac{V_w}{Q} \tag{1.21}$$

where V_w is the volume of water in the column and Q is the volumetric flow rate. V_w can be determined gravimetrically, when feasible, by taking the difference in the weight of the column before and after the addition of water (and making an appropriate assumption about the weight of water on a per-mL basis). Alternatively, V_w can be calculated based on the column packing material porosity (η) and the volume of the column (V_c) according to the following equations,

$$V_w = \eta \cdot V_c \tag{1.22}$$

$$\eta = 1 - \frac{\rho_d}{\rho_s} \tag{1.23}$$

where ρ_d and ρ_s are the bulk density and specific density of the packing material. ρ_d is an empirical quantity determined for the material based on the following equation,

$$\rho_d = \frac{M_s}{V_t} \tag{1.24}$$

where M_s is the mass of dry solid and V_t is the total volume (including pore space) occupied. More detailed determination and analysis of t_R can be performed using tracer tests (e.g., (*35*)).

1.4. Normalizing and Comparing Rate Constants

Comparison of rate constants measured under different reaction conditions is facilitated by normalizing the observed rate constants (k_{obs}) to factor out the effects of the "dose" of environmental reactant. Appropriate normalizations depend on the specifics of the reactants and reaction mechanism. The possibilities are numerous, but examples of some normalizations appropriate to reactions with solid-phase reductants are given here.

In reactions involving solid-phase reductants (e.g., the reduction of CoCs by zerovalent metals such as ZVI or ZVZ), the effects of the dose of reactant on k_{obs} can be factored out by normalizing to various measures of reductant concentration. This facilitates comparisons between different experimental setups (e.g., batch reactors and columns), different materials (e.g., ZVI vs. ZVZ), and different material formulations (e.g., ZVI produced by different manufacturers or of different particle sizes).

On the most basic level, k_{obs} can be normalized to the mass concentration of reductant added to the system. This normalization is performed according to

$$k_M = k_{obs} / \rho_m \tag{1.25}$$

where k_M is the mass-normalized rate constant and ρ_m is the mass concentration (in g solid-phase reductant per L aqueous phase) (*36*). This normalization is useful for comparing the results of experiments performed with varied ρ_m.

For reactions that occur at the surface of the solid-phase reductant, a better measure of the intrinsic reactivity of the material is a surface area normalized rate constant (k_{SA}), which is defined by the following equations,

$$k_{SA} = k_{obs} / \rho_a \tag{1.26}$$

$$\rho_a = a_s \rho_m \tag{1.27}$$

where ρ_a is the surface area concentration of the reductant (in $m^2\ g^{-1}$) and a_s is the measured specific surface area (in m^2/g) (*36*). Use of k_{SA} is especially advantageous when comparing reductants with different compositions (e.g., ZVI vs. ZVZ) or reductant formulations of different sizes (e.g., micron- and nano-sized ZVI). In some cases it may be relevant to take normalization a step further by normalizing to the surface concentration of reactive sites (*36*), or another measure relevant to the reaction and system of interest.

A tool for making systematic comparisons of kinetic data gathered under different conditions is the log k_{SA} vs. log k_M plot (*37*). An example is shown in Figure 1.5. The relationship between k_{SA} and k_M is illustrated by the diagonal contour lines, which correspond to different values of a_s and have a slope of 1. The data shown in Figure 1.5 is for the reduction of the CoC 1,2,3-trichloropropane (TCP) by different formulations of ZVI and ZVZ, including micron- and nano-scale materials. The rate constants were measured in both batch reactor and column experiments. Viewing the data on a log k_{SA} vs. log k_M plot highlights patterns in the data. For instance, it is apparent that the data fall into two distinct clusters for ZVZ and ZVI. Additionally, the positive difference between the ZVZ and ZVI clusters is greater in k_{SA} than in k_M. This suggests that ZVZ is intrinsically more reactive towards TCP than ZVI (*38*).

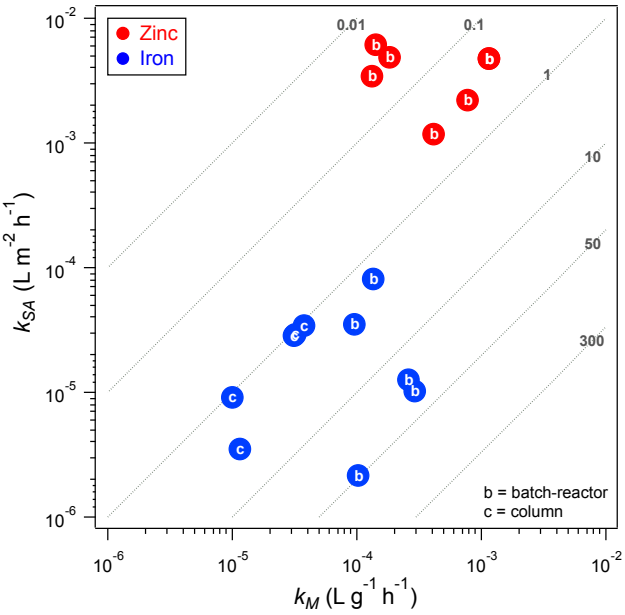

Figure 1.5. log k_{SA} vs. log k_M plot for the reduction of 1,2,3-trichloropropane (TCP) by zerovalent iron (ZVI) and zerovalent zinc (ZVZ). Data were gathered in batch reactor and column experiments with different formulations of the reductants (and/or different pre-treatments). Diagonal contours are representative values of ρ_a (m^2 g^{-1}). Adapted with permission from Sarathy et al., 2010 (*38*). Copyright 2010 American Chemical Society.

1.5. Predicting Rate Constants: Theory and Practice

It some cases, it may be more desirable or more practical to predict rate constants than to measure them experimentally. This may be the case when (*i*) a chemical is not available for experimentation (e.g., it has not yet been synthesized), (*ii*) there is a danger associated with the necessary experiments (e.g., determining rate constants for explosive compounds (*11, 39*)), or (*iii*) data is needed for more compounds than can practically be measured given time and cost constraints (e.g., identifying potential CoCs for further testing to support potential regulation (*40, 41*)). In most cases, rate constants for environmentally relevant reactions are predicted using theoretical or empirical relationships between rate constants and chemical properties. An overview of the theories

and common tools used in predicting rate constants for environmental CoC degradation reactions is presented here.

1.5.1. Activated Complex Theory

Many relationships for calculating or predicting rate constants are based on activated complex theory. This theory (also known as transition state theory) relates the rate of a reaction to the energy of the transition state. Activated complex theory describes a state in the progression of reactants to products where the arrangement of atoms cannot be described as reactants or products, but rather something in between. This species is known as the activated complex. The progression of a generic reaction through these states is illustrated in Figure 1.6, which shows the standard free energy for the hypothetical, simultaneous conversion of 1 mole of reactant to product plotted against the reaction coordinate (*4*). There is a free energy maximum at a point in the reaction corresponding to the presence of the activated complex (known as the transition state). This magnitude of this free energy maximum with respect to the free energy of the reactant is know as the standard molar free energy of activation ($\Delta G^{\circ\ddagger}$). The difference between the final state and the initial state is the reaction free energy (ΔG°_{rxn} or ΔG°).

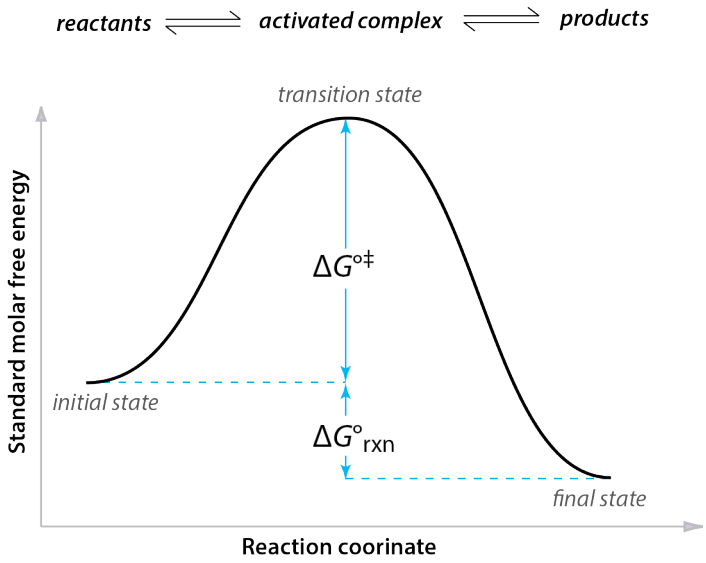

Figure 1.6. Basic reaction coordinate diagram. Adapted with permission from Maskill, 1989 (*4*). Copyright 1989 Oxford University Press.

Activated complex theory postulates that the activated complex can be treated as being in equilibrium with the reactants and products (despite not being a true molecule) (*4, 42*). This treatment leads to an expression of the relationship between the rate of the reaction, k, and $\Delta G^{\circ\ddagger}$ known as the Eyring equation (*4*),

$$k = \frac{k_B T}{h} \cdot e^{-\Delta G^{\circ\ddagger}/RT} \cdot (1 \text{ mol L}^{-1})^{1-n} \tag{1.28}$$

where k_B is the Boltzmann constant, T is temperature, h is Planck's constant, R is the gas constant, and n is the order of the reaction. This theory is the basis for most of the theories and relationships used to describe and predict reaction rates.

1.5.2. The Marcus Theory of Electron Transfer

Many reactions involving CoCs are oxidation or reduction reactions (i.e., redox reactions). As such they involve the transfer of electrons. In inorganic reactions, these processes are described as occurring as either inner-sphere or outer-sphere reactions, where inner-sphere reactions involve an appreciable interaction between the reacting

species during electron transfer and outer-sphere processes display only a weak interaction (*43*). When describing electron transfer between organic species, it has been suggested that the terms bonded and non-bonded are more appropriate, although the terms inner- and outer-sphere are still used most often (*43*).

A theory describing outer-sphere electron transfer for inorganic reactions has been presented by Marcus (*44*) (i.e., "the Marcus theory"). The application of this theory to outer-sphere organic reactions has been described in detail by Eberson (*43*). The Marcus theory describes the relationship between the standard free energy of activation ($\Delta G^{\circ\ddagger}$) for an electron transfer to the corrected standard free energy of the reaction ($\Delta G^{\circ\prime}$). This relationship is given by the following parabolic equation:

$$\Delta G^{\circ\ddagger} = W + \frac{\lambda}{4}\left(1 + \frac{\Delta G^{\circ\prime}}{\lambda}\right)^2 \tag{1.29}$$

where W is an electrostatic term and λ is the reorganization energy for the reaction (*43*).

This relationship can be used to relate the rate constant for the reaction (k) to the thermodynamic term $\Delta G^{\circ\prime}$, which is equal to the free energy of the reaction (ΔG°) plus an electrostatic correction (*43, 45, 46*). For the simplest case, Equation 1.29 can be substituted into the Eyring equation (Equation 1.28) to achieve the following relationship,

$$k = 10^{11} \exp -\left[\frac{\lambda}{4}\left(1 + \frac{\Delta G^{\circ}}{\lambda}\right)^2 \Big/ RT\right] \tag{1.30}$$

where R is the gas constant and T is temperature. This simplified relationship assumes $W = 0$, $\Delta G^{\circ\prime} = \Delta G^{\circ}$, and that the rate at which the reactants defuse together to form a precursor complex (prior to electron transfer) is much smaller than the rate of election transfer. Before applying Equation 1.30, it should first be confirmed that all appropriate

assumptions and simplifications are met, otherwise a more complete treatment should be used (*43*).

1.5.3. Empirical Predictive Models: LFERs and QSARs

In addition to theoretically based relationships, such as the Marcus theory based relationship described by Equation 1.30, there are many empirical predictive relationships relating *k* to various structural or molecular properties. These generally fall into a category of empirical relationships know linear free-energy relationships (LFERs) or—more broadly—quantitative structure activity relationships (QSARs). These relationships are empirical correlations between observed behaviors of a family of closely related substances (such as *k*) and values that describe molecular structure or properties. These are known as target and descriptor variables, respectively.

Descriptor variables for rate constants are most often chosen to reflect the mechanism of the rate-determining step of the reaction. Alternatively, if the mechanism is not known, statistically valid QSARS can give insight into the mechanism of the reaction. This can be challenging, however, especially in complex systems like those of heterogeneous reduction (i.e., reduction by a solid-phase reductant like ZVI), because there are many possible rate-limiting steps (e.g., adsorption, surface reactions, product desorption) (*47*).

The first LFERs to be described were linear correlations between *k* and equilibrium constants (*K*) for a homologous series of organic chemicals defined by simple patterns of substitution (*48-52*). Fundamentally, LFERs are empirical correlations, but they can be justified by the constant relationship between $\Delta G°$ and $\Delta G^{‡}$ over the course of the reaction (*53, 54*). The relationships between these free-energy terms and log

k and log K can be seen in Equations 1.31 and 1.32, where Equation 1.32 is the log form of the Eyring equation (Equation 1.28).

$$\log K = \Delta G^{\circ} / (2.303RT) \tag{1.31}$$

$$\log k = \log\left(\frac{k_B T}{h}\right) - \frac{\Delta G^{\circ\ddagger}}{2.303RT} \tag{1.32}$$

LFERs have also been described relating log k to measureable molecular properties. An example is the correlation between log k and the one electron reduction potential (E^1) for the reduction of nitroaromatic compounds (NACs) (e.g., (*30, 31*)). Again, while this is a purely empirical relationship, it is justified by the relationship between ΔG° and $\Delta G^{\circ\ddagger}$ (*41*). It should be noted that recent evidence suggests that care should be taken in drawing mechanistic conclusions from this empirical correlation and that the more rigorous Marcus theory based (non-linear) FER described in Equation 1.30 may be better suited for this purpose (see Chapter 6).

Examples of the log k vs. E^1 LFER and the Marcus-theory-based FER are given in Figure 1.7A and B. For Figure 1.7B, $\Delta G^{\circ\prime}$ was calculated assuming $\Delta G^{\circ\prime} = \Delta G^{\circ}$ and the following relationship

$$\Delta G^{\circ} = -nF\left[E^1_{\mathrm{NAC}} - E^1_{\mathrm{red}}\right] \tag{1.33}$$

where n is the number of electrons transferred, F is the Faraday constant, E^1_{red} is the one-electron reduction potential for the NAC, and E^1_{red} is the one-electron reduction potential for the reductant. The figures show that, while all the data sets are fit well by a log k vs. E^1 model, only some of the data sets are well fit by the Marcus theory based model described in section 1.5.2. Details and further conclusions regarding these plots are discussed in Chapter 6.

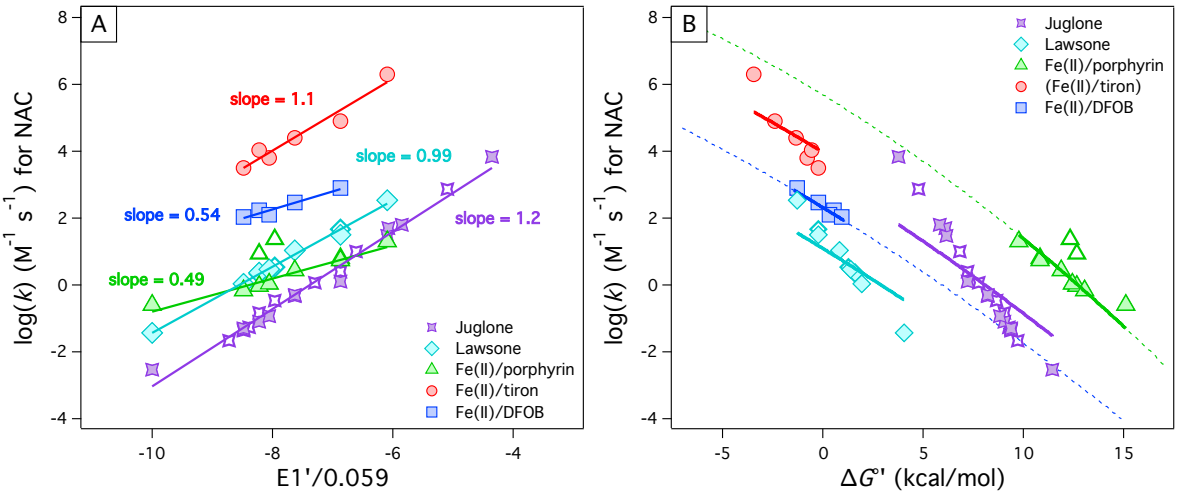

Figure 1.7. log(k_{red}) for the reduction NACs in the presence of a variety of environmentally relevant reductants plotted vs. (A) E1′/0.059, and (B) $\Delta G°'$. Data were fit to (A) a line or (B) the log form of Equation 1.30. In (B), an extrapolation of the fit is shown for cases where data was well fit to Equation 1.30 (as a dashed line). Reproduced from Salter-Blanc et al., 2014, in prep (*39*). See Chapter 6 for more details.

As the field of correlation analysis has developed, correlations have been observed that do not directly relate to free-energy relationships and/or substituent properties. These correlations fall under the broader term QSAR. These relationships utilize a wide range of molecular properties as descriptor variables including aqueous solubility (S_w), the octonal-water partitioning coefficient (K_{OW}), and Hammett parameters such as σ, or structural attributes including chain length and molecular size (*53*). While some authors make a distinction between property activity relationships (PARs) and structure activity relationships (SARs) (e.g., (*53*)), many use the term QSARs (or SARs) more broadly to describe correlations made based solely upon a knowledge of chemical structure (*41, 55*).

1.5.4. Role of Computational Chemistry

Computational chemistry is a useful tool in predicting rate constants for reactions involving CoCs in the environment. Computational chemistry is the field of study that

uses digital technologies to solve equations governing the theories and models that describe chemical systems. Computable quantities include molecular structures, potential energy surfaces (3-dimentional energy surfaces describing the potential energy of all possible configurations of atoms over the course of a reaction), and chemical properties (e.g., molecular properties such as spectral quantities and thermodynamic properties such as free-energies) (*56*). While the use of computational chemistry is unlikely to eliminate the need for experiments, there is often synergy in combining the two (*56*). Examples of useful combinations of computational and experimental chemistry include (*i*) applying computational methods *post facto* to resolve ambiguous results, (*ii*) using the two methods simultaneously, for instance to optimize the design of an experiment, and (*iii*) using theoretical methods to predict properties which are difficult or dangerous to gather experimentally (typically with some sort of experimental validation) (*56, 57*). The last example is particularly relevant to predicting reaction rates of CoCs in the environment.

In principle, rate constants for reactions involving CoCs could be determined from computed values of $\Delta G°$ or $\Delta G°^{‡}$ according to activated complex or the Marcus theory. In practice, however, performing such calculations for reactions involving all but very small molecules is not practical due to excessive computational expense (*58*). However, computational methods are very useful in determining descriptor variables for predictive models such as (L)FERs and QSARs (*57, 58*). Calculable descriptors are numerous and include values related to the charge, total energy, HOMO and LUMO energies, superdelocalizability, polarizability, and more (*58*). Calculated descriptors that have shown promise in predicting *k* for electron transfer reactions include E^1 (either calculated directly (*39, 47, 59-61*) or from correlation with electron affinity (*62, 63*)), the

energy of the lowest unoccupied molecular orbital (E_{LUMO}) (*64, 65*), and bond dissociation energy (*47*) (for dissociative electron transfer reactions). An example of the application of computational methods to computing descriptor variables for a FER describing the reduction of NACs is given in Chapter 6.

1.6. Dissertation Overview

This dissertation presents research regarding the degradation kinetics of CoCs in natural and engineered groundwater systems. It is presented in two parts. Part I (Chapters 2-4) focuses on the remediation of the emerging contaminant 1,2,3-trichloropropane (TCP) with zerovalent zinc (ZVZ). Chapter 2 describes how the rates of TCP reduction by ZVZ are affected by solution chemistry. Chapter 3 describes work that was competed concurrently to that presented in Chapter 2, but with a focus on determining the viability of ZVZ for treating TCP contamination in the field. It reports data from initial column experiments that are not documented elsewhere. Chapter 4 describes the expansion of the results from Chapters 2 and 3 to a field-scale pilot test that was performed in collaboration with Geosyntec Consultants and the U.S. Naval Facilities Engineering Command.

Part II (Chapters 5 & 6) focuses on predicting rate constants determining the environmental fate of novel munitions compounds. Chapter 5 focuses on the hydrolysis of nitroaromatic munitions compounds. It reports rate constants for the alkaline hydrolysis of 2,4,6-trinitrotoluene (TNT) and 2,4-dinitroanisole (DNAN). These are combined with computational results to resolve mechanistic ambiguities that must be resolved before predictions can be made for novel compounds. Chapter 6 focuses on the

reduction of nitroaromatic munitions compounds. A predictive model in the form of a free-energy relationship based on the Marcus theory of electron transfer is reported.

PART I. REMEDIATION OF 1,2,3-TRICHLOROPROPANE WITH ZEROVALENT ZINC

Chapter 2. Effects of Solution Chemistry on the Dechlorination of 1,2,3-Trichloropropane by Zerovalent Zinc[1]

Alexandra J. Salter-Blanc and Paul G. Tratnyek

2.1. Abstract

The reactivity of zero-valent zinc (ZVZ) towards 1,2,3-trichloropropane (TCP) was evaluated under a variety of solution conditions, including deionized water, groundwater, and artificial groundwater, over a pH range of about 6.5-12. In deionized water, first-order rate constants for TCP disappearance (k_{obs}) exhibit a broad minimum between pH 8 and 10, with increasing k_{obs} observed at lower and higher pH. The similarity between this trend and zinc oxide (ZnO) solubility behavior suggests pH related changes to the ZnO surface layer strongly influence ZVZ reactivity. Values of k_{obs} measured in acidic groundwater are similar to those measured in DI water, whereas values measured in alkaline groundwater are much smaller (>1 order of magnitude at pH values >10). Characterization of the surfaces of ZVZ exposed to deionized water, acidic groundwater, and alkaline groundwater suggests that the slower rates obtained in alkaline groundwater are related to the presence of a morphologically distinct surface film that passivates the ZVZ surface. TCP degradation rates in artificial groundwater containing individual solutes present in groundwater suggest that silicate anions contribute to the formation of this passivating film.

[1] Reprint with permission from Salter-Blanc, A. J.; Tratnyek, P. G. Effects of solution chemistry on the dechlorination of 1,2,3-trichloropropane by zero-valent zinc. *Environ. Sci. Technol.* **2011**, *45*, 4073-4079 (*18*). Copyright 2011 American Chemical Society.

2.2. Introduction

1,2,3-trichloropropane (TCP) is an emerging contaminant that is "reasonably anticipated to be a human carcinogen" (*66*). Groundwater contamination with TCP occurs at industrial and agricultural sites due to its use as a solvent for degreasing, feedstock for polymer production, and as a precursor to (and impurity in) some soil fumigants. Recent cases, involving the closure of drinking water production wells due to TCP contamination above action levels (*67*), have focused attention on TCP's unusual persistence and recalcitrance to common methods of remediation (*68*). To provide a more complete understanding of the chemical transformation processes that determine the fate and potential for remediation of TCP, we have recently reported experimental and theoretical studies on the reactivity of this compound (*38, 69*). After consideration of TCP degradation by substitution, hydrolysis, reduction, and oxidation (*38*), we concluded that reduction with zero-valent zinc (ZVZ) was particularly significant because it represents a novel and potentially promising method of affecting relatively fast TCP degradation.

While the ability of ZVZ to degrade chlorinated solvents has been described previously (*9, 70-73*), the advantages of ZVZ over the more conventional and better-characterized zero-valent iron (ZVI) have not been sufficient to generate interest in field-scale applications of ZVZ for remediation of contaminated groundwater. In the case of TCP, however, our results suggest that the kinetic advantage of ZVZ over ZVI is such that ZVZ has potential for remediation of TCP while ZVI does not (*38*).

To assess the prospects TCP remediation with ZVZ under field conditions, we have begun to consider (*i*) the use of less pure, and therefore less expensive, ZVZ; (*ii*) treatment under flow-through conditions (columns); and (*iii*) the effects of solutes found

in groundwater. We reported results on (*i*) and (*ii*) previously (*74*); here we describe results that address (*iii*). The focus of this work is on the effect of solution chemistry—including that of artificial and real groundwater—on the kinetics of TCP degradation using commercial-grade ZVZ. In addition to assessing the reactivity of ZVZ under conditions better reflective of the field, we have attempted to reconcile this reactivity data with information from the literature on zinc corrosion and the mechanism of its passivation.

ZVZ corrodes in deionized (DI) water to form zinc oxide (ZnO) and/or zinc hydroxide ($Zn(OH)_2$) (*75, 76*). These phases are amphoteric, displaying minimum solubilities at approximately pH 9, with solubility increasing at lower and higher pH (producing "U"- or "V"-shaped solubility diagrams) (*76*). Zinc (hydr)oxide corrosion products are present as surface films between pH 6 and 12 (*77*) and—depending on their structure—may inhibit further corrosion, resulting in passivation. These films have been extensively studied under alkaline conditions where they have been classified into two types, "type I" and "type II" (*75, 78, 79*). Type I is bulky and porous and permits continued corrosion of the metal, while type II is thin and more compact and limits corrosion, causing a transition from active to passive states (*75, 78, 79*). Type I films consist of either $Zn(OH)_2$ or ZnO formed by reprecipitation of dissolved Zn^{2+} species according to Equations 2.1 and 2.2 (*78*).

$$Zn(OH)_4^{2-} \leftrightarrow Zn(OH)_2 + 2OH^- \quad (2.1)$$

$$Zn(OH)_4^{2-} \leftrightarrow ZnO + H_2O + 2OH^- \quad (2.2)$$

As the type I film forms, it limits access of hydroxide to the ZVZ surface and promotes the formation of the type II film, which results directly from oxidation of the metal surface, according to Equation 2.3 (*78*).

$$Zn + 2OH^- \leftrightarrow ZnO + H_2O + 2e^- \quad (2.3)$$

Type II films consist of zinc-rich zinc oxides (Zn_xO_y, where x>y), which give the film its characteristically dark appearance (dark gray to black vs. the white of type I films) (*75, 78*).

Similar corrosion reactions are likely to occur in more complex solutions such as groundwater. Under such conditions, ZVZ corrosion is expected to be influenced by the presence of anions that can be categorized into three different types: (*i*) those that increase ZVZ solubility (e.g., Cl^-, SO_4^{2-}), (*ii*) those that reduce the solubility of ZVZ and thus promote formation of potentially protective zinc salts (e.g., CO_3^{2-}, PO_4^{3-}), and (*iii*) those that react with the ZVZ surface and potentially form passive films (e.g., CrO_4^{2-}) (*75*). These solute effects are often concentration dependent (*75*), and few corrosion studies have addressed the effects at concentrations relevant to groundwater. This study assesses the effect of solutes, as present in groundwater over a range of pH, on the reactivity of ZVZ towards TCP.

2.3. Methods

2.3.1. Reagents

The ZVZ used in this study included three industrial-grade materials, Zinc Dust 64 and Zinc Powders 1210 and 1239 (Horsehead Corporation, Monaca, PA). Basic material properties of these materials are summarized in Appendix A, Table A.1. The ZVZ was used as received. Saturated stock solutions of 1,2,3-trichloropropane (>98%,

Fluka) were prepared in deionized (Milli-Q) water. In most experiments, deioinized (DI) water was used without further treatment. Deoxygenated, deionized (DO/DI) water was prepared by sparging with either nitrogen or argon for ~1 h. Groundwater samples were obtained from three sites in Washington and California and designated Site Water P, Q, and M (SWP, SWQ, SWM). Relevant background on the composition of these samples is given in the Appendix A, Table A.4. The groundwater samples were used as received, unless otherwise specified. Artificial groundwater solutions were prepared in DI water using ACS certified salts.

2.3.2. Batch Experiments

Batch reactor experiments were performed in 160 mL serum vials sealed with Hycar septa (Thermo Scientific) and aluminum crimp caps. Reactors were filled with 20 g ZVZ and 80 mL of DI water, deoxygenated DI water (DO/DI water), groundwater, or artificial groundwater. Before addition of TCP, the ZVZ and solution were "pre-exposed" at room temperature for 20–28 hours while rotating end-over-end at ~9 rpm. pH values other than approximately 8.5–10 were obtained by titration with HCl or NaOH (buffers were not used to avoid complications from buffer-metal interactions). Titration induced changes to ionic strength and chloride concentration were not expected to have a significant impact on ZVZ reactivity (more information on ionic strength effects can be found in Appendix A, Figure A.2, and the effect of Cl^- addition can be seen in Figure 2.4). When pH was adjusted, the titration was performed approximately one hour into the pre-exposure period in order to first allow initial pH of the ZVZ/water system to stabilize (measurements of pH change over time showed that the pH of DI water increased rapidly to about 8.5-10 upon the addition of ZVZ (Zn64), but reached a steady value by about 15

min, results not shown). After the pre-exposure period, experiments were initiated by injection of 200 μL saturated aqueous TCP stock solution (for $[TCP]_0 \approx 30$ μM) and then rotated over-ended at ~32 rpm for the duration. The "initial" batch reactor pH was measured after the pre-exposure period, just prior to TCP addition. "Final" batch reactor pH was measured at experiment termination.

2.3.3. Analysis

Aliquots (1 mL) were removed from the batch reactor and analyzed by gas chromatography (GC) with a DB-624 column (J&W/Agilent) and electron capture detection. GC analysis was either performed by headspace analysis of the 1 mL aliquot in a 20 mL headspace vial or by direct injection of a 1:1 hexane extraction of the aliquot. TCP concentrations were determined through comparison to calibration curves prepared by analyzing batch reactors containing various concentrations of TCP in DI water. All batch reactors (including those used in calibration) contained a 1:1 ratio of liquid to headspace. Although this ratio varied slightly between experiments (due to volume occupied by the ZVZ) and during experiments (due to the removal of aliquots for analysis), partitioning calculations indicate that the percent of TCP present in the aqueous and vapor volumes of the batch reactors was fairly constant in all cases (98–99% in the aqueous phase).

2.3.4. Data Fitting and Normalization

Concentration versus time data were fit to pseudo-first-order kinetics to obtain observed rate constants (k_{obs}). In some cases, these data were either normalized to the mass concentration of ZVZ in the batch reactor to obtain mass-normalized rate constants (k_M) or to the surface area concentration (using the specific surface areas obtained by

BET N_2-gas adsorption) to obtain surface-area-normalized rate constants (k_{SA}). The surface area values used for this are given in Appendix A, Table A.1.

2.3.5. Characterization

ZVZ was characterized as received and after ~24 h exposure to either DI water or groundwater, at pH 6.8, ~9.7, and 11.9. Those exposed to solution were separated by vacuum filtration in an inert atmosphere. Filtrates were rinsed three times with acetone and vacuum-dried. Characterizations performed on the dry particles included transmission electron microscopy (TEM) with energy-dispersive X-ray spectroscopy (EDS), X-ray photoelectron spectroscopy (XPS), and X-ray diffraction (XRD). Details of methods for these analyses are provided in Appendix A (Section A.4).

2.4. Results and Discussion

2.4.1. Use of Industrial-Grade ZVZ

The practicality of using ZVZ for treatment of TCP-contaminated groundwater requires the availability of significant quantities of low-cost, sufficiently reactive material. In a recent study (*74*), we evaluated the most readily available industrial-grade granular scrap ZVZ, screening for reactivity in both batch reactors and columns. The results, which are summarized in Appendix A (Figure A.1), show that these materials display similar reactivity to the reagent-grade ZVZ we evaluated previously (*38*). One of these industrial-grade materials, Zinc Dust 64 (Zn64), showed somewhat higher reactivity on a mass-normalized basis, and the rates of TCP degradation were relatively unaffected by dissolved oxygen (Figure A.1). In addition, Zn64 was confirmed to produce propene as the main TCP dechlorination product (shown in Appendix A, Figure A.3). These

considerations led us to select Zn64 for the evaluation of solution chemistry effects presented here.

2.4.2. Effect of pH in DI Water

The reactivity of ZVZ toward TCP in DI water was found to be highly pH dependent. As seen in Figure 2.1, a 3-fold variation was observed in the rate constants for TCP disappearance in the presence of Zn64 over the pH range of 6.51 to 12.7. This degree of variation is similar to that observed for ZVI degradation of carbon tetrachloride over a pH range of 5–10 (*8*), although the "U"-shaped trend is unique. Minimum reactivity was observed from approximately pH 8–10. At pH values outside of this range, reactivity increased under increasingly acidic or basic conditions. This trend parallels the pH dependence of both ZVZ corrosion rate (*77*) and ZnO/$Zn(OH)_2$ solubility (*76*) in DI water. These trends show minima at pH 12 (for corrosion rate) and pH 9 (for solubility) with increased corrosion or solubility at higher and lower pH. The shape and minimum of the trend displayed in Figure 1.4 most closely resembles the trend for zinc (hydr)oxide solubility (Figure 1.4, inset), suggesting that solubility related changes to the phase (e.g., dissolution) strongly influence ZVZ reactivity. TEM/EDS, XPS, and XRD analysis of the ZVZ particles exposed to DI water at pH 6.8, 9.6, and 11.9 (shown in Appendix A, Section 4) confirm that the surface is primarily coated with ZnO and $Zn(OH)_2$.

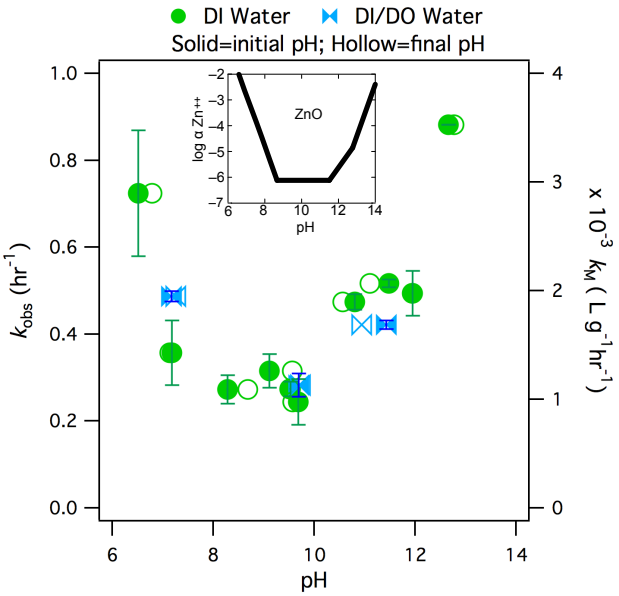

Figure 2.1. Observed reaction rate constants (k_{obs}) and corresponding mass-normalized reaction rate constants (k_M) versus pH for reduction of TCP by 250 g/L Zn64 in DI and DI/DO water. The rate constant for each experiment is plotted versus the initial and final pH of the batch reactor (shown with solid and hollow symbols, respectively). The resulting pair of points represents the range of pH relevant to each experiment. Error bars shown are ± one standard deviation around the k_{obs} fit to the raw concentration versus time data. Inset: Solubility diagram for ZnO in DI water (shown in more detail in Appendix A, Figure A.6A).

2.4.3. Effect of pH in Groundwater

Compared with the effect of pH in DI water, varying the pH of groundwater produced a distinctly different trend in the rate of TCP degradation. Figure 2.2 shows the rate constants for TCP degradation in groundwater from pH 6.29 to 12.1; also shown is a simplified version of the DI water data shown in Figure 2.1 (to facilitate comparison of the trends). At alkaline pH, the rates of TCP degradation are smaller than in DI water. Around pH 10, a typical pH for the system, the k_{obs} measured in groundwater is approximately one order of magnitude smaller than that measured in DI water (corresponding to an increase in half-life from 2.57 h to 26.7 h). This degree of groundwater inhibition is somewhat larger than is usually observed with ZVI: for

example, Liu et al. (*20*), observed TCE degradation rates using nZVI to be 3.5–7.5 times slower in groundwater than in DI water. Another notable difference seen in the groundwater data is the absence of the "U"-shaped trend noted in DI water; under these conditions, it appears that increased pH does not result in increased reactivity of ZVZ.

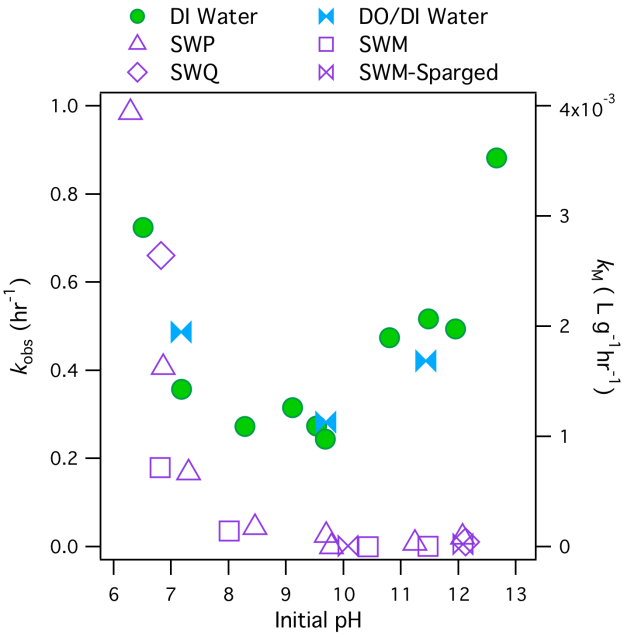

Figure 2.2. Rate constants (k_{obs} and corresponding values of k_M) for TCP degradation by Zn64 in DI water and groundwater (obtained from sites "P", "Q", and "M") at various pH values. Data for DI water are the same as in Figure 2.1. Uncertainties in k_{obs} are not shown for clarity, but they are similar to those shown in Figure 2.1.

The difference in reactivity of ZVZ in groundwater compared to ZVZ in DI water—as shown in Figure 2.2—suggests that a factor other than ZnO solubility controls reactivity in groundwater. As mentioned in the introduction, ZVZ corrosion can be influenced by anions that (*i*) increase ZVZ solubility, (*ii*) reduce ZVZ solubility and promote formation of potentially protective zinc salts, or (*iii*) react with the ZVZ surface to potentially form passivating films (*75*). The slower kinetics observed in the presence of groundwater solutes at alkaline pH indicate that the system must be affected by one of the scenarios (or some combination) resulting in slower corrosion—and therefore

reactivity—of ZVZ, namely, scenario (*ii*) or (*iii*). Both of these scenarios involve changes to the ZVZ surface, so it is expected that the surface of ZVZ exposed to groundwater will display different surface characteristics than ZVZ exposed to DI water. The reactivity data suggests there will also be a difference in the surface characteristics of ZVZ particles exposed to acidic and alkaline groundwater (Figure 2). There are then three categories of solution-exposed particles, (*i*) those exposed to DI water, (*ii*) those exposed to acidic groundwater, (*iii*) those exposed to alkaline groundwater, all with potentially different surface characteristics, perhaps taking the form of type I (non-passivating) and type II (passivating) films.

TEMs of ZVZ particles exposed to DI water and groundwater over a range of pH support the presence of morphologically distinct surface films on particles exposed to DI water, acidic groundwater, and alkaline groundwater. On samples exposed to DI water, at all pH values tested, this film is nonuniform and composed of large, round crystallites (a representative TEM image is shown in Figure 2.3A, the complete set of TEM images is shown in Appendix A, Figure A.4). On samples exposed to acidic groundwater (SWP), the film is also non-uniform with large crystallites, but the crystallite morphology is more needle-like (Figure 2.3B). On samples exposed to alkaline groundwater (SWP), the film is more uniform and is composed of compact crystallites (e.g., Figure 2.3C). The latter film also appears somewhat thinner, an interpretation supported by XRD analysis (Appendix A, Table A.2) showing a lower ZnO content and higher Zn^0 content in samples exposed to alkaline groundwater compared to the other solution-exposed samples. The relative thickness of the oxide layer on the ZVZ particles exposed to DI water and acidic groundwater, combined with the high reactivity of the particles, suggests

that the ZnO on the surface is present as a type I film. Such a film would allow for the continued corrosion of ZVZ, thereby supporting the high degradation rates observed in these solutions. The compact film present on ZVZ exposed to alkaline groundwater (pH 9.8 and 11.9), combined with the limited reactivity of these particles, suggests the presence of a thin, passivating type II film. The presence of this film would inhibit further corrosion of ZVZ and limit interaction of ZVZ with the aqueous surroundings resulting in the low degradation rates observed.

A B C

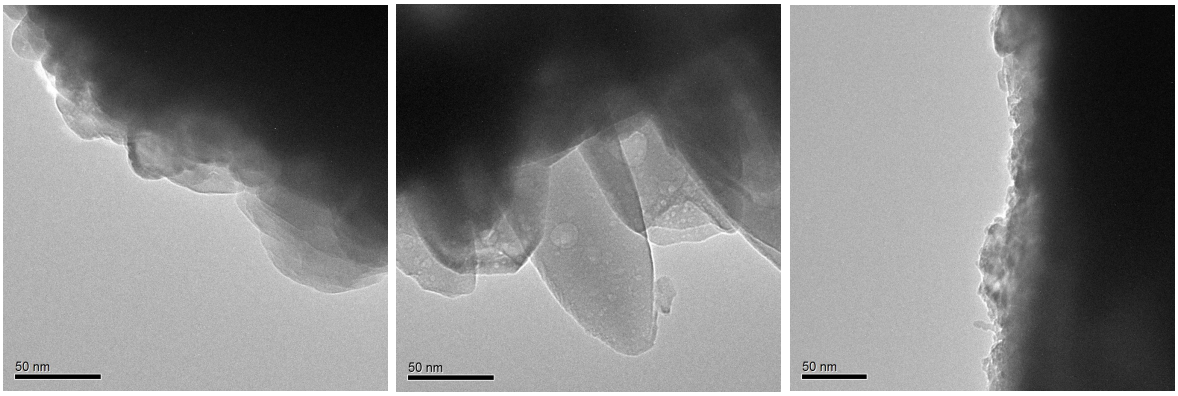

Figure 2.3. TEM images of ZVZ exposed to (A) DI water, displaying a type I film; (B) acidic groundwater, displaying a type I film; and (C) alkaline groundwater, displaying a type II film. More detail is given in Appendix A, Figure A.4.

2.4.4. Effect of Groundwater Solutes

Despite the insights into the structure of the oxide film gained from the TEMs of ZVZ exposed to DI water and groundwater, these data did not reveal precisely what caused the type II film to form in groundwater. The formation of this film is likely to be due to interactions of ZVZ with anions present in groundwater such as carbonate, phosphate, or silicate, all of which are known to inhibit ZVZ corrosion when their concentrations are sufficient (*75, 78, 80-85*). To isolate any effects of anions present in

our groundwater samples, we performed batch reactor experiments in solutions containing the corrosion inhibitors listed above, and other anions, at or above their concentrations in Site Water P (SWP). We believe SWP to be a representative sample, as most of the constituents were present at concentrations within the ranges that are typical of groundwater (*86-88*). The constituents with higher concentrations were Na^{+}, Cl^{-}, and SO_4^{2-}, which were included in our tests. The other solutes tested included borate, nitrate, and natural organic mater (NOM) because these are well know to have passivating effects on corrosion of ZVI. The results of all these "artificial groundwater" experiments are shown in Figure 2.4.

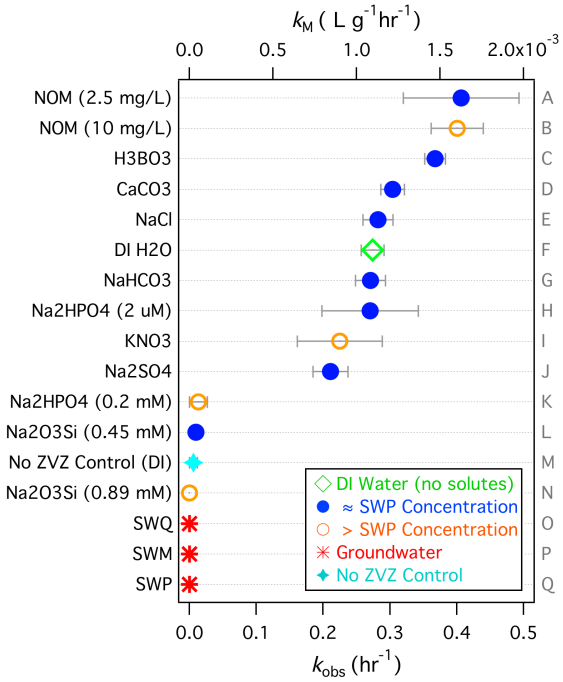

Figure 2.4. Rate constants (k_{obs} and corresponding k_M) for TCP reduction by Zn64 in various solutions, including DI water, groundwater (SWQ, SWP, and SWM), and artificial groundwater prepared at, or above, the reported concentration for Site Water P. pH and ionic strength were not controlled. Error bars shown are ± one standard deviation around k_{obs} from the fit to concentration versus time data. Detailed documentation of experimental conditions, listed according to the letters shown on the right of the figure, is given in Appendix A, Table A.4.

As seen in Figure 2.4, most of the constituents tested had little effect on the rate of TCP disappearance. The small (± 0.1 hr^{-1}) deviations from the rates measured in DI water can be attributed to pH and ionic strength effects, as these parameters were not controlled (more information on batch reactor pH and ionic strength can be found in Appendix A, Table A.4). Even some anions known to strongly inhibit ZVZ corrosion (carbonate, phosphate) did not show a large effect on TCP disappearance rates at the concentration of SWP. Lower disappearance rates were measured when the phosphate concentration was increased by three orders of magnitude to 0.2 mM, but this concentration is at least two orders of magnitude higher than is typical for groundwater (the median concentration of total phosphorous in groundwater is 20 μg/L (0.65 μM) (*87*)), so this effect is unlikely to be significant in most groundwaters . The other solutions to produce low disappearance rates contained sodium meta silicate ($Na_2O_3Si{\cdot}9H_2O$) prepared at concentrations of 0.45 mM and 0.89 mM. The measured concentration of silica (as SiO_2) in SWP is 0.45 mM. The concentrations of these silicate solutions, which were approximately equal to 26 and 53 ppm SiO_2(aq), are within the typical groundwater range of 5-85 ppm (*87*).

Inhibition by Si has been observed previously in studies utilizing ZVI as the reductant. In these studies, SiO_2 was seen to inhibit the reduction of a number or organohalides (*21-23*) and nitroaromatic compounds (*21*) by adsorption to the ZVI surface. While the reactivity of ZVZ with contaminants in silicate solutions has not, to our knowledge, been previously investigated, many studies have addressed the effect of silicate anions on ZVZ corrosion (*75, 78, 80-85*). These studies show that ZVZ corrosion (or reactivity) is decreased in the presence of silicate, and they attribute the inhibitory effect of silicate due to incorporation of Si into or onto the surface of the ZVZ in a Zn-

rich conversion layer. This incorporation likely occurs through adsorption of silicate anions (*78, 82, 83*) and/or the formation of zinc silicate films (*78, 81*). In the first case, silicate anions outcompete hydroxide for active sites on the ZVZ (due to stronger adsorption) (*78*). In the second case, the zinc silicate film presumably passivates the ZVZ surface by forming a physical barrier limiting metal-solvent interactions. Geochemical speciation modeling (shown in Appendix A, Section A.6) predicts $ZnSiO_4$ to be the thermodynamically favorable solid phase under the solute conditions of SWP (vs. ZnO in DI water), supporting the second case.

However, surface analysis did not give evidence for a zinc silicate film on the surface of ZVZ exposed to groundwater (nor other typical passive film forming zinc salts such as $ZnCO_3$). Rather, the data (XPS, XRD, etc.) suggest that the films on these particles were primarily composed of ZnO and $Zn(OH)_2$ (Appendix A, Section A.4), suggesting that the first case, silicate anion adsorption, was responsible for the observed inhibition. It is possible that, in the case of alkaline groundwater, a lack of interaction with hydroxide caused by adsorption of silicate anions led to the formation of the observed type II film. XPS of ZVZ exposed to DI water and groundwater at pH 6.8, ~9.7, and 11.9 showed slightly elevated levels of silicon on ZVZ exposed to alkaline groundwater (atomic concentrations of 0.77-1.18% vs. 0.21-0.42%). These samples also showed slightly elevated levels of magnesium and calcium, suggesting that these ions may also play a role in the formation of the passive film. Regardless of the exact mechanism of the inhibited reactivity of ZVZ toward TCP in groundwater, the effect is likely to be prevalent because the necessary components are common constituents of groundwater.

2.4.5. Implications for Groundwater Remediation

In order to put the ZVZ data from this study into context with previously measured data, we compared our new ZVZ data, collected under relatively realistic groundwater treatment conditions, with previously reported data, which included ZVZ data collected with reagent-grade material in DI water and ZVI data collected with various grades of materials under a variety of conditions (*38*). The resulting values are plotted in Figure 2.5 (using the log k_{SA} versus log k_M format that we have described previously (*37*)). Figure 2.5 shows data reported previously (*38*) in faded, solid symbols and new data in bold, hollow symbols. The industrial-grade ZVZ data collected in DI water and groundwater are the same as those shown in Figure 2.2 (note that they represent a range of pH). It can be seen that, while all the new ZVZ data collected in DI water clusters with the previously measured reagent-grade ZVZ values, the ZVZ data gathered in groundwater over a pH range of about 6-13 spans a much wider range of reactivity. The inhibited TCP degradation kinetics observed with ZVZ in alkaline groundwater display similar k_M and k_{SA} values to those obtained with ZVI.

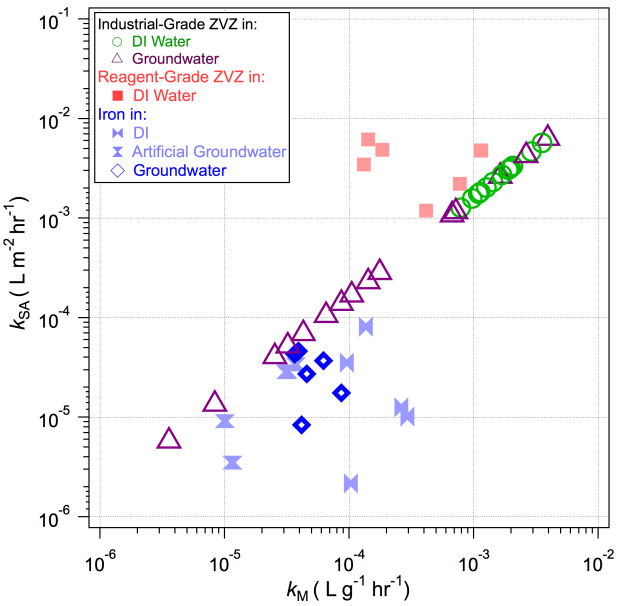

Figure 2.5. k_{SA}-k_M plot showing TCP degradation rates using Zn64 in DI water and groundwater (as reported in Figure 2.2) superimposed onto previously collected data using reagent-grade ZVZ in DI water and various ZVI materials in DI water and artificial groundwater. The Zn64 data fall along a line, the slope of which corresponds to the specific surface area (m^2 g^{-1}) of the material. New data for ZVI reduction of TCP in groundwater is also shown. Previously reported data is shown in faded, closed symbols and new data is shown in bold, open symbols.

Given the perspective provided by Figure 2.5, it is unclear whether ZVZ or ZVI will be more effective in field treatment. It appears that only if groundwater inhibition can be overcome through optimization of the treatment system (e.g., buffering system at acidic pH, pretreating groundwater to remove inhibiting constituents, or pretreating the ZVZ to protect it from passivation), will the potential reactivity advantages of ZVZ be achievable in the field. Alternatively, it is possible that degradation kinetics will not be the most important factor in determining the overall performance of ZVZ in the various configurations that it might be used for field-scale remediation of TCP. Other considerations have barely been investigated, such as the possibility of permeability losses due to hydrogen-bubble formation, changes in reactivity over the long-term due to

particle coating and pore blockage by secondary precipitates, hydrogeological factors that might extend the size of the dissolved Zn^{2+} plume beyond from the zone of treatment, and the cost to performance trade-offs of diluting ZVZ with other granular materials

2.5. Acknowledgements

This work was supported by the Strategic Environmental Research and Development Program (SERDP, Project ER-1458), and the Navy Environmental Sustainability Development to Integration Program (NESDI, Project N62583-09-C-0110). This report has not been subject to review by either agency and therefore does not necessarily reflect their views and no official endorsement should be inferred. Samples of ZVZ were donated by Horsehead Corporation. BET surface analysis was performed by James T. Nurmi, propene concentration analysis by Reid O'Brien Johnson. XPS and XRD data were collected by Ponnusamy Nachimuthu, TEM/EDS data by Libor Kovarik.

XPS, XRD, and TEM/EDS were performed using facilities as the William R. Wiley Environmental Molecular Sciences Laboratory (EMSL), a national scientific user facility sponsored by the Department of Energy's Office of Biological and Environmental Research and located at Pacific Northwest National Laboratory (PNNL), Richland, WA. The authors would like to thank Donald Baer for useful discussions involving the data collected at EMSL.

Chapter 3. Degradation of 1,2,3-Trichloropropane by Zerovalent Zinc: Laboratory Assessment for Field Application[2]

Alexandra J. Salter-Blanc, Paul G. Tratnyek, and Richard L. Johnson

3.1. Abstract

Bench-scale batch reactor and column tests were performed to identify types of granular zero-valent zinc (ZVZ) that might be suitable for remediation of 1,2,3-trichloropropane (TCP) contaminated groundwater. Two industrial grade materials, Zn64 and Zn1210, were selected for further analysis in a scaled-up, ex-situ field test. Groundwater was found to inhibit the reduction of TCP by zinc, but this affect was overcome in some instances by lowering pH. Also illustrated are several of the general issues involved in scaling between batch and column data for treatments with zero-valent metals.

3.2. Introduction

Zero-valent zinc (ZVZ) is known to reduce most chlorinated solvents (*9, 70-72*), but the advantages of ZVZ over zero-valent iron (ZVI) have not been sufficient to generate significant interest in using ZVZ for remediation of contaminated groundwater. Recently, it has been shown that the emerging contaminant 1,2,3-trichloropropane (TCP) is degraded much more rapidly by ZVZ than ZVI in batch experiments (*38*). Since there are currently few options for remediation of TCP-contaminated groundwater, these

[2] Reproduced (with edits) from Salter, A. J.; Johnson, R. L.; Tratnyek Paul, G., Degradation of 1,2,3-trichloropropane by zero-valent zinc: Laboratory assessment for field application. In: *International Conference on Remediation of Chlorinated and Recalcitrant Compounds, 7th*, Monterey, CA, **2010**, Paper No. D-056 (*74*). The original publication is not subject to copyright.

results have sparked interest in the application of ZVZ to remediate several TCP contaminated sites.

TCP contamination can occur at industrial and agricultural sites due to its use as a solvent for degreasing, feedstock for polymer production, and as a precursor to (and impurity in) some soil fumigants. At Camp Pendleton Marine Corps base in southern California, solvent/degreasing activities are presumed to be responsible for TCP contamination exceeding the State of California notification level[3] (0.005 μg/L (*89*)). This contamination has necessitated closure of several drinking water production wells at the site, and prompted a search for effective treatment options so these wells can be put back into production.

Currently, a pilot project utilizing ex-situ treatment columns is being prepared to test the use of ZVZ to treat the TCP-contaminated groundwater at Camp Pendleton. As field-scale tests are consuming of time and resources, initial material analysis and treatability assessments are being performed with bench-scale batch and column tests. In this case, the usual challenges of scaling from laboratory bench to field are compounded by the complete absence of any prior use of granular ZVZ in column or field applications. With this in mind, this paper focuses on the results of the bench-scale portion of this project and then explores the scalability of these results for design of the next, field stage of this project.

[3] Currently, there are no State of California or federal MCLs for TCP (California Environmental Protection Agency 2009); this is consistent with the status of TCP as an emerging contaminant.

3.3. Methods

3.3.1. Reagents

ZVZ used in this study included three industrial-grade materials, Zinc Dust 64 and Zinc Powders 1210 and 1239 (Horsehead Corporation, Monaca, PA). Properties of these materials are given in Table 3.1. All ZVZ materials and the sand used for batch and column fill (#17, U.S. Silica, Berkeley Springs, WV) were used as received. Saturated stock solutions of 1,2,3-trichloropropane (>98%, Fluka) were prepared in deionized (MilliQ) water. In most batch and column experiments, deioinized water was used without further treatment. Deoxygenated, deionized (DO/DI) water was prepared by sparging with either nitrogen or argon. Groundwater was obtained from a well at Camp Pendleton unless otherwise noted.

3.3.2. Batch Experiments

Batch reactor experiments were performed in 160-mL serum vials sealed with Hycar septa (Thermo Scientific) and aluminum crimp caps. Batches contained 20 g ZVZ (with the exception of the Zn64/Zn1210 combination batch, Batch 8, which contained 100 g total ZVZ) and 80 mL of either DI water, DO/DI water, or groundwater. In some cases, batches also contained silica sand in addition to the 20 g ZVZ. Before reaction initiation, the batches pre-equilibrated for 20-28 hours while rotating. If the pH of the batch reactor was adjusted, HCl or NaOH were added after 1 hour of pre-equilibration. Experiments were initiated through the injection of 200 μL saturated TCP stock solution and rotated end-over-end at ~32 rpm for the duration. Initial batch pH measurements were made after pre-equilibration and prior to TCP injection. All batch experiments were performed at room temperature.

3.3.3. Column Experiments

Column experiments were performed in 15-cm long, 2.5-cm I.D. columns (Kontes) filled completely with packing material that corresponded to specific batch experiments. The column packing material consisted either entirely of ZVZ or a ZVZ/sand combination; all reported percentages of materials (e.g., 25% Zn64 in sand) are mass percentages. Columns were prepared by adding a small amount of column influent and, subsequently, column packing material. Pore volume was determined by the mass difference between the dry and wet column. Columns were run in an up-flow manner, with the influent entering the bottom of the column and effluent exiting the top. The column influent was prepared by spiking the chosen solution (i.e., DI water or groundwater) with TCP. This influent was pumped from a reservoir into the column with an HPLC pump (Rainin). Any pH perturbations to the system were made in the reservoir from which the column influent was pumped. Fractions of the column effluent were collected at intervals and analyzed for pH and TCP concentration. All column experiments were performed at room temperature.

3.3.4. Analysis

Aliquots (1 mL) were removed from the batch reactor or column effluent fraction and analyzed by gas chromatography (GC) with a DB-624 column (J&W/ Agilent) and electron capture detection. GC analysis was either performed by headspace analysis of the 1 mL aliquot in a 20 mL headspace vial or by direct injection of a 1:1 hexane extraction of the aliquot. In both cases, TCP concentrations were determined by comparison to identically analyzed calibration curves prepared by analyzing no-zinc batch reactors containing varying concentrations of TCP in DI water.

Table 3.1. ZVZ properties.

Material	Designation	Mesh[1]	Specific Surface Area (m^2/g) [2]	Bulk Density (g/cm^3)
Zinc Dust 64	Zn64	through 325	0.620	2.60
Zinc Powder 1210	Zn1210	20-60	0.016	2.34
Zinc Powder 1239	Zn1239	200-325	0.160	3.27

[1] Provided by manufacturer. [2] Measured by BET gas adsorption.

3.4. Results and Discussion

3.4.1. Batch Experiments

As a first step in selecting candidate materials for future field-scale tests, several types of ZVZ were screened in batch reactor experiments to determine their reactivity towards TCP. The kinetics of TCP degradation in these batch experiments was described by fitting concentration versus time data to a pseudo first-order model to obtain observed rate constants, k_{obs}.

$$[\mathrm{TCP}] = [\mathrm{TCP}]_0 e^{-k_{obs}t} \tag{3.1}$$

Unlike groundwater in permeable reactive barriers (PRBs), the water to be run through the ex-situ treatment columns planned for Camp Pendleton will be at or near equilibrium with the atmosphere. Because of this, batch experiments were carried out in deoxygenated, deionized (DO/DI) and unsparged deionized (DI) water to isolate any effects of oxygen on the material reactivity. As seen in Figure 3.1A and B, Zn64 degraded TCP at the fastest rate, and the rate did not appear to be effected by the presence or absence of oxygen. Degradation of TCP by Zn1210 was slower (by about one order of magnitude), but again did not appear to be effected by the presence of oxygen.

Zn1239 gave TCP degradation kinetics similar to Zn1210 in DO/DI water (despite its higher surface area), but much slower rates in the presence of oxygen (Figure 3.1B).

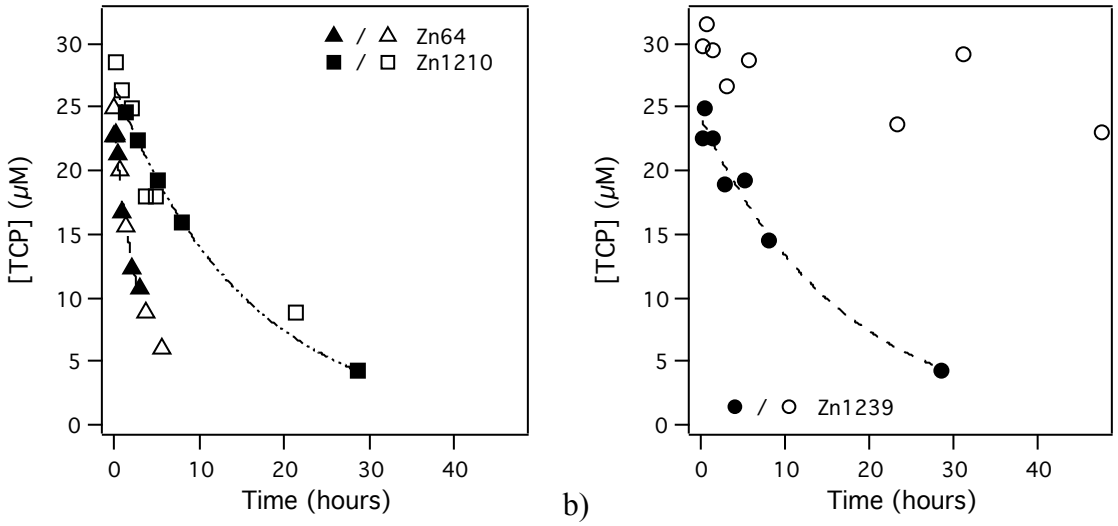

Figure 3.1. (A) Degradation of TCP by Zn64 and Zn1210 in DO/DI and DI water. (B) Degradation of TCP by Zn1239 in DO/DI and DI water. In both figures, solid symbols represent DO/DI data, with fit curves shown (see Equation 3.1). Hollow symbols represent data from unsparged DI water batches. All batches contained an equal mass dose of ZVZ (250 g/L).

After establishing the reactivity of the ZVZ materials in DI water, the rates of TCP reduction by Zn64 and Zn1210 were measured in site groundwater obtained from Camp Pendleton. The degradation of TCP in batch experiments containing site water was significantly slower than TCP degradation in the analogous batch experiments with DI water (mass normalized rate constants, k_M, given in Table 3.2). A similar reduction in reactivity was seen when Zn64 was mixed with sand (a practice often employed in treatment columns made from fine reactive materials in order to minimize back pressure and clogging). However, it was observed that the inhibitory effects of both site water and sand could be overcome, to some degree, by titrating the pH of the batch reactor to below ~7. This is consistent with known effects of pH on zinc oxyhydroxide solubilities (*76, 90*) and corrosion rates (*77*).

Table 3.2. Batch and column data and comparison.

			Batch Data		Column Data					Batch/Column Comparison	
	Batch or Column Solids	Solution	Initial Batch pH[1]	$k_{M,B}$ (L hr^{-1} g^{-1})	Column Influent pH[2]	Column Effluent pH	$\rho_{M,C}$[3] (g L^{-1})	$k_{obs,C}$ (hr^{-1})	η[4]	$k_{obs,C}$* (hr^{-1})	$k_{obs,C}$ / $k_{obs,C}$*
1	Silica Sand Only	DI Water	7.77	2.67 × 10-5	8.17	8.88-8.93	0	~0.024[7]	0.45	0	N/A
2	33% Zn64/sand	DI Water	**6.90**	3.08 × 10-4	**3.57**	7.43-7.50	1579	2.094	0.43	0.486	4.31
3	33% Zn64/sand	Site Water[5]	**6.89**	3.76 × 10-4	**2.26**	6.77-6.99	2264	0.436	0.36	0.852	0.512
4	25% Zn64/sand	Site Water[6]	9.40	3.05 × 10-5	8.57	8.0-8.8	2000	0.185	0.29	0.061	3.02
5	25% Zn64/sand	Site Water[6]	**6.82**	1.33 × 10-3	**2.56**	6.82-6.96	2009	0.447	0.29	2.671	0.167
6	100% Zn1210	Site Water[6]	10.30	2.17 × 10-5	8.08	7.5-8.5	4186	0.066	0.58	0.091	0.730
7	100% Zn1210	Site Water[6]	**6.62**	2.88 × 10-4	**2.45**	6.5-6.9	4884	0.379	0.58	1.408	0.269
8	20% Zn64/Zn1210	Site Water[6]	**7.05**	7.10 × 10-4	**2.36**	7.00-7.24	7895	0.458	0.39	5.608	0.082

[1] Bold values indicate pH values that resulted from titration of the batch reactor with HCl.
[2] Bold value indicate pH values that resulted from titration of the influent with HCl.
[3]Mass concentration: ZVZ mass measured prior to column assembly, solution volume determined from the mass difference between the dry and wet column.
[4] Porosity: determined from the mass difference between the dry and wet column.
[5]Data for Batch 3 were collected in water from another TCP-contaminated site with composition similar to that of Camp Pendleton; the column was run with Camp Pendleton site water.
[6]Obtained from Camp Pendleton.
[7]The TCP concentration of the influent was not measured for this control, so $k_{obs,C}$ is based on a calculated influent concentration.

Based on the above batch data, Zn64 was selected for further investigation in small-scale column experiments because of its high overall reactivity. Zn1210 was also selected because of its large particle size, which may negate the need to mix the material with sand, allowing for 100% of the column to be packed with reactive material and avoiding the inhibitory effect caused by the presence of the sand. Zn1239 was not selected for column testing because of its reduced reactivity in the presence of oxygen and because it did not offer any benefits, either in reactivity or size, that were not represented by the other two materials.

3.4.2. Column Experiments

After selecting Zn64 and Zn1210 from batch experimental results, short-term, small-scale columns were run to assess performance in flow-through systems and to identify an effective mixing ratio of Zn64 with sand. The columns were allowed to run until they reached a steady-state concentration (~24-48 hrs) after which an experimental observed rate constant for the column ($k_{obs,C}$) was determined. The rate constant was extracted from the data by assuming pseudo first-order behavior (see Equation 3.1) and treating the influent TCP concentration as $[TCP]_0$ and the average of the measured concentrations at steady-state as the TCP concentration at the residence time (t_R).

Rearranging Equation 3.1 yields:

$$k_{obs} = -\frac{\ln\left([\mathrm{TCP}]/[\mathrm{TCP}]_0\right)}{t} \tag{3.2}$$

which can be rewritten in terms of measured values:

$$k_{obs,C} = -\frac{\ln\left([\mathrm{TCP}]_{\mathrm{eff}}/[\mathrm{TCP}]_{\mathrm{inf}}\right)}{t_R} \tag{3.3}$$

where $[TCP]_{eff}$ is the average concentration of TCP after the column has reached steady state and $[TCP]_{inf}$ is the concentration of the influent. The resulting rates constants for the column experiments are summarized in Table 2.

The main factors in controlling $k_{obs,C}$ appear to be pH and ZVZ type. Columns run at a low pH consistently showed faster $k_{obs,C}$ than columns run without pH adjustment (for both Zn64 and Zn1210). In columns run at a similar pH, all ratios of Zn64/sand produced a higher $k_{obs,C}$ than 100% Zn1210. In addition, differences in the Zn64/sand mixing ratio (Column 3 and 5) did not have a large effect on $k_{obs,C}$ despite variations in total Zn64 mass (#3 contained 60 g Zn64, #5 contained 43 g). Substituting Zn1210 for sand as a mixing material for Zn64 also had little effect on $k_{obs,C}$, as Columns 5 and 8 (25% Zn64/sand vs. 20% Zn64 in Zn1210, but with equal mass of Zn64) showed a similar $k_{obs,C}$.

In order to test whether or not the fast kinetics observed in pH adjusted, 15-cm columns would be maintained throughout the length of a larger column, a 1-m column with the same packing material and influent as Column 5 was run at a flow rate predicted to give about 80% TCP reduction (see scaling calculations below). The $k_{obs,C}$ was determined to be 0.17 hr^{-1}, which is slower than anticipated and closer to the value from Column 4, the analogous column without pH adjustment, than Column 5. It is likely that fast kinetics like those observed in Column 5 only persisted in the first section of the 1-m column (where pH remained low) and did not apply to the overall $k_{obs,C}$.

Since manipulation of influent pH to the large column did not produce the higher rates of TCP degradation that were observed in batch and small column experiments, the evaluation of materials for the ex-situ field tests at Camp Pendleton is based on results

from columns run without pH adjustment. Of these columns, #4, containing 25% Zn64/sand, displayed a $k_{obs,C}$ three times faster than #7, which contained 100% Zn1210. With respect to the rate of TCP degradation, the 25% Zn64/sand mixture is a favorable choice for further analysis. Other factors must be considered, however, such as the quantity of hydrogen production. In the short-term column experiments, Zn64 appeared to produce a larger volume of hydrogen gas than Zn1210 columns (although this result has yet to be quantified). It is unclear what consequences this will have in the long term. It is also unclear how other factors such as clogging, aging, and inhibition by sand will affect columns made from Zn64/sand and Zn1210 in the long term. Given these uncertainties, it will be desirable to compare both the 25% Zn64/sand mixture and Zn1210 during the ex-situ field test at Camp Pendleton.

3.4.3. Batch/Column Comparison

To help with design of the columns to be tested at Camp Pendleton, scaling calculations can be performed using the batch and small-column data described above. To do this, rate constants for column conditions were calculated from batch results, ($k_{obs,C}^*$), and compared to the measured values of $k_{obs,C}$. $k_{obs,C}^*$ was determined by assuming first-order behavior and a linear dependence of k_{obs} on mass load. As such, $k_{obs,C}^*$ was determined by multiplying the mass-normalized batch-determined rate constant ($k_{M,B}$), expressed in L g^{-1} hr^{-1}, by the mass concentration of ZVZ in the theoretical column ($\rho_{M,C}$), expressed in g L^{-1}. The equation for this calculation is given below.

$$k_{obs,C}^{*} = k_{M,B} \times \rho_{M,C} \tag{3.4}$$

To facilitate direct comparison between the theoretical and experimental columns, the measured mass concentrations of ZVZ from the experimental columns ($\rho_{M,C}$, given in Table 2) were used in the calculations for the theoretical columns. The results of these calculations are given in Table 3.2.

Table 3.2 shows varying degrees of agreement between $k_{obs,C}$ and $k_{obs,C}^*$. For batches/columns that were not pH adjusted (4 and 6), $k_{obs,C}$ was similar or faster than $k_{obs,C}^*$. For pH adjusted columns, the DI water column showed a faster $k_{obs,C}$ than $k_{obs,C}^*$ but the site water columns showed slower $k_{obs,C}$ than $k_{obs,C}^*$, most likely because of differences in pH down the length of the column. The poorest agreement was observed in Column 8, presumably because the residence time was not long enough for Zn1210 to have much effect, and the kinetics were dominated by the mass of Zn64.

3.4.4. Implications for Scale-Up

If first-order behavior and a linear dependence on mass concentration are assumed, scaling calculations can be used to estimate the column parameters (i.e., flow rate, column size) required to treat the well water at Camp Pendleton. This can be done by rearranging Equation 3.3 to solve for residence time (t_R),

$$t_R = -\ln\left(\frac{[TCP]_{eff}/[TCP]_{inf}}{k_{obs,C}}\right) \tag{3.5}$$

and inserting the TCP concentration of the well water for $[TCP]_{inf}$ and the desired concentration of the treated water for $[TCP]_{eff}$. Since residence time is determined by the volume of water present in the pore space (V_w) and the volumetric flow rate (Q), these parameters can be substituted into Equation 3.5, which can then be rearranged to yield Equation 3.6.

$$V_w = -\ln\left(\frac{[\mathrm{TCP}]_{\mathrm{eff}}/[\mathrm{TCP}]_{\mathrm{inf}}}{k_{obs,C}}\right)\times Q \tag{3.6}$$

If V_{w} is expressed in terms of the material porosity (η) (empirically determined, see Table 2) multiplied by the column volume (V_{c}), the equation becomes,

$$\eta \times V_c = -\ln\left(\frac{[\mathrm{TCP}]_{\mathrm{eff}}/[\mathrm{TCP}]_{\mathrm{inf}}}{k_{obs,C}}\right)\times Q \tag{3.7}$$

which can be solved for either column volume or flow rate after entering in experimentally determined values from this study. Whether or not the equation is solved for V_{c} or Q will be determined by which of these parameters has been predetermined for the treatment scenario in question. In the upcoming pilot tests, the column size is relatively restricted so the flow rate will need to be varied to control the column effluent concentration. In potential large-scale drinking water treatment the flow rate will likely be dictated by supply demands and a column(s) will need to be sized to accommodate that parameter.

Assuming the columns employed in the pilot tests at Camp Pendleton will be 120 inches (3 m) long with a 6 inch (15.2 cm) I.D., the flow rate required to reduce the well water from 5 µg/L (one of the highest values at the site) to 0.005 µg/L (the California EPA notification level (*89*)) can be estimated using Equation 3.7. A column packed with 100% Zn1210 will require a 310 mL/hr flow rate (104 hr residence time) and a column packed with 25% Zn64/sand will require a 430 mL/hr flow rate (37 hour residence time). This level of performance is less than desired, but is comparable or better than any other reduction-based (*38*) or chemical oxidation or enhanced bioremediation treatments (*68*), although quantitative comparisons under the specific groundwater conditions have not been made. To fully utilize ZVZ as a reductant, methods of eliminating or reducing

groundwater inhibition must be identified. Future research should focus on identifying methods of either maintaining low pH throughout the column (e.g., using a pH buffering mixing material), or removing the constituents responsible for groundwater inhibition (e.g., a pretreatment column).

3.5. Conclusions

Based on our bench-scale analyses, we recommend Zn64 and Zn1210 for further testing at Camp Pendleton. Zn64 clearly showed the fastest kinetics of the materials tested, but due to material size considerations and apparent hydrogen production rates, Zn1210 may be a more practical choice in long-term applications. It was seen that groundwater inhibition greatly reduces the ability of ZVZ to reduce TCP. While this inhibition can be overcome in batch experiments by lowering the pH to below ~7 and in small-scale column experiments by titrating the influent pH to ~2, pH adjustments do not appear to overcome inhibition in larger (i.e., 1 m long) columns. Treatment of TCP with ZVZ will be more effective in a system that either maintains low pH or employs a method of removing inhibiting groundwater constituents.

3.6. Acknowledgments

This work was supported by grants from the Navy Environmental Sustainability Development to Integration Program (NESDI) and the Strategic Environmental Research and Development Program (SERDP). It has not been reviewed by either agency and therefore does not necessarily reflect their views and no official endorsement should be inferred.

Chapter 4. Evaluation of Zerovalent Zinc for Treatment of 1,2,3-Trichloropropane-Contaminated Groundwater: Laboratory and Field Assessment[4]

Alexandra J. Salter-Blanc, Eric J. Suchomel, John H. Fortuna, James T. Nurmi, Chris Walker, Tom Krug, Suzanne O'Hara, Nancy Ruiz, Theresa Morley, Paul G. Tratnyek[5]

4.1. Abstract

The efficacy and feasibility of using zerovalent zinc (ZVZ) to treat 1,2,3-trichloropropane (TCP) contaminated groundwater was assessed in laboratory and field experiments. In the first portion of the study, the reactivity of commercially available granular ZVZ towards TCP was measured in bench-scale batch-reactor and column experiments. These results were used to design columns for on-site pilot-scale treatment of contaminated groundwater at a site in Southern California. Two of the ZVZ materials tested were found to produce relatively high rates of TCP degradation as well as predictable behavior when scaling from bench-scale to field testing. In addition, there was little decrease in the rates of TCP degradation over the duration of field testing.

[4] This chapter is reproduced (with edits) from Salter-Blanc, A. J.; Suchomel, E. J.; Fortuna, J. H.; Nurmi , J. T.; Walker, C.; Krug, T.; O'Hara, S.; Ruiz, N.; Morley, T.; Tratnyek , P. G. Evaluation of zerovalent zinc for treatment of 1,2,3-trichloropropane contaminated groundwater: Laboratory and field assessment. *Ground Wat. Monitor. Remed.* **2012**, *32*, 42-52 (*91*) and is reprinted with the permission of Groundwater Monitoring & Remediation.

[5] The field-scale columns described in this chapter were engineered and operated by Geosyntec Consultants. Current and former Geosyntec staff members Eric J. Suchomel, John H. Fortuna, Chris Walker, Tom Krug, and Suzanne O'Hara contributed to the design and management of field-scale operations. James T. Nurmi collected sieving data, TEM images, and XRD data. The remaining bench-scale experiments, development of scaling calculations, and data synthesis and analysis were performed by Alexandra J. Salter-Blanc under the mentorship of Paul G. Tratnyek. Contributions to project direction and oversight were made by Nancy Ruiz and Theresa Morley.

Finally, no secondary impacts to water quality were identified. The results suggest ZVZ may be an effective and feasible material for use in engineered treatment systems, perhaps including permeable reactive barriers (PRBs).

4.2. Introduction

1,2,3-trichloropropane (TCP) is a chlorinated volatile organic compound that has been used in a variety of chemical production processes, as a precursor to agricultural chemicals, and as a solvent, resulting in point and non-point source contamination in soil and groundwater. TCP is anticipated to be a human carcinogen (*92*). Toxicity to humans appears to be high relative to other chlorinated solvents (*93*), suggesting even low-level exposure to TCP could pose a significant human health risk. In response, the State of California has established a public health goal (PHG) of 0.0007 μg/L in addition to a notification level of 0.005 μg/L for TCP in drinking water (*89*). These stringent standards, in combination with improved analytical methods, have resulted in an increased awareness of TCP contamination throughout the state (*89*). This has, in turn, placed TCP among emerging contaminants that are being considered by a number of organizations as a possible priority for future research and regulation. For example, TCP is included in the most recent version of the U.S. EPA's drinking water Contaminant Candidate List (CCL3) (*94*) and the ATSDR 2011 Hazardous Substance Priority List (*95*). TCP is also one of eight volatile compounds considered under the U.S. EPA's current Drinking Water Strategy (*96*).

Compliance with these existing and potential regulations will require identification of more effective remediation strategies. This will be challenging, as TCP degradation has proven to be hard to achieve under most natural and engineered

remediation processes; including biodegradation (*97-102*), hydrolysis (*38, 103*), advanced oxidation processes (*68, 104, 105*), and reduction by granular and nano-scale zerovalent iron (ZVI and nZVI) (*38*).

Recently, zerovalent zinc (ZVZ) has been identified as a potentially promising reductant for TCP remediation (*38*). Reduction of TCP by ZVZ produces propene, without significant accumulation of intermediate products (*18, 38*). ZVZ is known to reduce many chlorinated solvents (*9, 70-72*). Despite this, the kinetic advantages of ZVZ over ZVI have not been sufficient to generate significant interest in using ZVZ for remediation of contaminated groundwater, especially given the greater cost. In the case of TCP, however, a stronger reductant (such as ZVZ) may be required to achieve sufficient removal in treatment systems.

ZVZ reduces TCP at rates 1-3 orders of magnitude faster than ZVI in well-mixed batch reactor experiments containing deionized (DI) water (*38*). The rate of this reaction is controlled by the presence of surface films composed of zinc (hydr)oxide, which passivate the ZVZ to varying degrees depending on pH and the presence of certain groundwater solutes (passivating species include silicate anions and potentially magnesium and calcium) (*18*). In alkaline groundwater, TCP reduction rates are lower compared to those measured in DI water, resulting in an order-of-magnitude decrease in the observed rate constant (or an order-of-magnitude increase in half-life) at pH 8-10, which is the equilibrium pH of the system. Rates of TCP reduction by ZVZ in alkaline groundwater are, however, on the order of (or faster than) reduction rates measure with ZVI, even using industrial-grade ZVZ (*18*), suggesting ZVZ may still be a promising option for site treatment of TCP-contaminated groundwater.

To gain a more complete understanding of the efficacy of ZVZ for treatment of TCP contaminated groundwater (and to better understand issues surrounding the transferability and scalability of laboratory results), we conducted a comprehensive evaluation of three commercially available ZVZ products for treatment of TCP at a site in Southern California. This study contained two major parts, (*i*) initial material analysis and screening in the laboratory, and (*ii*) on-site testing of the most effective materials, determined in laboratory screening, in pilot-scale columns.

4.3. Methods

4.3.1. Reagents

The ZVZ used in this study included three industrial-grade materials, Zinc Dust 64 (Zn64), Zinc Powder 1210 (Zn1210), and Zinc Powder 1239 (Zn1239), all from Horsehead Corporation (Monaca, PA). Properties of these materials are given in Table 4.1. All ZVZ was used as received. Reagent-grade TCP was used for all experiments. Sand used in column experiments included a fine-grained silica sand used in bench-scale testing (#17, U.S. Silica, Berkeley Springs, WV), and a larger-grained silica sand used in on-site testing (Monterey #3 Sand, Pacific Polymers International, Inc., Garden Grove, CA). Groundwater was obtained from a monitoring well at the location of on-site testing.

Table 4.1. ZVZ properties.

Material	Designation	Mesh[1]	Specific Surface Area (m^2/g) [2]	Bulk Density (g/cm^3)[3]
Zinc Dust 64	Zn64	through 325	0.620	2.60
Zinc Powder 1210	Zn1210	20-60	0.016	2.34
Zinc Powder 1239	Zn1239	200-325	0.160	3.27

[1] Provided by manufacturer. [2] Measured by BET N_2 gas adsorption. [3] For freely settled material.

4.3.2. Batch Reactors

Well-mixed batch reactor experiments were performed in 160-mL serum vials sealed with Hycar septa (Thermo Scientific) and aluminum crimp caps. Reactors contained 20 g ZVZ and 80 mL of DI water, deoxygenated DI water, or groundwater. In most cases, the headspace of the serum vial contained air, except for when deoxygenated DI water was used, in which case the headspace consisted of 5% hydrogen in nitrogen.

Before reaction initiation, the batches were pre-equilibrated for 20-28 hours while rotating. If the pH of the batch reactor was adjusted, HCl or NaOH was added after 1 hour of pre-equilibration. Experiments were initiated through the injection of 200 μL of a saturated TCP stock solution (for a concentration of ~30 μM or ~4.4 mg/L) and were then rotated end-over-end at ~32 rpm for the duration of the experiment. Initial batch pH measurements were made after pre-equilibration and prior to TCP injection. All batch experiments were performed at room temperature.

4.3.3. Bench-scale Columns

Bench-scale column experiments were performed in 15-cm long, 2.5-cm I.D. columns (Kontes) filled completely with packing material, except for one experiment, which used a 1-m long, 2.5-cm I.D. steel pipe (as a preliminary test of scalability). The column packing material consisted either entirely of ZVZ or of a ZVZ/sand mixture; all reported percentages of materials (e.g., 25% Zn64 in sand) are mass percentages (wt:wt). Columns were prepared by adding a small amount of column influent media and, subsequently, column packing material. Columns were run in an upflow manner, with the influent entering the bottom of the column and effluent exiting the top.

The column influent was prepared by spiking the influent media (i.e., DI water or groundwater) with TCP (~30 μM). The influent was pumped from a reservoir through the column with an HPLC pump at a flow rate of 0.25 mL/min (Rainin). Any pH adjustments to the system were made in the reservoir from which the column influent was pumped. Fractions of the column effluent were collected over time and analyzed for pH and TCP concentration. All column experiments were performed at room temperature.

4.3.4. Analysis of Bench-scale Experiments

Aliquots (1 mL) were removed from batch reactors or column effluent fractions and analyzed by gas chromatography (GC) with a DB-624 column (J&W/ Agilent) and electron capture detection. GC analysis was either performed by headspace analysis of the 1 mL aliquot in a 20 mL headspace vial or by direct injection of a 1:1 hexane extraction of the aliquot. In both cases, TCP concentrations were determined by comparison to calibration curves prepared by analyzing no-zinc batch reactors containing varying concentrations of TCP in DI water.

4.3.5. Field-scale columns

In Phase I of on-site testing, columns were constructed in order to test the effectiveness of Zn64 and Zn1210. Columns for each zinc material were composed of two in-series 100 cm long sections of clear PVC pipe (lead and lag column arrangement) filled completely with relevant packing material. Columns were prepared by adding a small amount of column influent media and, subsequently, small ~2 cm lifts of column packing material. The columns were mixed during packing to minimize stratification of the column packing material. The Zn64/sand column was constructed from 10 cm diameter pipe and the Zn1210 column from 15 cm diameter pipe. Column end caps and

influent and effluent valves were constructed from PVC and attached to the column bodies using VOC-free PVC cement. Midpoint sample ports were installed after each lead column and effluent sample ports were installed after each lag column. Columns were mounted vertically and run in an upflow manner. The column influent was pumped from a reservoir through the columns at a nominal flow rate of 5 mL/min with a peristaltic pump (Masterflex L/S MultiChannel Pump System). Column influent consisted of groundwater extracted from a local groundwater monitoring well that was stored in a reservoir and spiked with sufficient TCP to reach a concentration of approximately 5 μg/L. The spiked influent was stored under an argon blanket to minimize changes to groundwater geochemistry.

For Phase II of on-site testing, the lead and lag column segments were constructed from 5-gallon screw-top polyethylene pails connected in series. Column packing procedures were as described for Phase I, except that the column segments were not completely filled so that approximately 2 cm of headspace was allowed to remain in the pails above the packing material in order to minimize pressure build up due to hydrogen generation. Polypropylene ball and check valves were installed near the bottom and top of each pail to serve as influent and effluent ports. A headspace pressure relief valve was installed in each pail lid. Columns were run in upflow mode. Influent was pumped through the column segments at a nominal flow rate of 5 mL/min using peristaltic pumps located before and after the inlet and outlet of each column segment to both feed and pull water to or from each segment. Midpoint and effluent sample ports were installed after each lead and lag column segment, respectively.

4.3.6. Analysis of Field Samples

During column operation, samples were collected biweekly from the influent reservoir, the midpoint of each column, and the effluent of each column. Samples were analyzed for water quality parameters (pH, oxidation reduction potential (ORP), temperature, and dissolved oxygen (DO)) using a field meter. Additionally, TCP, potential degradation products propane and propene, dissolved zinc, cations (calcium, iron, magnesium, sodium, potassium), anions (chloride, sulfate, nitrate, nitrite), sulfide, silica, phosphate, and alkalinity were analyzed by either Calscience (Garden Grove, CA) or Microseeps, Inc. (Pittsburgh, PA) using standard methods (more information can be found in the Supporting Information to the published version of this chapter (*91*), Table S1).

4.4. Results: Bench-scale Material Screening and Analysis

Prior to on-site testing, three ZVZ materials were screened in bench-scale experiments for reactivity towards TCP. First, material reactivity and the effects of DO and groundwater constituents were assessed in batch reactor experiments. Following this, promising materials were assessed in small-scale column experiments to test the scalability of the batch reactor results and identify potential operational considerations.

4.4.1. Batch Reactor Experiments

As an initial step in material analysis, three types of industrial-grade ZVZ (Zn64, Zn1210, and Zn1239) were screened in batch reactor experiments containing TCP spiked DI water or deoxygenated DI water to quantify reactivity towards TCP and sensitivity to DO.

The kinetics of TCP degradation were described by fitting concentration versus time data with a pseudo first-order model (Equation 4.1) to obtain an observed rate constant, k_{obs}.

$$[TCP] = [TCP]_0 e^{-k_{obs}t} \tag{4.1}$$

The k_{obs} values were then normalized to obtain $k_{M,}$ the mass normalized rate constant, and k_{SA}, the surface area normalized rate constant (*36*). k_M was obtained by normalizing to the mass concentration (ρ_m) (in g ZVZ/L H_2O) according to Equation 4.2.

$$k_M = k_{obs} / \rho_m \tag{4.2}$$

k_{SA} was obtained by normalizing to the surface area concentration (ρ_a) of ZVZ, which is a function of the specific surface area (a_s) (in m^2/g, given in Table 4.1) and ρ_m.

$$\rho_a = a_s \rho_m \tag{4.3}$$

$$k_{SA} = k_{obs} / \rho_a \tag{4.4}$$

The results of ZVZ screening in batch reactor experiments are summarized in Figure 4.1.

The format of Figure 4.1 (log k_{SA} vs. log k_M) is used because it allows for systematic comparisons of kinetic data gathered under different conditions (e.g., ZVZ with higher ρ_a vs. lower ρ_a, batch reactor vs. column, etc.) (*37*). In this case, new kinetic data for TCP degradation by industrial-grade ZVZ (shown in hollow symbols) are compared to previously collected data (shown in solid gray diamonds) for TCP degradation by reagent-grade ZVZ in DI water (*38*). The previously collected reagent-grade data clusters within an order of magnitude in both k_{SA} and k_M.

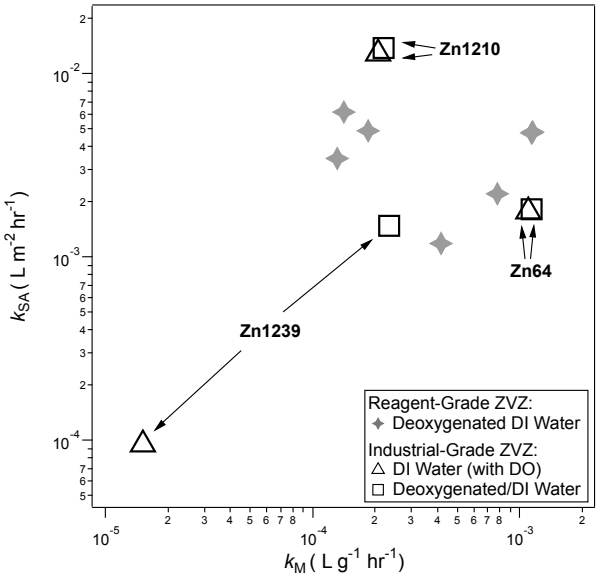

Figure 4.1. Comparison of TCP degradation kinetics by industrial-grade ZVZ (this study) to rate constants obtained with reagent-grade ZVZ and reported previously (*38*). Industrial-grade ZVZ included Zinc Dust 64 (Zn64), Zinc Powder 1210 (Zn1210), and Zinc Powder 1239 (Zn1239). Kinetics were measured in DI water (containing DO) and deoxygenated DI water (without DO).

Superimposed onto this are the data collected as part of this study with Zn64, Zn1210, and Zn1239 in DI water or deoxygenated DI water. The data for Zn64 and Zn1210 collected in both DI water and deoxygenated DI water cluster with the reagent-grade data. This suggests that these materials give similar TCP degradation kinetics to higher purity reagent-grade ZVZ, and that they are insensitive to the initial presence of oxygen. In the case of Zn1239 only the data point for the deoxygenated experiment clusters with the reagent-grade data, while the data point for the experiment containing DO falls over an order-of-magnitude slower in both k_{SA} and k_M. The lower reactivity of Zn1239 towards TCP in the presence of DO suggests that it may be a less promising candidate for *in situ* and *ex situ* groundwater treatment systems, which may contain DO to varying degrees. Zn64 and Zn1210, however, do not appear to be affected by DO and produce TCP degradation rates on the scale of those measured in the presence of more

costly reagent-grade materials. For these reasons, only Zn64 and Zn1210 were used for further screening.

In addition to measuring the effects of dissolved oxygen, the effects of pH and groundwater solutes were also assessed. Detailed findings obtained using Zn64 have been presented previously (*18*), while the results presented here suggest Zn1210 is similarly affected by solution chemistry.

In prior work (*18*), it was found that changes in pH between 6 and 12 cause variation in the rates of TCP degradation by Zn64 in DI water (within an order of magnitude). Titration of pH to values lower or higher than 8-10 (the equilibrium pH of the system) produced increased degradation rates. Replacing DI water with acidic groundwater (pH <7) did not alter this trend (i.e., in groundwater below pH 7, the kinetics were similar to those measured in DI water). Alkaline groundwater (pH >7), however, inhibited ZVZ dechlorination of TCP compared to DI water. In the pH range of 8-10, this resulted in an order-of-magnitude decrease in k_{obs} (corresponding to an increased half-life of ~25 h versus ~2.5 h). This inhibition is explained as being due to changes in the composition and structure of the zinc (hydr)oxide surface film, which were likely influenced by the presence of silicate anions in groundwater.

The results of this previous study are summarized in Figure 4.2. The data for Zn64 falls along a diagonal line corresponding to the specific surface area (SSA) of the material. All data collected in DI water—with and without DO—(shown in gray circles) cluster within an order of magnitude in k_{SA} and k_M. Data collected in acidic groundwater (black diamonds) also fall in this range. Data collected in alkaline groundwater (black triangles) fall between 1 and 3 orders of magnitude slower in k_{SA} and k_M.

Additional data collected with Zn1210 as part of this study show a similar trend, with data collected in DI water and acidic groundwater clustering together and data collected in alkaline groundwater being slower. Details on the trend of Zn1210 reactivity in DI water and groundwater at various pH values are given in the Supporting Information to the published version of this chapter (*91*), Figure S1.

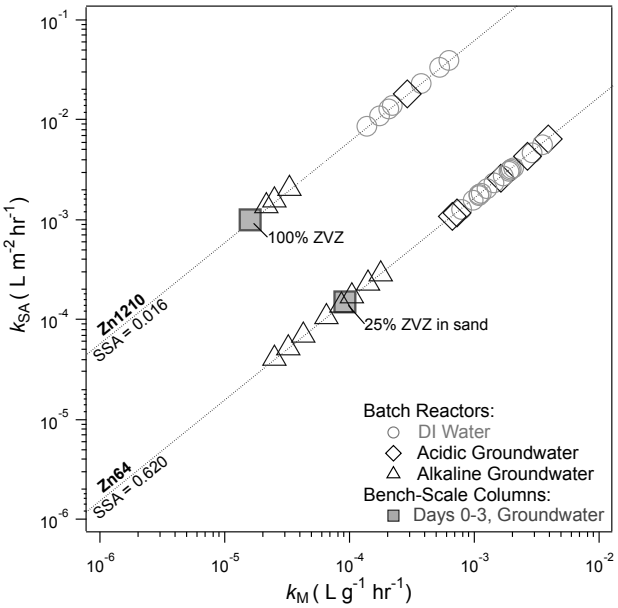

Figure 4.2. TCP degradation rates by Zn64 and Zn1210 in DI water and deoxygenated DI water (gray circles) and in groundwater (black triangles and gray filled black squares). Data was measured in both batch reactor experiments (hollow symbols) and column experiments (solid symbols). The majority of scatter is due to variations in pH (see Salter-Blanc et al. 2011 and the Supporting Information to the published version of this chapter (*91*), Figure S1). Data for Zn64 are from Salter-Blanc, et al. 2011.

As seen in Figure 4.2, both Zn64 and Zn1210 display inhibited TCP degradation rates in alkaline groundwater compared to DI water or acidic groundwater, however, the kinetics are comparable or faster than kinetics than typically observed with ZVI, which degrades TCP at rates on the order of 10^{-6}-10^{-4} in k_{SA} and 10^{-5}-10^{-4} in k_M (Sarathy, 2010). Comparing the two ZVZ types, Zn1210 produces relatively fast rates in k_{SA}, suggesting a higher intrinsic reactivity of the material to TCP. Zn64 produces somewhat faster rates in

k_M, and therefore faster TCP degradation per mass of material. Both materials were considered in the column and field phases of this work.

4.4.2. Bench-scale columns

Following initial screening in batch reactor experiments, the reactivity of Zn64 and Zn1210 were assessed in short duration (1-3 day) bench-scale column experiments using site groundwater in order to gauge the scalability and transferability of the batch reactor results and to assess potential operational concerns. Column media consisted of either Zn1210 alone or Zn64 mixed with sand (necessary to achieve flow due to the fine mesh of Zn64). Packing material details are given in the Supporting Information to the published version of this chapter (*91*), Table S2.

Rate constants for column experiments were extracted from the data by assuming pseudo first-order behavior. Rearranging Equation 4.1 yields Equation 4.5,

$$k_{obs} = -\frac{\ln([TCP]/[TCP]_0)}{t} \tag{4.5}$$

Based on the assumption that $[TCP]_0$ is equal to the influent concentration ($[TCP]_{inf}$), and that the effluent concentration ($[TCP]_{eff}$) is $[TCP]$ at the residence time of the column (t_R) (*74*), Equation 4.5 can be rewritten in terms of measured values (Equation 4.6).

$$k_{obs} = -\frac{\ln([TCP]_{eff}/[TCP]_{inf})}{t_R} \tag{4.6}$$

t_R was determined from the flow rate and from the pore volume, which in turn was determined by taking the mass difference between the dry and wet packed column and assuming 1 g water was equal to 1 mL pore space.

From data presented and discussed in detail elsewhere (*74*), it was concluded that the main factors controlling k_{obs} in these columns were pH and ZVZ material type. In that study, columns adjusted to run at a lower pH consistently showed faster degradation rates than columns run without pH adjustment (for both Zn64 and Zn1210). This is consistent with the behavior noted in batch reactor experiments. However, when column length was increased (from 15 cm to 1 m) no effect of influent pH was observed, likely because the low pH conditions only persisted in the first few centimeters of the column. In columns run at a similar pH, all ratios of Zn64/sand showed faster k_{obs} relative to Zn1210, as expected given the higher k_M of Zn64 in the batch experiments. Differences in the Zn64/sand mixing ratio (25% or 33% Zn64, by mass) did not have a large effect on degradation rates despite variations in total Zn64 mass.

Column kinetics for the two columns most relevant to this study are shown in Figure 4.2 (normalization to k_M and k_{SA} was as described for the batch-reactor experiments). These columns contained 25% Zn64/sand and 100% Zn1210. Both columns produced TCP degradation rates in or near the range of kinetics gathered in batch reactor experiments conducted in alkaline groundwater (in the column experiments, the pH of both the influent groundwater and the effluent was greater than 7). The agreement between the results suggests that the kinetics measured in batch reactors are scalable to columns of this size.

The value of k_{obs} obtained for the 25% Zn64/sand column was 0.185 h^{-1} (a half life of 3.7 h), while k_{obs} for the Zn1210 column was 0.066 h^{-1} (a half life of 10.5 h). From these results alone, it would appear that the Zn64/sand mixture is a more promising candidate for use in engineered treatment systems due to higher reactivity per column

volume. However, these small-scale, short-term experiments were not able to capture the potential effects of longer-term exposure in larger treatment systems (e.g., effects of aging on ZVZ reactivity, susceptibility of the packing material to clogging, effects of hydrogen gas production due to ZVZ reduction of water). For these reasons, both Zn64 and Zn1210 were used as packing materials for the on-site portion of this study.

4.5. Results: On-site Column Testing

4.5.1. Design

For the on-site testing portion of this study, results from the bench-scale analyses were used to size columns for field-testing. Columns were designed assuming pseudo first-order TCP degradation rates based on the bench-scale studies described above. The assumption was also made that k_{obs} is independent of column geometry (k_{obs} is a function of k_M and ρ_m, both of which are constant when the only void space in the column is related to the media porosity). Using these assumptions, Equation 4.6 can be rearranged to predict $[TCP]_{eff}$ based on the k_{obs} determined in bench-scale testing, a calculated t_R, and $[TCP]_{inf}$:

$$[TCP]_{eff} = e^{-(k_{obs} t_R)} [TCP]_{inf} \tag{4.7}$$

Based on the following relationships:

$$t_R = \frac{V_w}{Q} \tag{4.8}$$

$$V_W = \eta \cdot V_c = \eta \cdot \pi r^2 h \tag{4.9}$$

(where V_w is the water volume in the saturated column, Q is the volumetric flow rate, η is the porosity , V_C is the column volume, r is the column radius, and h is the column height) Equation 4.7 can be written in terms of operational parameters:

$$[\mathrm{TCP}]_{\mathrm{eff}} = e^{-\left(k_{obs} \times \frac{\eta \cdot \pi r^2 h}{Q}\right)} [\mathrm{TCP}]_{\mathrm{inf}} \tag{4.10}$$

This relationship was used to size the on-site columns based on laboratory k_{obs} values gathered for each material. Certain operational parameters were fixed: Q was set to a value of 5 mL/min, $[TCP]_{inf}$ was set to 5 μg/L (the target concentration in the influent reservoir), and η was determined by the packing material used (see Table 4.1). r and h were then adjusted to achieve a target $[TCP]_{eff}$ coinciding with the desired TCP removal efficiency for the column.

Two phases of column operation were conducted, with the first designed to assess the performance of Zn64 and Zn1210. The second phase was designed based on the results of the first phase, and used to confirm the initial results and assess potential effects of varying sand mixtures.

4.5.2. Phase I Column Operation

In Phase I of on-site testing, the columns were constructed from two 100-cm PVC pipes connected in series. Pipe diameter was selected using Equation 4.10 and varied depending on media type. Column packing material was either a 25% mixture of Zn64 in sand (Zn64/sand) or Zn1210 (100%). Detailed column design parameters are given in Table S3 of the Supporting Information to the published version of this chapter (*91*).

The Phase I columns were operated for 8-12 weeks with effluent samples collected biweekly. No operational issues were encountered during the first four weeks of

testing. In Week 5, however, leaks related to failures in the polyethylene hose barbs connecting the columns to the influent and effluent tubing were noted in both columns. It appeared that these failures were related to increased backpressure resulting from generation of hydrogen gas (from reduction of water by ZVZ) within the pore space of the column packing material. The columns were modified after Week 5 by replacing the polyethylene hose barbs with larger diameter stainless-steel barbs and pressure relief valves. Columns were taken offline for approximately two weeks while these modifications were made.

Following the Week 5 modifications, the 25% Zn64/sand column operated for the remainder of the planned 12-week test duration. During Week 8, the influent tubing to the lead Zn1210 column segment burst, draining the lead column. The tubing was replaced but flow through the lead Zn1210 column could not be reestablished at the target rate of 5 mL/min, possibly due to either plugging within the column from gas generation or cementation of the packing material while the column was drained.

4.5.3. Phase I Results and Analysis

TCP removal results for the first 8 weeks of Phase I on-site column testing are shown in Figure 4.3 (detailed results are presented in the Supporting Information to the published version of this chapter (*91*), Tables S4-S6). Figure 4.3A shows the percent TCP removal calculated from measured $[TCP]_{inf}$ and $[TCP]_{eff}$ values. This value measures the performance of the specific column, and is influenced by a number of design and operational factors. Also shown are the design removals (according to Equation 4.10). The design removals were 95% for *25% Zn64/sand* and 99% for *Zn1210* (shown as symbols on the left-most side of Figure 4.3A).

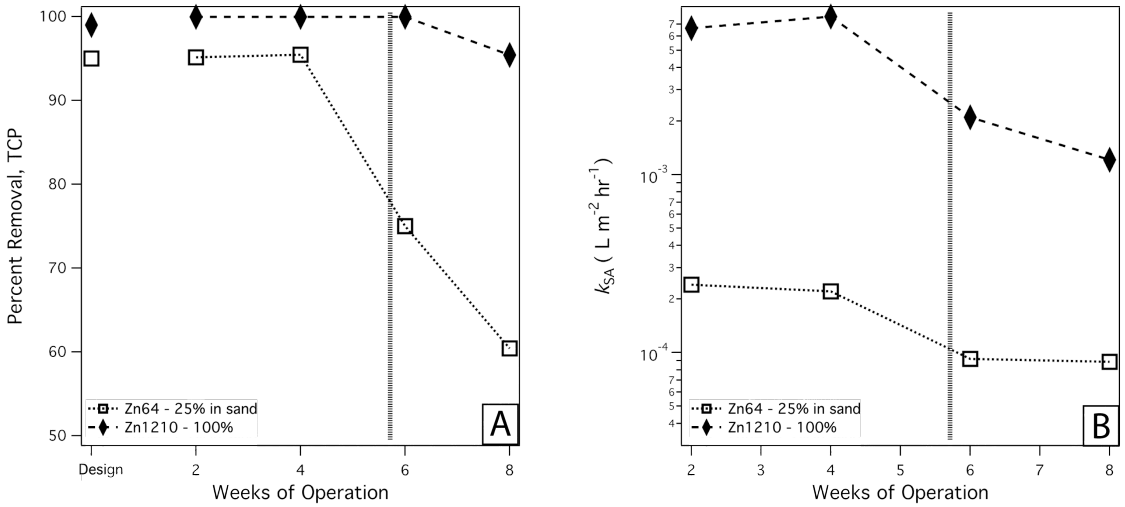

Figure 4.3. Results from Phase I of on-site testing. (A) Percent TCP removal from $[TCP]_{inf}$ and $[TCP]_{eff}$. Design removals are given as symbols at the left-most side of the figure (calculated values); measured results are displayed by length of operation. (B) Surface area normalized rate of TCP disappearance determined from $[TCP]_{inf}$ and $[TCP]_{eff}$ and normalized to factor out differences between the mass of metal present in each column, the specific surface area (SSA) of each material, and the residence time. The vertical dashed line in each figure represents a period of time when the columns were taken off-line for modification.

During the first four weeks of column operation, TCP removal in both the Zn64/sand and Zn1210 columns was similar to the design values. After Week 4, TCP removal in the Zn64/sand column decreased rapidly, falling from approximately 95% at Week 4 to 60% at Week 8. Removal continued to decrease through the remaining weeks of testing, with a removal of 46% during Week 12 (shown in the Supporting Information to the published version of this chapter (*91*), Table S4). In contrast, the Zn1210 column maintained TCP removal similar to the design value, and showed only a moderate decrease in removal at Week 8.

The reactivity of ZVZ in each column over time was measured by calculating a k_{obs}, to factor out performance differences related to t_R, and normalized to k_{SA}, to factor out performance differences related to specific surface area. The resulting k_{SA} values

provide a direct comparison of material reactivity. In contrast to percent removal, this value measures the "specific" reactivity of ZVZ rather than overall column performance. k_{SA} can be compared across columns with differing designs or containing different types of ZVZ, and to values determined in batch reactor experiments. The values of k_{SA} calculated for the first eight weeks of Phase I are shown in Figure 4.3B.

Figure 4.3B shows that the initial reactivity of both Zn64 and Zn1210 was as expected, or higher, based on the bench-scale portion of this study (see Figure 4.2). Material reactivity was lower after 6 weeks of operation. It is unclear whether this decrease in reactivity is due to relatively prolonged exposure to groundwater, or related to a period of design challenges and column modification, during which, the columns were taken off line (see Phase I Column Operation section for details).

During column operation, effluent samples were analyzed to evaluate changes the columns affected on the influent groundwater. This included analysis of TCP degradation products, dissolved Zn, and other geochemical parameters such as alkalinity and ion concentrations (detailed results are presented in the Supporting Information to the published version of this chapter (*91*), Tables S5 and S6).

- Propene, which is the expected product of TCP reduction by ZVZ (*18, 38*), was observed in the column effluents at concentrations on the order of 0.1-0.2 μg/L. These concentrations are lower than expected based on measured TCP loss and stoichiometric conversion to propene. This is likely due to partitioning of propene into gas bubbles that were generated within the column pore space. Biodegradation of propene might also be contributing. Note that, unlike propene,

partitioning of TCP into gas bubbles is not anticipated to be a significant route of TCP loss, based on the Henry's Law constant for TCP.

- Dissolved Zn concentrations measured in column effluents varied from below laboratory analytical detection limits (< 0.0100 mg/L) to a maximum of 0.437 mg/L, compared to influent concentrations of <0.0100 mg/L to 0.0809 mg/L. The effluent concentrations were well below the 5 mg/L secondary maximum contaminant level (MCL) for zinc in drinking water (concentrations above this result in a metallic taste) (*106, 107*). There is currently no primary MCL for zinc in groundwater.
- The concentration of calcium, silica, and the alkalinity decreased significantly between the influent and effluent of the Phase I columns, suggesting that these ions were retained in the column in some form. In contrast to typical ZVI behavior (*108*), sulfate was not removed.

4.5.4. Phase II Column Operation

Given the promising TCP removal results observed during Phase I, a second phase of on-site column testing was carried out to confirm the Phase I results. Phase II placed more focus on Zn1210 because of operational advantages noted in Phase I including, (*i*) ease of handling and mixing (due to larger size), (*ii*) relatively slow decreases in TCP degradation over time (relative to Zn64), and (*iii*) fewer problems with gas build up (presumably due to slower rates of hydrogen gas generation from the reduction of water by ZVZ, although this was not quantified). In addition to testing Zn1210 as the sole column media, Zn1210-sand mixtures were evaluated to test the

potential effects of mixing Zn1210 with sand in various percentages, as might occur in the field as part of a permeable reactive barrier (PRB) style deployment.

The Phase II column design was modified to address the operational issues encountered during Phase I, as previously discussed, as well as to better simulate potential configurations for ex-situ ZVZ deployment (e.g., wellhead treatment). Modifications to column construction for Phase II are described in the Methods section. Column packing and operation was the same as in Phase I. Column packing material included: 25% Zn64 in sand, 100% Zn1210, 33% Zn1210 in sand, and 67% Zn 1210 in sand. Detailed design parameters are given in Table S3 of the Supporting Information to the published version of this chapter (*91*). The columns were run for 12 consecutive weeks and were sampled biweekly. No operational issues were encountered.

4.5.5. Phase II Results and Analysis

TCP removal results for the Phase II columns are shown in Figure 4.4 (detailed results are presented in the Supporting Information to the published version of this chapter (*91*), Tables S7-S11). Figure 4.4A shows the percent TCP removal for each column over the 12 weeks of operation, during which approximately 30 pore volumes of groundwater were flushed through the columns. The design removals of the columns were: 100% for *25% Zn64/sand*; 73% for *33% Zn1210/sand*; 92% for *67% Zn1210/sand*; 98% for *100% Zn1210* (shown as symbols on the left-most side of Figure 4.4A). The design removals were lower than in Phase I due to constructability constraints (i.e., the use of 5-gallon pails, which dictated column diameter and limited column height).

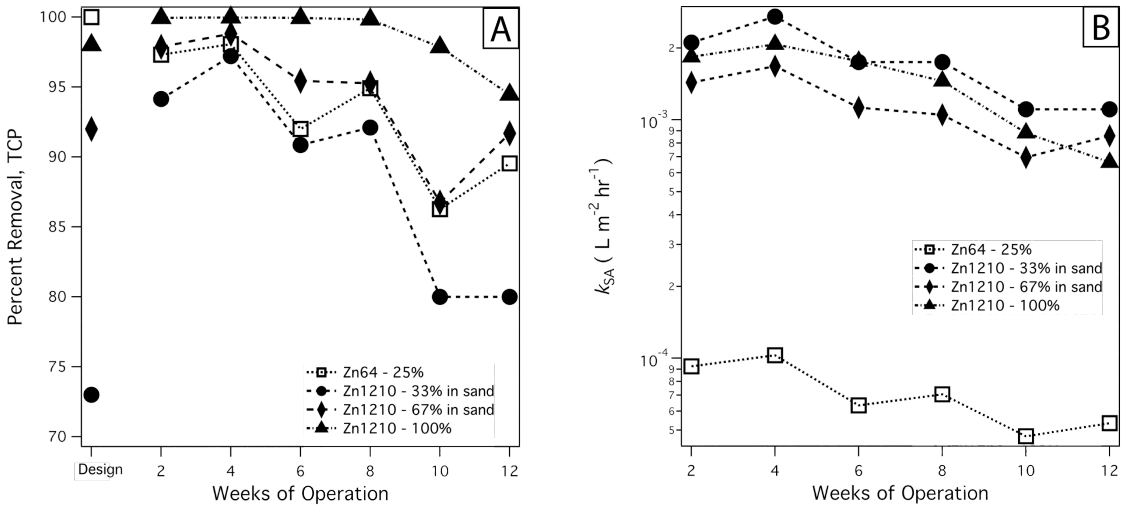

Figure 4.4. Results from Phase II of on-site testing. (A) Percent TCP removal determined from $[TCP]_{inf}$ and $[TCP]_{eff}$. Design removals are given as symbols at the left-most side of the figure (calculated values); measured results are displayed by length of operation. (B) Surface area normalized rate of TCP disappearance determined from $[TCP]_{inf}$ and $[TCP]_{eff}$ and normalized to factor out differences between the mass of metal present in each column, the specific surface area (SSA) of each material, and the residence time.

As seen in Figure 4.4A, the measured percent removal for all Zn1210 columns was similar to or greater than the design removal throughout the 12 weeks of operation. In contrast, the measured percent removal for the 25% Zn64/sand column over the course of operation was lower than the design efficiency. Decreases of about 5% in percent removal from values measured at Week 2 were observed for the 25% Zn64/sand, 100% Zn1210, and 67% Zn1210/sand columns. The 33% Zn1210/sand column showed the greatest decrease in removal (from ~95% to ~80%), but, even at Week 12, the measured removal was still higher than the design removal of 73%.

Figure 4.4B shows k_{SA} values for TCP degradation by ZVZ in each column over time. The initial values are as expected based on the bench-scale portion of this study. The values for Zn1210 in columns containing varying amounts of sand are similar to each other, which suggests that the addition of sand to the column media did not affect ZVZ

reactivity (e.g., through passivating affects related to the presence of silica). Reactivity in each column decreased somewhat with time, but remained within the range of values measured in batch-reactor experiments. The agreement between k_{SA} values measured in the bench- and field-scale portions of this study suggest that the kinetics are highly scalable and that significant inhibitory effects are not imparted by longer-term exposure to groundwater.

Changes to the composition of the efffluent water, in addition to decreased TCP concentrations, were as follows (detailed results are presented in the Supporting Information to the published version of this chapter (*91*), Tables S8-S11):

- Propene was detected in the effluent of each Phase II column throughout the 12 weeks of operation at concentrations on the order of 0.1-0.6 µg/L. As with Phase I, the observed propene concentrations were less than expected based on the observed TCP removal, assuming stoichiometric conversion of TCP to propene. This is not unexpected given that the Phase II columns were designed with a gas headspace above the discharge point of each column segment.
- Concentrations of dissolved zinc in the Phase II column effluent varied from about 0.0394 mg/L to a maximum of 0.244 mg/L, compared to influent concentrations of <0.0100-0.0683 mg/L. The effluent concentrations were well below the 5 mg/L secondary MCL for zinc in drinking water. Based on these concentrations, dissolved zinc is not anticipated to have a negative impact on secondary water quality.
- The concentrations of calcium and silica, as well as the alkalinity decreased significantly between the influent and effluent of all four Phase II columns.

Magnesium concentrations also decreased to a lesser extent. The magnitude of removal appeared to decrease over the course of operation. The observed removal is consistent with previous work, which showed that—in addition to ZnO/Zn(OH)2—Ca, Mg, and Si are present in small concentrations on the surface of ZVZ exposed to groundwater from this site (*18*).

4.6. Results: Post-Operation Characterization

Following on-site testing, select Phase II column media was characterized to assess physical and chemical changes to the material resulting from extended exposure to groundwater. The lead columns from three of the four Phase II columns (containing 25% Zn64/sand, 67% Zn1210/sand, and 100% Zn1210) were disconnected, drained of pore water, and shipped to the laboratory. Upon receipt at the laboratory, column media was analyzed to determine material characteristics, composition, and reactivity.

4.6.1. Material Characteristics

After the field test and delivery to the laboratory, the column segments contained mainly loose granular material with zones that were moderately cemented. The cemented zones broke apart with little effort when handled, leaving it unclear whether the state of the columns as received was representative of operational conditions, or reflective of alterations to the material that occurred during shipping and handling. For these reasons, further testing under more controlled conditions will be necessary to determine changes in porosity and hydraulic conductivity following exposure to groundwater. Based on qualitative observations, however, the behavior of the ZVZ materials with regard to

cementation appears to be very different than ZVI, which tends to cement to a much greater degree when exposed to groundwater.

4.6.2. Composition

In order to assess the current composition of the column media, the Zn materials were separated from the sand in the column media through sieving (results shown in the Supporting Information to the published version of this chapter (*91*), Figure S2). One sample for sieving was taken from the top few inches of the column segment and another was taken from the bottom few inches.

Based on the mass of sand and zinc recovered, both samples from the 67% Zn1210/sand column contained approximately 70% Zn1210 and 30% sand, which is consistent with the nominal packed zinc concentration of 67%. This indicates that after 12 weeks, the majority of the Zn material was still present in the column and did not appear to have redistributed significantly.

A similar analysis of the 25% Zn64/sand column showed that the top portion contained only 4% Zn64, whereas the bottom portion contained 36%, indicating that settling of the material likely occurred. This is consistent with observations of Zn64 settling made during Phase I of on-site testing (the column packing material was visible due to the clear PVC pipe used in column construction). It is probable that the small size of Zn64 makes it more mobile than the larger Zn1210, as well as more difficult to mix uniformly under typical field conditions.

Following sieving, the recovered Zn materials, along with a loose, fine white precipitate also separated during sieving, were analyzed using transmission electron microscopy with energy-dispersive x-ray spectroscopy (TEM/EDS) to determine

composition (results are shown in the Supporting Information to the published version of this chapter (*91*), Figure S3). The fractions identified visually as Zn1210 and Zn64 were confirmed to consist largely of ZVZ. Some zinc oxide (ZnO) was also present and increased levels of Si were noted. The loose white material consisted of $CaCO_3$ (aragonite) with traces of ZnO (EDS shown in the Supporting Information (*91*), Figure S4A). The presence of this precipitate accounts for the decrease in both calcium concentration and alkalinity observed in the column effluents relative to the influent. Aragonite formation is expected based on the concentration of calcium present in the site water and the pH of the system (geochemical speciation model shown in the Supporting Information (*91*), S4B).

4.6.3. Reactivity

In addition to assessing the material characteristics and composition of the column media, changes in ZVZ reactivity related to longer-term exposure to groundwater were assessed in batch reactor experiments conducted under controlled laboratory conditions. This type of post hoc batch testing of column or core materials has proven to be informative in studies with ZVI (*109*). The experiments were conducted using methods described for the bench-scale phase of this project, with post-operation column media replacing the virgin ZVZ materials. Column media samples were collected from the top portion of the column segments and the experiments were conducted in DI water. The resulting k_{obs}, k_M, and k_{SA} values are shown in Table 4.2. For Zn1210, normalization was made based on the nominal percentage of ZVZ present in the columns at construction. Neglecting conversion of ZVZ to ZnO, this is valid for the 100% Zn1210 column and the 67% Zn1210/sand column (the concentration of the latter was supported

in sieving experiments). Normalization of the data from the 25% Zn64/sand column was made based on a 4% Zn64 mass concentration as determined in the sieving experiments. All data fall in or near the range of that collected with virgin ZVZ in the bench-scale portion of this work.

Table 4.2. Reactivity of column media following on-site operation.

Column Media (nominal Zn content)	Assumption of Zn Content	k_{obs}	k_M	k_{SA}
100% Zn1210	100%	1.33×10^{-2}	5.32×10^{-5}	3.32×10^{-3}
67% Zn1210/sand	67%	8.30×10^{-3}	3.32×10^{-5}	2.08×10^{-3}
25% Zn64/sand	4%	6.25×10^{-3}	1.56×10^{-4}	2.50×10^{-4}

4.7. Summary and Conclusions

In order to gain a better understanding of the relative kinetics gathered throughout this study, the TCP degradation rates measured during on-site testing and in post-operation characterization were appended to Figure 4.2 to create Figure 4.5. The data for the Phase II columns at Week 12 are shown as diamonds and the post-operation batch experiments as asterisks.

The Phase II Zn1210 columns (100%, 67% in sand, and 33% in sand) show very close agreement with the Zn1210 (100%) column run at the bench-scale. This agreement suggests both that the results measured in the laboratory were scalable to the larger on-site columns, and that there were no considerable negative effects related to scale-up or longer-term operation of the on-site columns. Additionally, increasing the fraction of sand in the columns did not significantly decrease the intrinsic reactivity of Zn1210 (as assessed by k_{SA}).

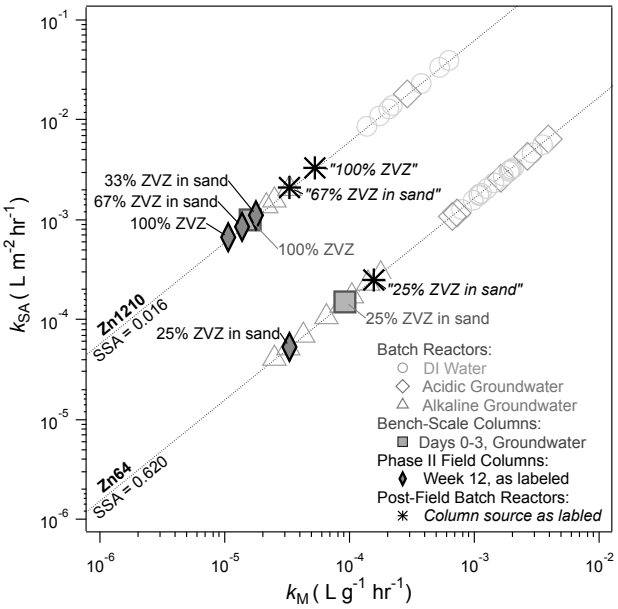

Figure 4.5. TCP degradation kinetics measured in batch reactor experiments containing raw material, laboratory-scale columns, Phase II on-site columns (at Week 12), and batch reactor experiments containing material from Phase II columns post-operation ("post-field batch reactors"). Data collected with Zn64 and Zn1210 fall on separate diagonal lines, the slope of which correspond to the specific surface areas (SSA) of the two materials material in m^2g^{-1}.

In contrast, the 25% Zn64 column from Phase II of on-site testing produced slower kinetics than what was observed in the laboratory-scale column (although the results are still within the range of kinetics measured in batch experiments). The reason for this discrepancy is likely related to variable ZVZ loadings throughout the column, which was not taken into account in the normalization to k_M and k_{SA} (normalization was made assuming the design percentage of 25% Zn64 in sand).

Also shown in Figure 4.5 are data measured in post-operation batch reactor experiments containing on-site column media (shown as asterisks). Based on similar experimental conditions, these data are most comparable to the batch reactor data collected in the initial bench-scale phase of this study. The post-operation data fall at the upper range of data collected with virgin material exposed to alkaline groundwater. This

suggests that there were no significant effects to material reactivity associated with exposure to groundwater during the 12 weeks of column operation (and subsequent exposure to oxygen during shipping) that were not also associated with short-term exposure in the bench-scale portion of the study.

Overall, it appears that the reactivity of ZVZ during Phase II on-site testing was comparable to what was predicted in the bench-scale portion of this study. The kinetics in the on-site columns were slower than what was measured in batch reactor experiments containing DI water or acidic groundwater, but were not significantly slower than batch reactor kinetics measured in alkaline groundwater (the conditions of on-site testing). In addition, it does not appear that changes to the ZVZ materials in the Phase II columns over 12 weeks of operation had a significant negative impact on reactivity towards TCP.

Transformations of the ZVZ appear to be minimal, with some conversion to ZnO, as expected. The accumulation of ZnO and $CaCO_3$ produces minimal cementation in the columns, considerably less than is often observed with ZVI. In addition, the dissolved Zn concentrations in the column effluents are well below the secondary MCL of 5 mg/L, suggesting that ZVZ used in groundwater treatment systems would not have a negative impact on secondary water quality.

Based on overall performance, Zn1210 was the most promising material for treatment of TCP in groundwater. This material showed relatively fast reactivity towards TCP under a range of solution conditions and the intrinsic reactivity of the material was not negatively affected when it was mixed with sand, as might be expected in field deployment as a PRB. Despite the high reactivity towards TCP, the production of hydrogen gas appeared to be minimal compared to Zn64 (although this was not

quantified). In addition, the morphology of Zn1210 (larger flakes) compared to that of Zn64 (fine powder) was more practical in terms of ease of handling and, when mixed with sand in the on-site columns, did not settle or otherwise move through the column.

4.8. Acknowledgements

This work was supported by the Navy Environmental Sustainability Development to Integration Program (NESDI, Project N62583-09-C-0110). Portions of this work were also supported by the Strategic Environmental Research and Development Program (SERDP, Project ER-1458). This report has not been subject to review by either agency and therefore does not necessarily reflect their views and no official endorsement should be inferred.

PART II. PREDICTION OF THE ENVIRONMENTAL FATE OF NOVEL MUNITIONS COMPOUNDS

Chapter 5. Mechanisms and Kinetics of Alkaline Hydrolysis of the Energetic Nitroaromatic Compounds 2,4,6-Trinitrotoluene (TNT) and 2,4-Dinitroanisole (DNAN)[6]

Alexandra J. Salter-Blanc, Eric J. Bylaska, Julia J. Ritchie, and Paul G. Tratnyek[7]

5.1. Abstract

The environmental impacts of energetic compounds can be minimized through the design and selection of new energetic materials with favorable fate properties. Building predictive models to inform this process, however, is difficult because of uncertainties and complexities in some major fate-determining transformation reactions such as the alkaline hydrolysis of energetic nitroaromatic compounds (NACs). Prior work on the mechanisms of the reaction between NACs and OH^- has yielded inconsistent results. In this study, the alkaline hydrolysis of 2,4,6-trinitrotoluene (TNT) and 2,4-Dinitroanisole (DNAN) were investigated with coordinated experimental kinetic measurements and molecular modeling calculations. For TNT, the results suggest reversible formation of an initial product, which is likely either a Meisenheimer complex or a TNT anion formed by abstraction of a methyl proton by OH^-. For DNAN, the results suggest that a Meisenheimer complex is an intermediate in the formation of 2,4-dinitrophenolate. Despite these advances, the remaining uncertainties in the mechanisms of these

[6] Reproduced with permission from Salter-Blanc, A. J.; Bylaska, E. J.; Ritchie, J. J.; Tratnyek , P. G. Mechanisms and kinetics of alkaline hydrolysis of the energetic nitroaromatic compounds 2,4,6-trinitrotoluene (TNT) and 2,4-Dinitroanisole (DNAN). *Environ. Sci. Technol*. **2013**, *47*, 6790-6798 (*11*). Copyright 2013 American Chemical Society.

[7] DNAN disappearance data were collected by Julia J. Ritchie under the mentorship of Alexandra J. Salter-Blanc. Molecular modeling was performed by Eric J. Bylaska.

reactions—and potential variability between the hydrolysis mechanisms for different NACs—mean that it is not yet possible to generalize the results into predictive models (e.g., quantitative structure-activity relationships, QSARs) for hydrolysis of other NACs.

5.2. Introduction

Environmental release of energetic munitions compounds—through manufacture, handling, use (including in testing and training), and disposal—leads to potentially problematic contamination of soils, sediments, and water (*110, 111*). As new energetic materials and formulations are developed, however, their environmental impacts can be minimized through careful design and selection according to the principles of green chemistry (*112-114*). A principle of green chemistry is that the design or selection of new substances should favor chemicals with limited environmental persistence, and degradation products that are relatively benign (*112*).

Achieving this goal—for energetic compounds or other chemicals—requires a sufficient understanding of chemical transformation pathways and kinetics to predict environmental fate. Obtaining the necessary chemical property data for this is a long-standing challenge, in part because the continuously expanding, large, and diverse population of chemicals of environmental concern precludes direct, empirical measurement of more than a small fraction of the data at a reasonable monetary and temporal cost (*40, 115, 116*). This challenge had led to a great deal of interest in predictive models that can estimate contaminant fate properties efficiently and reliably (*41, 115, 116*).

A common approach for predicting chemical properties employs empirical correlations such as linear free energy relationships (LFERs) and quantitative structure

activity relationships (QSARs). These models are obtained by calibration using training sets of response (target) variable data that are usually experimental, and descriptor variable data that are relatively accessible. Such models are widely used as tools for predicting descriptors related to environmental fate and transport for use in regulatory decision-making and experimental prioritization (*41, 115, 116*). In the case of (novel) energetic compounds, however, the challenge of obtaining experimentally determined environmental fate properties for model calibration is greatly increased by factors that are nearly unique to this type of material: (*i*) access to many of the materials is highly restricted, (*ii*) few environmental laboratories are equipped to perform experiments with such materials, and (*iii*) novel materials of this type are rarely prepared in sufficient quantities for environmental fate property testing.

In principle, the challenge of obtaining response variable data such as rate constants for model calibration can be overcome by determining the values from first principles (i.e., using molecular modeling). Given an understanding of the environmental fate mechanisms for a given family of compounds, reactions of novel compounds within this family can be modeled computationally to determine activation parameters for the reactions. According to the principles of transition state theory, these activation parameters can then be used to calculate rate constants for the reactions (*4*). The result would be a correlation calibrated fully *in silico*, which could then be validated with obtainable experimental data for energetic (and model nonenergetic) compounds.

One family to which this method might be applied is energetic nitroaromatic compounds (NACs). The most familiar member of this group is 2,4,6-trinitrotoluene (TNT), which has long been used in a variety of energetic materials. Also included is a

shock-insensitive alternative to TNT, 2,4-dinitroanisole (DNAN) (*117*), which is used in modern munitions formulations such as PAX-21 (*118*). While TNT and DNAN comprise a subfamily of substituted nitrobenzenes, other NACs used in emerging munitions formulations include substituted heterocycles, such as 5-nitro-1,2,4-triazol-3-one (NTO)—another insensitive replacement for TNT that is used in emerging munitions formulations (*117*)—and polyaromatic compounds. A representative sample of energetic NACs is shown in Figure 5.1; these and many more have been described previously (*119, 120*).

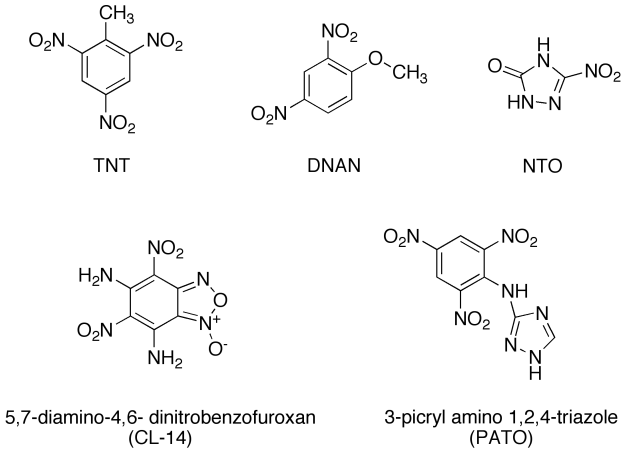

Figure 5.1. A selection of energetic NACs included or considered for use in munitions formulations.

The main abiotic transformation processes influencing the environmental fate of NACs in groundwater are reduction and alkaline hydrolysis (*121*). While the pathways and kinetics associated with the reduction of NACs have been studied extensively (e.g., (*30-33, 122*)), the pathways associated with alkaline hydrolysis are not well characterized, despite considerable proof-of-concept testing of this process for engineered remediation of TNT-contaminated wastewaters (*13, 14, 123-129*). In the case of TNT, there are significant inconsistencies in the experimental data, which likely arise from the

sensitivity of the reaction to the nature of the solvent (*130, 131*), difficulty observing products in water due to their poor solubility (*13*), and the influence of the concentration ratio between TNT and base on product distribution (*130, 131*). Previous computational studies of TNT reaction energetics have also failed to definitively determine the pathways of its reaction with OH^- (*132-134*).

This incomplete understanding of the mechanisms of TNT hydrolysis in natural and engineered systems inhibits the prediction of degradation properties of future energetic NACs through the use of correlations calibrated with data determined fully *in silico*. Our goal in this paper is to clarify the mechanisms of TNT degradation by OH^- in water by taking a combined approach that emphasizes reconciliation of both experimental and computational data. An analysis of the kinetics of TNT disappearance in the presence of OH^- is presented and used to determine the experimental activation free energies ($\Delta G^{\ddagger}$) and reaction free energies (ΔG_{rxn}) for the processes. Also presented are $\Delta G^{\ddagger}$ and ΔG_{rxn} values for possible mechanisms of TNT degradation determined using molecular modeling. The measured and modeled results are then compared to assess which mechanisms predominate. Also reported is an analogous analysis for DNAN, which is structurally similar to TNT.

5.3. Methods

5.3.1. Reagents

Stock solutions of NACs were prepared by dissolving solid-phase TNT (ChemService, Inc.; West Chester, PA) or DNAN (Alfa Aesar; Ward Hill, MA) in HPLC-grade acetonitrile (Fisher Scientific; Waltham, MA) to achieve a concentration of

10 g/L. All deionized (DI) water used was obtained from a Milli-Q system (EMD Millipore; Billerica, MA). HPLC mobile-phase components consisted of DI water and HPLC-grade methanol (Fisher Scientific; Waltham, MA). Phosphate buffers were prepared from sodium phosphate (mono- and di-basic) (Fisher Scientific; Waltham, MA) and adjusted with NaOH (Aldrich; St. Louis, MO) to pH 11.0, 11.7, and 12.0. Acidified acetonitrile was prepared by adding sufficient sulfuric acid to HPLC-grade acetonitrile to neutralize an equal volume of corresponding buffer.

5.3.2. Batch Experiments

Batch experiments were carried out in 20-mL amber VOA vials capped with Teflon-lined silicon septa (SUN Sri; Rockwood, TN). Each vial initially contained 20 mL phosphate buffer (50 mM) at pH 11.0, 11.7, or 12.0. Vials were temperature equilibrated in water baths or in a cold room to 11.0, 25.0, 40.0, 55.0, or 65.0 °C. After temperature equilibration, TNT or DNAN was introduced to the reaction vial by injecting 200 µL of a 10-g/L stock solution prepared in acetonitrile (reaction initiation). Following introduction of TNT or DNAN, the vials were shaken by hand for ~1 min (in the water bath) to ensure proper mixing. 1-mL aliquots were removed at specified times and quenched by mixing with an equal volume of acidified acetonitrile.

Quenched aliquots were analyzed by high-pressure liquid chromatography (HPLC). The HPLC setup included a Varian ProStar 210 solvent delivery module, 410 autosampler, and 330 photodiode array detector, with a Platinum C18 5µ 250-mm x 4.6-mm column (Grace; Deerfield, IL). The mobile phase consisted of 1:1 DI water:methanol and was pumped at a flow rate of 1 mL min^{-1}.

5.3.3. Kinetic Modeling

The kinetics of TNT disappearance were fit assuming the reaction proceeds by a sequence of reversible and irreversible steps

$$\text{TNT} + \text{OH}^- \underset{k_{-1}}{\overset{k_1}{\rightleftharpoons}} \text{P1} \xrightarrow{k_2} \text{P2} \qquad \text{(Scheme 5.1)}$$

where P1 is the first product, P2 is the second product, k_1 is the second-order rate constant for the forward portion of the first reaction, k_{-1} is the rate constant reverse portion of the first reaction, and k_2 is the rate constant for the second reaction. The reaction was simplified by assuming constant hydroxide concentration in the buffered system and then treating the formation of P1 as a pseudo-first-order process

$$\text{TNT} \underset{k_{-1}}{\overset{k_{1,obs}}{\rightleftharpoons}} \text{P1} \xrightarrow{k_2} \text{P2} \qquad \text{(Scheme 5.2)}$$

where $k_{1,obs}$ is the observed pseudo-first-order rate constant for formation of P1.

Rate constants were determined by fitting concentration vs. time data for TNT. The data were fit by simultaneous numerical solution to the following differential equations (Equation 5.1 and Equation 5.2) using IGOR Pro (Wavemetrics; Lake Oswego, OR).

$$\frac{d[\text{TNT}]}{dt} = -k_{1,obs}[\text{TNT}] + k_{-1}[\text{P1}] \qquad (5.1)$$

$$\frac{d[\text{P1}]}{dt} = k_{1,obs}[\text{TNT}] - k_{-1}[\text{P1}] - k_2[\text{P1}] \qquad (5.2)$$

Data sets obtained at different pH values, but at the same temperature were fit globally (i.e., simultaneously) to obtain values of $k_{1,obs}$ and [TNT] for each pH condition and

single, global values for each k_{-1} and k_2 (as these are pH-independent values according to Scheme 1).

DNAN disappearance was fit to a simple, irreversible pseudo-first-order model as described in Schemes 3 and 4,

$$\text{DNAN} + \text{OH}^- \xrightarrow{k_1} \text{P} \qquad \text{(Scheme 5.3)}$$

$$\text{DNAN} \xrightarrow{k_{1,obs}} \text{P} \qquad \text{(Scheme 5.4)}$$

where P is the product of the reaction, k_1 is the second-order rate constant, and $k_{1,obs}$ is the observed pseudo-first-order rate constant. The data was fit to a pseudo-first-order model to obtain $k_{1,obs}$.

Plots of $k_{1,obs}$ vs. [OH^-] (Appendix B, Table B.1 and Table B.3) for both TNT and DNAN confirmed that the forward reactions characterized by $k_{1,obs}$ were pseudo-first order with respect to [OH^-]. Given this, second-order rate constants, k_1, for TNT and DNAN were determined by linear regression to the $k_{1,obs}$ vs. [OH^-] data for each temperature.

5.3.4. Molecular Modeling

In this study, the solution phase ΔG_{rxn} and $\Delta G^{\ddagger}$ were directly calculated from gas-phase reaction energy, entropy, and solvation energy differences using electronic structure calculations, continuum solvation models, and gas-phase entropy estimates. All calculations were performed using the NWChem program suite (*135*). The electronic structure calculations were either performed using density functional theory (DFT) (*136*) with the B3LYP (*137, 138*) exchange correlation potential, or with second-order Møller-Plesset perturbation theory (MP2) (*139*). In all cases, the 6-311++G(2d,2p) basis set was

used (obtained from the Extensible Computational Chemistry Environmental Basis Set Database (*140*)). The solvation energies were estimated using the self-consistent reaction field theory of Klamt and Schüürmann (COSMO) (*141*), with the cavity defined by a set of overlapping atomic spheres with radii suggested by Stefanovich and Truong (H 1.172 Å, C- 2.096 Å, C = 1.635 Å, O 1.576 Å and N 2.126 Å) (*142*). The dielectric constant of water used for all of the solvation calculations was 78.4. The solvent cavity discretization was generated from the surfaces of nonoverlapping spheres that were discretized by an iterative refinement of triangles starting from a regular octahedron. Three refinement levels, equivalent to 128 points per sphere, were used to define the solvent cavity in these calculations.

The geometries and harmonic frequencies for the reactants, products, and transition states were consistently optimized using the B3LYP calculation with COSMO. Transitions states were determined for the Meisenheimer and proton abstraction reactions by performing constrained optimizations at a series of C-OH and CH-OH bond distances. The transition state for the S_N2 reactions were found by a quasi-Newton (BFGS) saddle point search initialized with d(C-OH) = 1.45 Å and d(C-NO_2) = 1.65 Å. The virtual entropies for each compound were estimated using formulas derived from statistical mechanics that are broken into translational, rotational, and frequency terms. In addition to the COSMO correction, cavitation, and dispersion contributions to the solvation energy were added *a posteriori* using empirically derived expressions that depend only on the solvent accessible surface area. In this study, we used the parameterized formula given by Sitkoff *et al*. (*143*).

$$\Delta G_{cav+disp} = \gamma A + b \tag{5.3}$$

where A is the solvent-accessible surface area and γ and b are constants set to 5 cal mol^{-1} $Å^{-2}$ and 0.86 kcal mol^{-1}, respectively. Sitkoff *et al.* fit the constants γ and b to the experimentally determined free energies of solvation of alkanes (*144*) by using a least-squares fit.

5.4. Results and Discussion

5.4.1. Formulation of Candidate Mechanisms

Generally, NACs can interact with bases (nucleophiles) to form charge-transfer complexes, radical anions, σ-complexes, or proton abstraction products (*145*). Formation of σ-complexes has been observed from the interaction of various nucleophiles with a wide range of NACs (*146*). σ-Complexes are formed as intermediates in the Ar-S_N mechanism of nucleophilic aromatic substitution (*146, 147*). This reaction involves reversible addition of a nucleophile to an electron-deficient carbon on an aromatic ring (in a rate determining step) followed by elimination of a leaving group from the same ring carbon (*146, 147*). In cases where this intermediate is stable enough to be isolated or detected, it is known as a Meisenheimer complex (*146-148*). Stabilizing factors include the presence of electron withdrawing groups on the aromatic ring and poor leaving groups (*147*). Meisenheimer complexes have been studied extensively (*146*), however, most of these studies were performed in nonaqueous media, and evidence for this reaction occurring under environmentally-relevant (natural and engineered) conditions is limited.

Of the prior studies that characterize the reaction of TNT and OH^- in water, several have hypothesized that a Meisenheimer complex is the initial product (*13, 125,*

146). However, demonstrating the participation of this intermediate is difficult because of its short lifetime and limited solubility in water. The main evidence for its formation is from NMR spectra that were obtained while following the reaction in acetone (due to solubility constraints in water) (*13*). Whether these conclusions apply to aqueous media is uncertain, because other studies in nonaqueous or partially aqueous systems have shown that the initial product in the reaction of TNT with base is strongly influenced by the solvent (*130, 131*).

Alternatively, it has been suggested that direct nitro substitution could be the initial step in this reaction, based on NMR analysis of the final polymeric reaction products formed in water (*127*). A third possible initial step is the abstraction of a methyl proton, which has been reported to form along with or instead of a Meisenheimer complex in nonaqueous or partially aqueous systems, possibly leading to the formation of a Janovsky complex (*130, 131*). A recent theoretical study using DFT concluded that Meisenheimer-complex formation and/or proton abstraction are the most likely initial reactions in the interaction of TNT with OH^- (*132*). All of the proposed initial steps for reaction between TNT and OH^- are summarized in Figure 5.2.

Prior work on the reaction of DNAN with OH^- is more limited. The reaction between DNAN and OH^- has been suggested to occur through substitution of the methoxy group, leading to 2,4-dinitophenol (*149, 150*), which may in turn react with OH^- to form 2,4-dinitrophenolate (*150*). This reaction may take place through OH^- addition at the C1 carbon (as shown in Figure 5.3) (*149*), i.e., through the formation of a Meisenheimer complex. Meisenheimer complex formation at the C1 carbon—as well as at other possible addition sites—is shown in Figure 5.3 as an initial step in methoxy

substitution. In addition, we considered proton abstraction and direct nitro substitution reactions in order to compare the results with those calculated for TNT, although, to our knowledge, these reactions have not been observed experimentally.

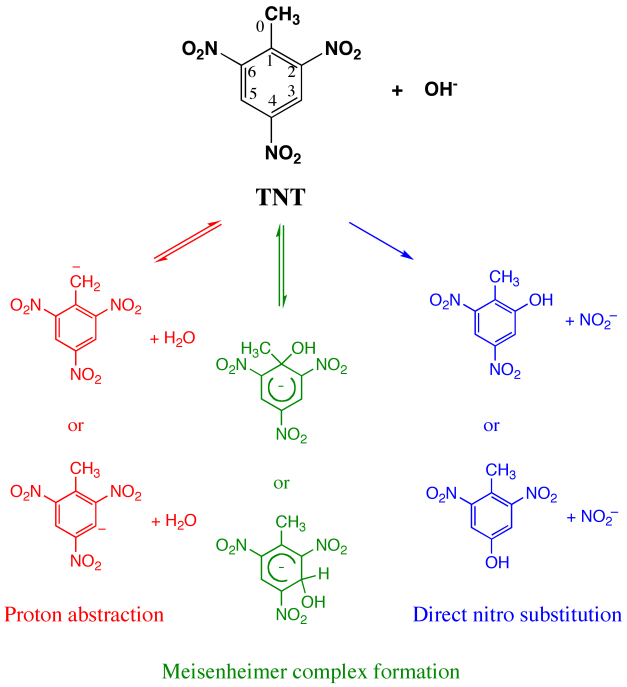

Figure 5.2. Alternative initial steps in the mechanism of reaction between TNT and OH^-.

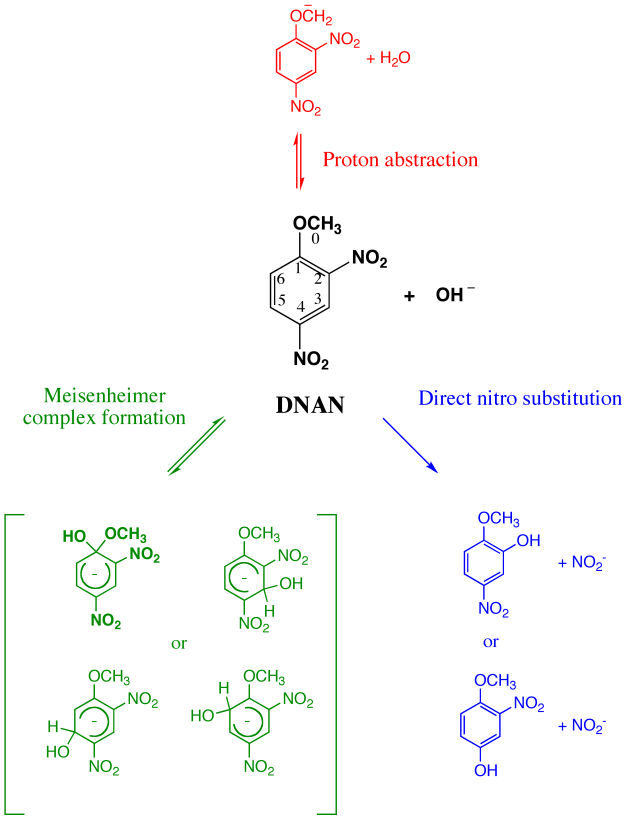

Figure 5.3. Alternative initial steps in the mechanism of reaction between DNAN and OH^-. Meisenheimer complex formation at C1, which has been hypothesized based on experimental observations (*149*), is shown in bold.

5.4.2. Experimental Kinetic Data

In order to provide experimental evidence for evaluating the alternative mechanisms of interaction between TNT and DNAN with OH^-, the disappearance kinetics for these NACs were determined in aqueous phosphate buffer at three pH's (from 11.0 to 12.0) and four temperatures (from 11 to 55 °C for TNT, and 25 to 65 °C for DNAN). Representative concentration vs. time data are shown in Figure 5.4 for TNT at 11 °C and DNAN at 25 °C. The complete data set—including additional data for TNT at 25, 40, and 55 °C and for DNAN at 40, 55, and 65 °C—is given in the Appendix B, Table B.1 and Table B.3.

For both TNT and DNAN, the kinetics of reaction with OH^- appeared to be first order with respect to both the NAC and OH^- (second-order overall). TNT disappearance did not show simple, irreversible pseudo-first-order behavior, but was better fit to a model that includes a reversible first step, followed by an irreversible second step (as described in Schemes 1 and 2). A similar model has been used in prior work on the kinetics of intermediate formation upon the reaction of TNT with OH^- (*13*). Fitting this model to the data for TNT disappearance gave rate constants for each step, which are summarized in Appendix B, Table B.2. Unlike TNT, the disappearance of DNAN was well fit with a simple model for irreversible, pseudo-first order kinetics (Schemes 3 and 4). Rate constants determined from this fit are summarized in Appendix B, Table B.4.

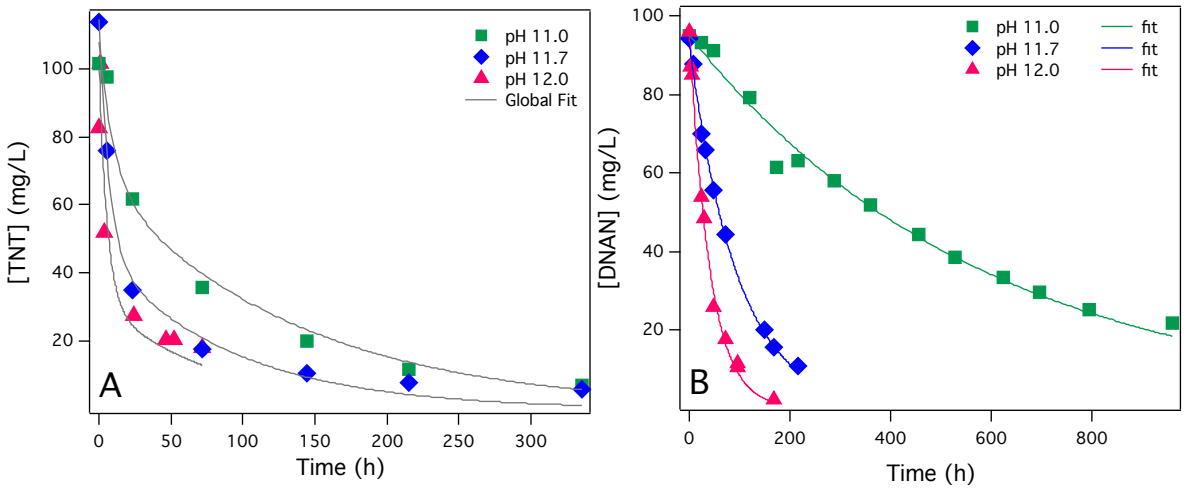

Figure 5.4. (A) TNT disappearance at 11 °C for pH 11.0, 11.7, and 12.0. All three datasets were fit with constraints that gave global values for k_{-1} and k_2 but separate values for $k_{1,obs}$ at each pH. Data for 25, 40, and 55 °C are shown in Appendix B, Table B.1. (B) DNAN disappearance at 25 °C for pH 11.0, 11.7, and 12.0. Each data set was fit individually to determine $k_{1,obs}$. Data for 40, 55, and 65 °C are shown in Appendix B, Table B.3.

5.4.3. Determination of Free Energies from Experimental Kinetics

To generalize the results obtained from batch experiments with TNT and DNAN, and to facilitate comparisons between these results and data obtained from computational modeling (next section), the rate constants for each temperature were used to obtain experimental free energies for the reactions of TNT and DNAN with OH^-. This was done by applying transition state theory (*4*), which relates the rate of a reaction to the energy of the transition state, specifically, the free energy of activation ($\Delta G^{\ddagger}$). This relationship is defined by the Eyring equation (*4*) (Equation 5.4),

$$k = \frac{k_B T}{h} \cdot e^{-\Delta G^{\ddagger}/RT} \cdot (1 \text{ mol L}^{-1})^{1-n} \tag{5.4}$$

where k is the rate constant in molar concentration units (if applicable), k_B is the Boltzmann constant, T is temperature, h is Planck's constant, $\Delta G^{\ddagger}$ is the molar free energy of activation, R is the gas constant, and n is the order of the reaction. Activation parameters were determined from the rate data using a linearized version of the Eyring equation (Equation 5.5),

$$\ln\left(\frac{k \cdot h}{k_B T (\text{mol L}^{-1})^{1-n}}\right) = \frac{\Delta S^{\ddagger}}{R} - \frac{\Delta H^{\ddagger}}{RT} \tag{5.5}$$

where $\Delta S^{\ddagger}$ is the molar entropy of activation and $\Delta H^{\ddagger}$ is the molar enthalpy of activation.

Figure 5.5 shows Eyring plots for the proposed steps in the reaction of TNT with OH^-, including both the forward and reverse formation of the first product, P1, and subsequent degradation of P1 to P2. The plots show adjusted values of k_1, k_{-1}, and k_2 plotted vs. inverse temperature. Also shown in Figure 5.5 are kinetic data for the reaction of TNT with OH^- previously reported by Mills et al. (*13*), who fit their data assuming reversible Meisenheimer-complex formation (using a kinetic model that accounts for

reversibility in the initial step), and Emmrich[22] who obtained k_1 by fitting to an irreversible, pseudo-first-order model.

As seen in Figure 5.5, our data for k_1 (associated with the reaction TNT + OH^- → P1) show good agreement with those reported previously. In the case of k_{-1} (associated with the reaction TNT + OH^- ← P1), our data do not agree as closely with the data reported by Mills et al. (*13*). Our data do, however, show a more linear relationship and smaller uncertainties. The reason for the inconsistency between these results is likely that Mills et al. did not consider the effect of the second reaction (P1 → P2) in their determination of k_1 and k_{-1}. They made the assumption that the second reaction does not affect the disappearance of TNT at "low" hydroxide concentrations (0.01-0.1 mol dm^{-3}), and so they used data gathered in this concentration range to study the initial reaction independently. Their kinetics, which were typically measured over two half-lives, fit well to a model based on this assumption. Our data, however, show that the kinetics of TNT disappearance deviate from pseudo-first-order after two half-lives (most of our experiments were run for 4–8 half-lives), and that this deviation is consistent with the contribution of the second reaction (P1 → P2) to the rate of TNT disappearance. For this reason, we fit only our data to Equation 5.5 to determine $\Delta S^{\ddagger}$ and $\Delta H^{\ddagger}$ for each reaction shown in Figure 5.5. These were subsequently used to calculate $\Delta G^{\ddagger}$ at 25 °C. All of these results are tabulated in Table 5.1.

In addition to determining activation parameters for the reaction of TNT, a similar treatment was used to extract thermodynamic values from the kinetic data for DNAN. The results are shown in Figure 5.6 as an Eyring plot for the second-order rate constant, k_1. Error bars on k_1 represent the uncertainties (±1 standard deviation) from the fit of $k_{1,obs}$

vs. [OH^-] (Appendix B, Table B.1). While the data point corresponding to the experiments performed at 65 °C shows relatively large error, exclusion of this point does not significantly change the value of $\Delta G^{\ddagger}$ calculated from the linear fit. Superimposed on the figure are the rate constants for the reaction of DNAN with OH^- that were reported by Murto and Tommila (*150*), which were also obtained by modeling their data with pseudo-first-order kinetics. While their data set shows an essentially identical slope to the result from this study, their intercept is about an order of magnitude smaller (note that, according to the Eyring equation, the slope is related to $\Delta H^{\ddagger}$ and the intercept is related to $\Delta S^{\ddagger}$). Absent any *a priori* explanation for this difference, we have fit each data set to the linearized Eyring equation and reported both sets of results in Table 5.1. There is no significant difference between the values of $\Delta G^{\ddagger}$ determined from these two data sets.

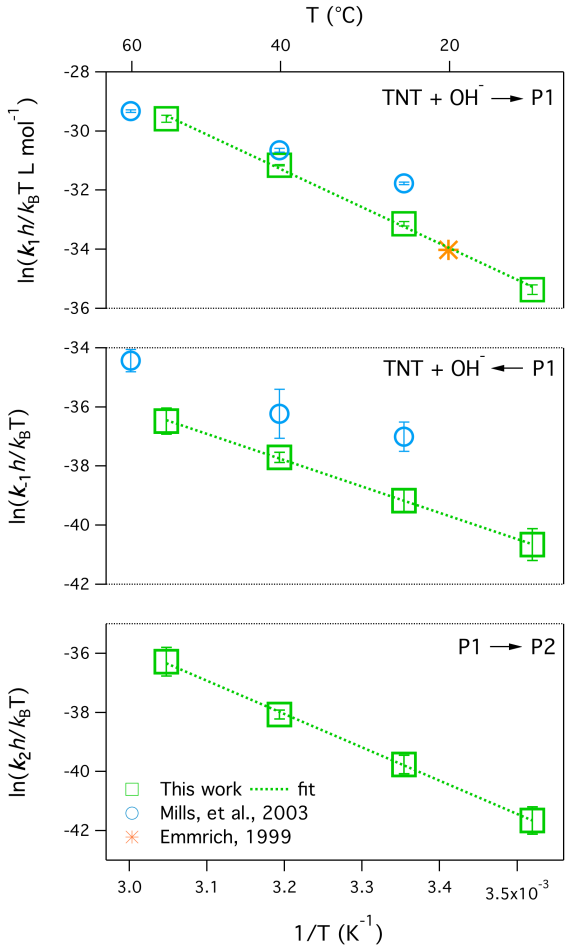

Figure 5.5. Eyring plots for the reaction of TNT with hydroxide. Each panel in the figure displays rate constants for a different step in the proposed reaction of TNT with OH^- (as described in Scheme 1) according to a linearized version of the Eyring equation (Equation 5.5). The top panel of the figure corresponds to k_1 and the forward portion of the first reaction (TNT + OH^- ⟶ P1), the middle panel corresponds to k_{-1} and the reverse portion of the first reaction (TNT + OH^- ⟵ P1), and the bottom panel corresponds to k_2 and the second reaction (P1 ⟶ P2). Also shown are data reported by Mills et al. (*13*) and Emmrich (*14*). Error bars are shown for all data, with the exception of the value reported by Emmrich, for which no uncertainty was reported.

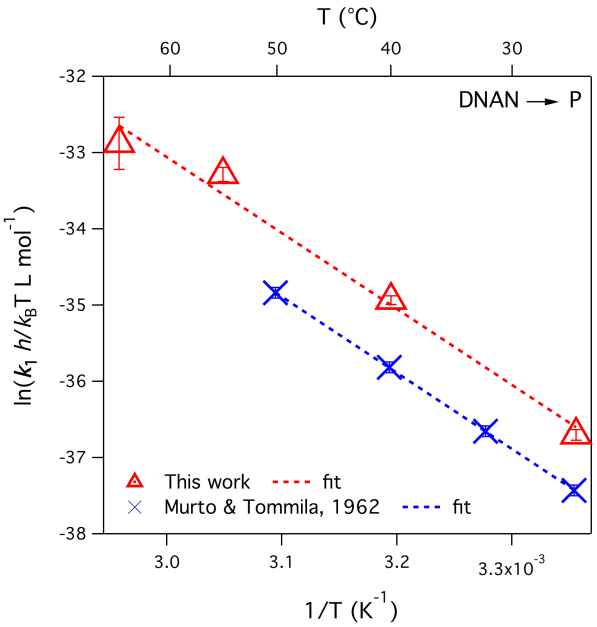

Figure 5.6. Eyring plot for the reaction of DNAN with hydroxide. A transformation of the second-order rate constant, k_1, is plotted vs. inverse temperature (based on a linearized version of the Eyring equation). Data reported in this work are shown as red triangles. Error bars on k_1 represent the error (±1 standard deviation) from the fit of $k_{1,obs}$ vs. [OH^-] (Appendix B, Table B.1). Data reported by Murto and Tommila (*150*) are shown as blue X's. Each data set was fit linearly to determine Eyring parameters given in Table 5.1.

Table 5.1. Eyring fit and activation parameters for TNT and DNAN. Except where indicated, all parameters reported were determined by fitting data original to this work.

Parent	Rxn	Eyring Slope (K)	Eyring Intercept	$\Delta H^{\ddagger}$ (kcal mol^{-1})	$\Delta S^{\ddagger}$ (kcal K^{-1} mol^{-1})	$\Delta G^{\ddagger}$ [a] (kcal mol^{-1})
TNT	TNT → P1	-12270 ± 430	7.9 ± 1.4	24.370 ± 0.030	0.01573 ± 0.00051	19.6810 ± 0.0016
TNT	TNT ← P1	-8882 ± 49	-9.38 ± 0.16	17.63866 ± 0.00055	-0.018634 ± 5.5 x 10^{-6}	23.194517 ± 3.1 x 10^{-5}
TNT	P1 → P2	-11282 ± 97	-1.95 ± 0.32	22.4061 ± 0.0017	-0.00388 ±0.00010	23.56230 ± 0.00073
DNAN	DNAN → P	-9960 ± 870	-3.2 ± 2.7	19.79 ± 0.15	-0.0063 ± 0.0046	21.66 ± 0.54
		-9986 ± 32 [b]	-3.9324 ± 0.10 [b]	19.83200 ± 2.0 x 10^{-4} [b]	-0.0078097 ± -5.4 x 10^{-6} [b]	22.160473 ± 1.0 x 10^{-5} [b]

a) Calculated at 25 °C from $\Delta H^{\ddagger}$ and $\Delta S^{\ddagger}$. *b*) Determined by fitting data reported by Murto and Tommila (*150*).

5.4.4. Determination of Free Energies from Molecular Modeling

In addition to measuring the rate constants and determining free energies for TNT and DNAN experimentally, solution phase reaction energies and activation barriers for the candidate mechanisms shown in Figure 5.2 and Figure 5.3 were determined using electronic structure calculations. Data determined at the COSMO B3LYP and COSMO MP2 levels are summarized in Figure 5.7, which shows ΔG_{rxn} and $\Delta G^{\ddagger}$ vs. shorthand labels for each candidate mechanism. This shorthand represents the mechanism ("MC" = Meisenheimer-complex formation, "Sub" = direct nitro substitution, "PA" = proton abstraction) and reaction location (e.g., "@1" = reaction occurring at C1, as labeled in Figure 5.2 and Figure 5.3). Also shown are data previously reported by Hill et al. (*132*), which were modeled in the solution phase using DFT at the SMD (Pauling)/M06-2X/6-31+G(d,p) level (*151, 152*). The values for all the computational results summarized in Figure 5.7 are given in Appendix B, Table B.5.

In Figure 5.7, it can be seen that there is considerable variation in the absolute values of ΔG_{rxn} for a given mechanism calculated at different levels of theory (with average absolute differences in ΔG_{rxn} ranging from 5.5 kcal mol^{-1} between the COSMO B3LYP data and the COSMO MP2 data, and 11 kcal mol^{-1} between the COSMO B3LYP data and the data reported by Hill et al.). Despite this variation, there is generally good agreement in the relative values of ΔG_{rxn} between the mechanisms, especially between the COSMO B3LYP and COSMO MP2 data. The trends in $\Delta G^{\ddagger}$ are less consistent. The average absolute differences from COSMO B3LYP, however, are slightly smaller than seen for ΔG_{rxn} (5.0 kcal mol^{-1} for COSMO MP2 and 7.2 kcal mol^{-1} for Hill et. al.). While our results are not sufficient to determine the absolute accuracy of these calculations (as

this was not within the scope of this paper), our ΔG_{rxn} values can be used to determine the relative favorability of each of the candidate mechanisms, and our $\Delta G^{\ddagger}$ values can be used to determine the relative kinetics.

From the ΔG_{rxn} values for both TNT and DNAN shown in Figure 5.7, it is clear that direct nitro substitution at C2 and C4 (Sub@2 and Sub@4) are the most thermodynamically favorable mechanisms. The ΔG_{rxn} values for TNT at both reaction sites are ~10 kcal mol^{-1} more negative than the analogous reactions on DNAN, suggesting TNT is the more favorable of the two. This is easily rationalized by the additional electron-withdrawing group on TNT. The $\Delta G^{\ddagger}$ values for Sub@2 and Sub@4 show a similar trend to the ΔG_{rxn} values, with the $\Delta G^{\ddagger}$ values for TNT being ~10 kcal mol^{-1} lower than the values for DNAN. The high values of $\Delta G^{\ddagger}$ for DNAN suggest that the reactions should occur more slowly than for TNT and are not likely to be kinetically significant.

Compared to direct nitro substitution, the ΔG_{rxn} values for Meisenheimer-complex formation and proton abstraction are less favorable for both TNT and DNAN. ΔG_{rxn} values for Meisenheimer-complex formation at all sites are near zero for TNT and endothermic by at least 6 kcal mol^{-1} for DNAN. Proton abstraction at the methyl group (PA@0) on TNT is between −20 and 0 kcal mol^{-1} and PA@3 is endothermic by about 10 kcal mol^{-1}. Proton abstraction reactions on DNAN are also endothermic and not thermodynamically feasible (results not shown).

Overall, the computational results predict that TNT can undergo direct substitution (Sub@2 and Sub@4), Meisenheimer-compex formation (MC@1 and MC@3), and proton abstraction at the methyl group (PA@0). For DNAN, the

computational results suggest that the direct substitution reactions, while thermodynamically feasible, are not likely because of their high activation barriers, and that only MC@1 and MC@3 are kinetically and thermodynamically favorable.

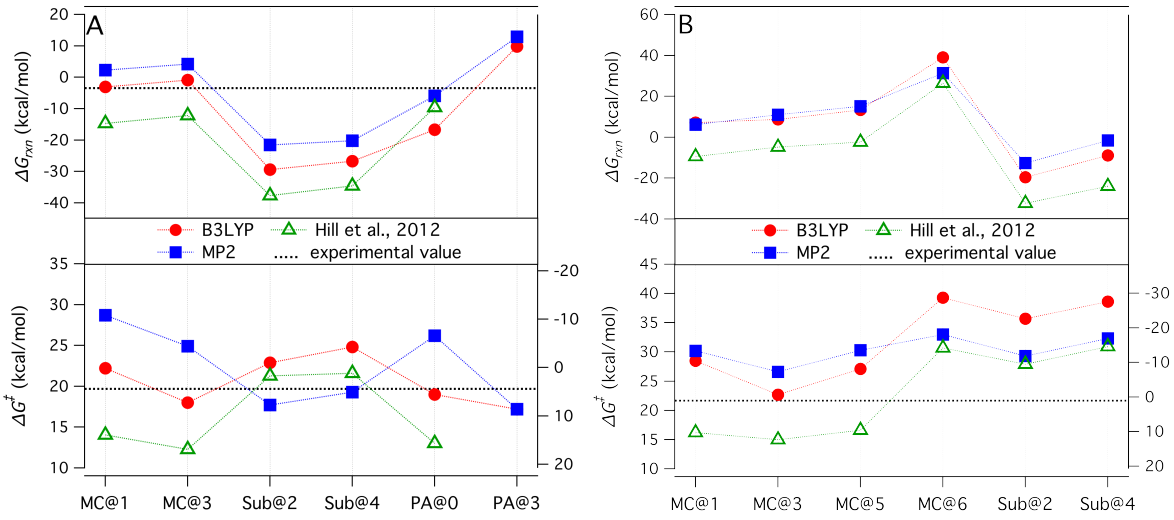

Figure 5.7. Computationally determined reaction free energies (ΔG_{rxn}) and activation free energies ($\Delta G^{\ddagger}$) for (A) TNT and (B) DNAN. Values are shown for the possible initial reaction steps determined at the COSMO B3LYP and COSMO MP2 levels. Also shown are data reported by Hill et al (*132*). Experimentally determined values (derived from fits to the kinetic results) are shown as black dotted lines.

5.4.5. Reconciling the Computational Results with Experimental Observations

The likelihood of the candidate mechanisms can be further evaluated by comparing the results of molecular modeling to experimental observations. Ideally, this might be based on a comparison of computationally derived ΔG_{rxn} and $\Delta G^{\ddagger}$ values to those determined experimentally in order to determine likely mechanisms. To facilitate such a comparison, Figure 5.7 has been annotated with experimental values of $\Delta G^{\ddagger}$ for TNT and DNAN and an experimental value of ΔG_{rxn} for TNT. The experimental ΔG_{rxn} was determined from the difference in the experimental $\Delta G^{\ddagger}$ values for the forward and reverse steps in the reaction of TNT with OH^{-}. This calculation could not be performed

for DNAN since the initial step in the reaction with OH^- was not reversible. As seen in Figure 5.7, however, different levels of theory produce a substantial range of computed values of $\Delta G^{\ddagger}$. Because of this variability, and because there is no way to know *a priori* which level of theory best reflects experimental observations, we have not made a direct comparison of the computational and experimental values for ΔG_{rxn} and $\Delta G^{\ddagger}$. Other comparisons can be made, however, which lead to a number of significant conclusions.

In the case of TNT, kinetic modeling of the experimental results, shown in Figure 5.4 (and in Appendix B, Table B.1 and Table B.3), suggests a reversible reaction. Assuming reversibility, the ΔG_{rxn} value is expected to be close to 0 kcal mol^{-1} (due to the forward and reverse reactions having similar values of $\Delta G^{\ddagger}$). This is consistent with the experimental ΔG_{rxn} value of −3.5 kcal mol^{-1}. Since the computed ΔG_{rxn} values for Sub@2 and Sub@4 are approximately −25 to −30 kcal mol^{-1}, these mechanisms are likely too favorable to exhibit reversibility. The ΔG_{rxn} values for MC@1, MC@3, PA@0, and PA@3 are more consistent with a reversible reaction.

Based on these considerations and the analysis given in the previous section, MC@1, MC@3, and PA@0 appear to be the most likely initial steps in the reaction between TNT and OH^- in water. Of these, the mechanisms that show the closest agreement between the computed value of $\Delta G^{\ddagger}$ (at both the COMSO B3LYP and COSMO MP2 levels) and the experimental value are MC@3 and PA@0. However, as mentioned previously, we do not know *a priori* how accurate the computational methods are. Additionally, the value of $\Delta S^{\ddagger}$ determined from the fit of the TNT disappearance data (Table 5.1) is positive, suggesting that the transition state shows increased disorder compared to TNT. This implies a dissociative mechanism such as proton abstraction.

However, given the overall uncertainty in the results, we cannot conclude which mechanism (MC@1, MC@3, or PA@0) predominates or if the observed kinetics reflect a combination of mechanisms.

In the case of DNAN, the computational and experimental results are not as consistent regarding the reversibility or irreversibility of the reaction. The experimental kinetics suggest an irreversible reaction, for which a ΔG_{rxn} much lower than 0 kcal mol^{-1} (generally less than about -20 kcal mol^{-1}) is expected. However as seen in Figure 5.7, MC@1 and MC@3, which are the top candidate mechanisms based on the analysis given in the previous section, have slightly positive ΔG_{rxn} values. While the reason for this discrepancy is uncertain, possible explanations are either that (*i*) there is another pathway not considered here that has a lower $\Delta G^{\ddagger}$ and is exothermic, or (*ii*) the theory is not accurately describing the transition states of this pathway, perhaps due to the fact that the continuum solvation model is overestimating the first transition state because it is nearly dissociated. While other pathways are possible, MC@1 is a very likely initial reaction, based on the previously observed products of the reaction, 2,4-dinitophenol (*149, 150*) and, subsequently, 2,4-dinitophenolate (*150*). Additionally, molecular modeling of the pathway between DNAN and 2,4-dinitrophenolate at the COSMO B3LYP and COSMO MP2 levels predicts MC@1 to be the initial step of the reaction (details are reported in Appendix B, Figure B.1).

Previous efforts have failed to unambiguously define mechanisms for the reactions of TNT and DNAN with OH^-, especially in the case of TNT where product characterization has been particularly challenging. The experimental and computational observations reported here provide insight into these mechanisms, although some

ambiguity remains, especially in the case of TNT. Because of this ambiguity, it is uncertain whether TNT and DNAN react by the same mechanism. The possible difference in mechanisms means that predicting the reaction mechanism for one based on the other may lead to unreliable predictions of environmental fate. This, along with uncertainties in the consistency of the calculated results with experimental values, presents a challenge for developing QSARs calibrated "fully *in silico*" that predict the hydrolysis behavior of the diverse range of energetic NACs.

5.5. Acknowledgements

This work was supported by the Strategic Environmental Research and Development Program (SERDP) under ER1735. This report has not been subject to review by SERDP and therefore does not necessarily reflect their views and no official endorsement should be inferred. A portion of this research was performed using the PNNL Institutional Computing (PIC) facility and the Chinook and Spokane computing resources at the Molecular Science Computing Facility at EMSL, a national scientific user facility sponsored by the Department of Energy's Office of Biological and Environmental Research located at Pacific Northwest National Laboratory, DE-AC06-76RLO 1830. We also acknowledge EMSL for supporting the development of NWChem. The Pacific Northwest National Laboratory is operated by Battelle Memorial Institute. Structure database management and sorting was performed using Instant JChem (Instant JChem 5.9, 2011, ChemAxon [http://www.chemaxon.com]).

Chapter 6. Free Energy Relationships for Predicting Reduction Rates of Energetic Nitroaromatic Compounds Using Calculated One-Electron Reduction Potentials

Alexandra J. Salter-Blanc, Eric J. Bylaska, Hayley Johnston, and Paul G. Tratnyek[8]

6.1. Abstract

Robust models are needed for predicting the environmental fate of nitroaromatic compounds (NACs), including novel energetic compounds being evaluated for use in future munitions formulations. Here, we explore the ability of a (non-linear) free-energy relationship (FER) based on the Marcus theory of outer-sphere electron transfer to describe rate constants for the reduction of NACs by juglone, lawsone, Fe(II) porphyrin, and by Fe(II) complexed by the organic ligands tiron and desferrioxamine B (DFOB). The results suggest that rate constants reported in the literature for the reduction of predominately non-energetic NACs by Fe(II) porphyrin and Fe(II)/DFOB are consistent with the model. Based on these findings, a FER was calibrated for NAC reduction by Fe(II) porphyrin using one-electron reduction potentials determined from molecular modeling at the B3LYP/6-311++G(2d,2p) level with the COSMO solvation model. Newly measured rate constants for the reduction of 2,4,6-trinitrotoluene (TNT), 2,4-dinitrotoluene (2,4-DNT), and 2,4-dinitroanisole (DNAN) were compared to the FER to assess its usability for predicting reduction rates for energetic NACs. The results suggest that the FER calibration method is generally effective, however, disagreement between

[8] NAC disappearance data were collected by Hayley Johnston under the mentorship of Alexandra J. Salter-Blanc. Molecular modeling was performed by Eric J. Bylaska.

the model and measured results for certain compounds illustrate the challenge associated with calibrating FERs in the absence of experimental descriptor data, especially when applying the FERs to structurally diverse compounds.

6.2. Introduction

The release of energetic nitroaromatic compounds during the manufacture of munitions, and in testing and training activities, poses known and potential threats to human health and the environment (*110, 111*). Concern over this contamination has lead to a growing interest in identifying new energetic compounds with properties that minimize their environmental impact (*153*). This application of "green chemistry" principals (*112*) to the design and selection of new energetic compounds requires data on their chemical fate properties, often in the early stages of evaluation (including prior to synthesis) where experimentation with candidate compounds is impractical (*11, 153*). To overcome this obstacle, robust models are needed to predict key environmental fate properties, including rate constants for nitro reduction—a major determinant of their fate (*154, 155*). In addition, the reliance of these models on experimental input data should be limited, due to the difficulty or impracticality of performing experiments with novel and/or energetic compounds.

Existing models describing the rates of NAC reduction (typically for non-energetic compounds) are based on linear free energy relationships (LFERs). These LFERs include correlations to (*i*) the one-electron reduction potential (E^1_{NAC}) (*30, 31*), (*ii*) E_{LUMO} (*65*), and (*iii*) electron affinity (*62*). These correlations—especially correlations to E^1_{NAC}—have been interpreted as evidence that the rate of NAC reduction is controlled by an outer-sphere electron transfer (Equation 6.1) (*3, 30, 31, 41*).

$$Ar\text{-}NO_{2(aq)} + 1e^-_{(g)} \rightarrow Ar\text{-}NO^{\bullet-}_{2(aq)} \tag{6.1}$$

We hypothesize that, if outer-sphere electron transfer is controlling, the rate constants for NAC reduction can be described using a (non-linear) free energy relationship (FER) based on the theory developed by Marcus (*44*) and elaborated for application to organic reactions by Eberson (*43*).

The Marcus theory of outer-sphere electron transfer relates the free energy of activation ($\Delta G^{\ddagger}$) for an electron transfer to the corrected standard free energy of the reaction ($\Delta G^{\circ\prime}$) and gives rise to the following parabolic relationship:

$$\Delta G^{\ddagger} = W + \frac{\lambda}{4}\left(1 + \frac{\Delta G^{\circ\prime}}{\lambda}\right)^2 \tag{6.2}$$

where W is an electrostatic term and λ is the reorganization energy (*43*). Based on Equation 6.2 and the relationship between reaction rate and $\Delta G^{\ddagger}$ given by the Eyring equation (*4*), $\Delta G^{\circ\prime}$ can be related to the rate constant (k) in the following (non-linear) free-energy relationship (FER) (*43*),

$$k = \frac{k_d}{1 + \frac{k_d}{K_d Z}\exp\left\{\left[W + \frac{\lambda}{4}\left(1 + \frac{\Delta G^{\circ\prime}}{\lambda}\right)^2\right] \Big/ RT\right\}} \tag{6.3}$$

where k_d is the rate at which the electron donor and acceptor diffuse together to form the precursor complex, K_d is the equilibrium constant for formation of the precursor complex, Z is a universal frequency factor (often written as $k_B T/h$), and R and T have their usual meanings. Equation 6.3 accounts for contributions to the rate constant from precursor formation and electron transfer (*43*).

Equation 6.3 can be plotted in the form of a "Marcus plot" (*43*) as shown in Figure 6.1, which shows curves for various λ with relevant values for k_d, K_d, Z, W, R, and

T assigned as discussed in the Results section. This approach has been used to plot and fit data for various organic reactions,(e.g.,(*43, 156*)) including environmentally-relevant oxidation reactions (*157-159*), and photocatalytic reduction of NACs by TiO_2 (*160*). However, it does not appear to have been applied the reduction of NACs by environmentally-relevant model reductants (e.g, quinone and iron porphyrin electron shuttles, and organically-complexed Fe(II) species).

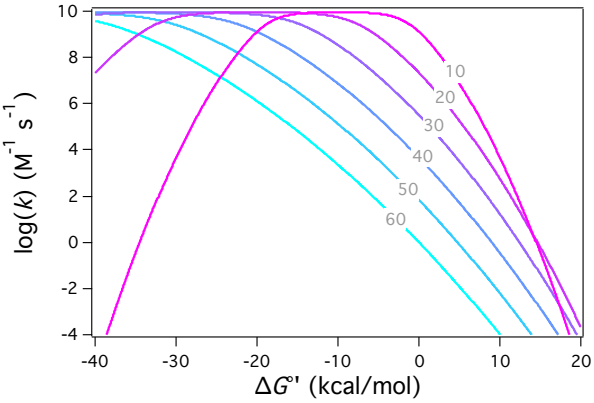

Figure 6.1. Log plots of Equation 3 for various values of λ (labeled on the curves). Values for k_d, K_d, *Z*, *W*, *R*, and *T* relevant to NAC reduction were assigned as discussed in the Results section.

Our first objective in this study was to test the use of the Marcus/Eberson treatment to describe rates of NAC reduction and, in doing so, to revisit the hypothesis that the rate of NAC reduction is controlled by an outer-sphere electron transfer. Our second objective was to define a FER using available literature data for non-energetic NACs and test the usability and accuracy of this type of correlation to predict rate constants for energetic compounds. Our requirements for a useable and accurate FER were that it (*i*) be calibrated with calculated descriptor variables ($\Delta G°'$)—since measured data are often not available for novel energetic NACs—and (*ii*) be validated with data for energetic compounds.

6.3. Experimental

6.3.1. Reagents

Stock solutions of nitrobenzene (NB) (Aldrich Chemical Company Inc.), 2,4,6-trinitrotoluene (TNT) (Chem Service Inc.), 1-chloro-4-nitrobenzene (4-Cl-NB) (Acros Organics), 2,4-dintroanisole (DNAN) (Alfa Aesar), 2,4-dinitrotoluene (2,4-DNT) (Tokyo Chemical Industry Co.), or 1,3-dinitrobenzene (1,3-DNB) (Tokyo Chemical Industry Co.) were prepared in HPLC-grade methanol (Fisher Scientific) at a concentration of 0.1 M. Phosphate buffer was prepared from monobasic sodium phosphate (Fisher Scientific) and adjusted with NaOH (Aldrich) to pH 7.0. L-cysteine (Acros Organics) solutions (0.25 M) were prepared fresh daily in deoxygenated DI water. Stock solutions of Fe(III) meso-tetra (N-methyl-4-pyridyl) porphine pentachloride (Frontier Scientific) was prepared in deoxygenated DI water to achieve a concentration of 4.29 mM. All deionized (DI) water used was obtained from a Milli-Q system (EMD Millipore).

6.3.2. Batch Experiments

Batch experiments were performed in 60mL clear glass reaction vials capped with buytl rubber septa (Fisher Scientific). Each vial was prepared in an anoxic glove box and initially contained 49 mL phosphate buffer, 1 mL aqueous cysteine solution, and an aliquot (25–400μL) of aqueous porphyrin solution. Vials were temperature equilibrated in a 25.0 °C water bath. After temperature equilibration, the specified NAC was introduced to the reaction vial by injecting 50 μL of a 0.1 M stock solution. 1 mL aliquots were removed over time and quenched by mixing with 1 mL of oxygenated HPLC grade methanol in an autosampler vial.

Quenched aliquots were analyzed by high performance liquid chromatography (HPLC). The HPLC set-up included a Varian ProStar 210 solvent delivery module, 410 autosampler, and 330 photodiode array detector, with a Platinum C18 5µ 250-mm x 4.6-mm column (Grace). For most analyses, the mobile phase consisted of 1:1 DI water:HPLC-grade methanol, the flow rate was 1 mL min^{-1}, and the detection wavelength was 254 nm.

6.3.3. Computational Methods

The computational methods used in this study are fully detailed in Appendix C, Section C.1. Briefly, values of E^1_{NAC} were determined from the free energy difference, ΔG_{rxn}, for the one-electron half reaction, given in Equation 6.1. These energy differences were calculated using electronic structure calculations with the COSMO continuum solvation model using the NWChem program suite. The electronic structure calculations were performed using density functional theory (DFT) with the 6-311++G(2d,2p) basis set and the LDA, PBE96, B3LYP, PBE0, and M06-2X exchange correlation functions.

6.4. Results and Discussion

6.4.1. Use of the Marcus/Eberson FER to describe rate constants for NAC reduction

In order to test the ability of the Marcus/Eberson FER to describe rate constants for NAC reduction, we plotted and fit data available in the literature according to Equation 6.3 (Figure 6.2A). For this, we compiled second order rate constants ($\log(k_{red})$) measured with the electron carrier/donor pairs juglone/hydrogen sulfide (*30, 31*), lawsone/hydrogen sulfide (*30*), and Fe(II) porphyrin/cysteine (*30*), as well as Fe(II) complexed by the organic ligands tiron (*161*) and DFOB (*162*).

In order to plot the data, $\Delta G°'$ was determined for all NAC/reductant pairs. First, $\Delta G°$ (the uncorrected standard free energy of the reaction) was calculated from the one-electron reduction potentials (E^1) for the NAC (E^1_{NAC}) and reductant (E^1_{red}) according to Equation 6.4.

$$\Delta G° = -nF\left[E^1_{NAC} - E^1_{red}\right] \tag{6.4}$$

where n is the number of electrons transferred, and F is the Faraday constant. Care was taken to use E^1 values applicable to the experimental conditions (e.g., potentials measured at pH 7 (E^1_7), potentials corrected for standard environmental conditions ($E^{1\prime}$) (*30*), etc.). The E^1_{NAC} data used were those reported in conjunction with the log(k_{red}) data (*30, 31, 161, 162*). E^1_{red} data were obtained from the literature (*30, 163, 164*), or calculated from the standard one-electron reduction potential (E^0) (*162, 165*). Details on the sources of and corrections to E^1 are described in Appendix C, Tables C.1–C.5. Note that in some cases, the reported E^1_{NAC} were not measured, but estimated based on LFERs for juglone and lawsone.[9, 10] We included those data in some plots but excluded them when fitting the data.

Equation 6.3 is written in terms of the $\Delta G°'$ (the corrected standard free energy of the reaction). $\Delta G°'$ is equal to $\Delta G°$ plus a correction to account for electrostatic interactions. This is described in detail elsewhere (*43, 45, 46*). For the reactions described in this work, the electrostatic correction was calculated to be equal to zero in cases where the reductant carries a charge of -1 (*43*), and negligible in all other cases (*45, 46*). Therefore, $\Delta G°'$ was taken to be equal to $\Delta G°$.

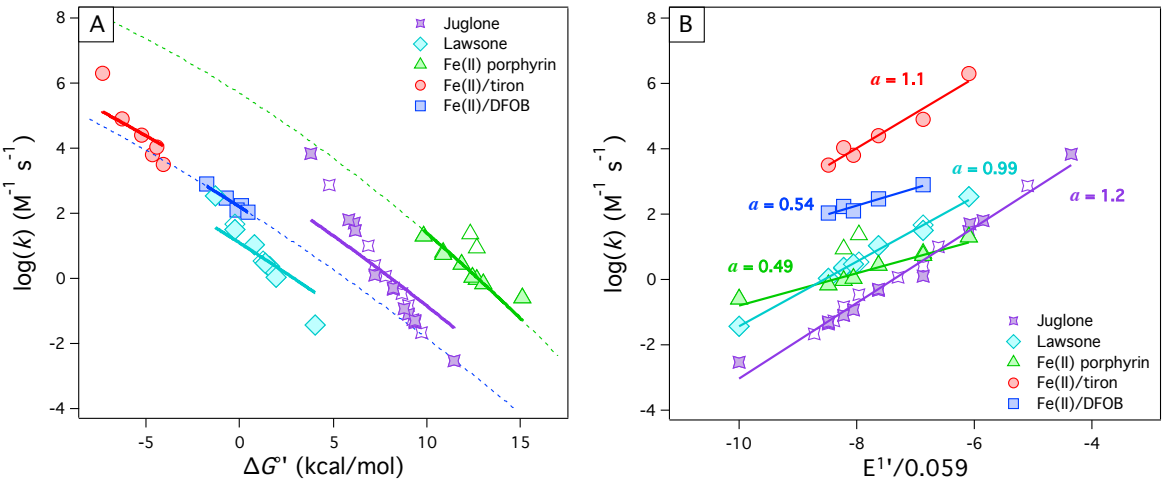

Figure 6.2. log(k_{red}) for various NACs vs. (A) $\Delta G°'$ and (B) E^1_{NAC}/0.059. Reductants include the electron carrier/donor pairs juglone/hydrogen sulfide,(*30, 31*) lawsone/hydrogen sulfide (*30*), Fe(II) porphyrin/cysteine (*30*), and the Fe(II)/ligand complexes Fe(II)/tiron(*161*) and the Fe(II)/DFOB (*162*). Closed symbols represent data for which the independent variable was determined from measured E^1_{red}. Open symbols represent data for which the independent variable was determined from E^1_{red} that were estimated from LFERs (*30, 31*). Only data for which E^1_{red} was measured were included in the fits. Data were fit to (A) Equation 6.5 or (B) an line. In (A), an extrapolation of the fit is shown (as a dashed line) for cases where the data is well fit to Equation 6.5.

The resulting Marcus plot of the data is shown in Figure 6.2A. Also shown are fits using Equation 6.5, which is a log transformation of the Marcus/Eberson FER described in Equation 6.3.

$$\log k_{red} = \log\left(10^{10}\right) - \log\left(1 + 0.1 \times \exp\left\{\left[\frac{\lambda}{4}\left(1 + \frac{\Delta G°}{\lambda}\right)^2\right] \Big/ 0.592\right\}\right) \qquad (6.5)$$

For this analysis, all variables besides the reorganization energy (λ) were defined or calculated as follows. k_d was assumed to be 10^{10} $M^{-1}s^{-1}$ and k_d/K_dZ was given a value of 0.1—both common assumptions for parameters with little influence (*43*). W, which is dependent on the charges on the electron acceptor and donor species (Z_1 and Z_2) in

addition to other system parameters (*43*), is equal to zero when Z_1 and/or $Z_2 = 0$ as is the case in all instances presented here (the charge on the NAC = 0 in all cases).

The data in Figure 6.2A suggest strong correlation of $\log(k_{red})$ to $\Delta G^{\circ\prime}$ with little scatter and few outliers. However, fitting the data to Equation 6.5 shows two outcomes: for two of the reductants—Fe(II) porphyin and Fe(II)/DFOB—the Marcus/Eberson model matches the data closely, but for the other three reductants—juglone, lawsone, and Fe(II)/tiron—the trend in the data is steeper than the model. For Fe(II)/tiron, if the data point for 4-acetylnitrobenzene at $\log(k_{red}) = 6.3$ and $\Delta G^{\circ\prime} = -7.3$ is treated as an outlier, the data show better agreement with the model, but the similarity of the trend for the complete dataset to that for juglone and lawsone suggests it falls into this latter category.

The overall agreement between the model and data for Fe(II)P and Fe(II)/DFOB suggest that these reactions proceed according to Marcus theory (i.e., the reductants behave as outer-sphere, one-electron reductants and the rate is controlled (to varying degrees) by the rates of diffusion and electron transfer as described in Equation 6.3). The deviation between the model and data for juglone, lawsone, and Fe(II)/tiron, however suggests these reactions do not conform to the Marcus model. For example, the reductants may not react with NACs by an outer-sphere electron transfer mechanism or other factors not accounted for in the model may influence $\log(k_{red})$.

For Fe(II)P and Fe(II)/DFOB, the degree to which the rates of diffusion (k_d) and electron transfer influence $\log(k_{red})$ can be diagnosed by considering tangents to the Marcus curve fit (γ). At sufficiently negative values of $\Delta G^{\circ\prime}$, $\gamma = 0$ due to a plateau in the curve (see Figure 6.1) equal to k_d (*43*). In this region, $\log(k_{red})$ is controlled by the rate of precursor formation. For $\gamma < 0$ electron transfer is rate controlling, and $\gamma = -0.5/2.3RT$ at

$\Delta G^{\circ\prime} = 0$ (*45*). If an additional term is added to Equation 6.3 to account for back electron transfer and the formation of successor complexes (as described elsewhere (*45, 166*)), this term will define a limit to γ of -1/2.3RT for sufficiently endergonic reactions (*43, 45, 166*). In this region $\log(k_{red})$ is controlled by the competition between back electron transfer and the rates of successive reactions.

Values of γ can be approximated as the slope of a line fitted to a region of the Marcus curve. Using this method, the values of γ for Fe(II)P and Fe(II)/DFOB were determined to be -0.715/2.3RT and -0.496/2.3RT, respectively, which are consistent with the rate of NAC reduction by these reductants being controlled by the rate of electron transfer. This analysis cannot be applied to juglone, lawsone, and tiron since they do not give NAC reduction kinetics that conform to the Marcus/Eberson model.

These conclusions differ from previously published interpretations based on correlations directly between $\log(k_{red})$ vs E^1_{NAC} (*15, 16, 19*). In these studies, the model applied was Equation 6.6.

$$\log k_{red} = a\frac{E^1_{NAC}}{2.3RT/F} + b = a\frac{E^1_{NAC}}{0.059} + b \tag{6.6}$$

Plots of the data according to the $\log(k_{red})$ vs. $E^1_{NAC}/0.059$ V as defined by Equation 6.6 (originally reported in refs. (*30, 31, 122*)) are shown in Figure 6.2B. A slope (a) of ~1 on this type of plot has been used to support the hypothesis that (single) electron transfer is rate limiting and a slope of <<1 is suggested to be indicative of other rate limiting factors such as precursor formation or mass transport (*3*). Linear fits to the data (including only the cases where E^1_{NAC} was measured rather than estimated) are shown in Figure 6.2B. For juglone, lawsone, and Fe(II)/tiron, $a \approx 1$. For Fe(II)P and Fe(II)/DFOB, $a \approx 0.5$. This analysis leads to the interpretation that the rates of NAC reduction by juglone, lawsone,

and Fe(II)/tiron are limited by the rate of electron transfer, whereas the rates of reduction by Fe(II)P and Fe(II)/DFOB are influenced by other factors.

Equation 6.6 has been described as originating from substitution of the Eyring equation into the Polanyi linear equation (*167, 168*), which relates $\Delta G^{\ddagger}$ and $\Delta G^{\circ\prime}$ (*3, 41*). The Polanyi equation is a linear relationship that predates Marcus's quadratic equation (Equation 6.2). It is valid for a sufficiently small ranges of $\Delta G^{\circ\prime}$ and is essentially a tangent to the curve described by the Marcus equation (Equation 6.2). If the relationship between $\log(k_{red})$ and $\Delta G^{\circ\prime}$ is controlled by the Marcus theory of outer-sphere electron transfer (considering reverse electron transfer), the tangent must be in the range of $0 \geq \gamma \geq -1/2.3RT$ with $\gamma = -0.5/2.3RT$ at $\Delta G^{\circ\prime} = 0$, $\gamma < -0.5/2.3RT$ at $\Delta G^{\circ\prime} > 0$, and $\gamma > -0.5/2.3RT$ at $\Delta G^{\circ\prime} < 0$ (*45*). Therefore, the slope of the data with respect to $\Delta G^{\circ\prime}$ (e.g., as determined from both E^1_{NAC} and E^1_{red}) should be useful in diagnosing whether the data is consistent with Marcus theory. However, in Equation 6.6, E^1_{red} has been factored into the constant *b* (*41*), so the relationship of the data with respect to $\Delta G^{\circ\prime}$ is less clear.

To further illustrate the importance of accounting for E^1_{red}, the data in Figure 6.2B were fit to a version of Equation 6.5 written in terms of E^1_{NAC} (by substituting in Equation 6.4 for $\Delta G^{\circ\prime}$) where both λ and E^1_{red} are floated (not shown). This method of fitting the data accurately captured the "slope" of the trend for juglone, lawsone, and Fe(II)/tiron. However, the fitted values of E^1_{red} were considerably different than the measured values (e.g., for lawsone, the fitted value of E^1_{red} was 0.144 V, whereas the measured values is -0.415 V (*164*)). Based on the various discrepancies associated with analyzing correlations of $\log(k_{red})$ to $E^1_{NAC}/0.059$ V, it appears that treatment of the data

using the full Marcus/Eberson model (Equations 6.5) is a more robust approach for diagnosing outer-sphere electron transfer and assigning rate control.

The conclusion drawn from the Marcus/Eberson analysis that Fe(II)P behaves as an outer sphere electron transfer reductant and juglone does not, is consistent with a pair of previous studies of the reduction of polyhalogenated alkanes (*169, 170*). In these studies rate constants obtained with Fe(II)P and juglone ($k_{Fe(II)P}$ and k_{JUG}) were compared to rate constants obtained with $Co^{(II)}W_{12}O_{40}^{7-}$ (k_{CoW7-}). $CoW_{12}O_{40}^{7-}$ is a polyoxometalate that is well known to react by single electron transfer via an outer-sphere mechanism (*169*). A slope of 1 in the correlation between $\log(k_{Fe(II)P})$ and $\log(k_{CoW7-})$ and slope of >>1 in the correlation of $\log(k_{JUG})$ and $\log(k_{Fe(II)P})$ was interpreted as evidence that Fe(II)P reduces polyhalogenated alkanes in an outer-sphere, single electron transfer, whereas juglone (or mercatojuglone, the reducing species) does not (*169*). This was rationalized as consistent with the hypothesis that mecaptojuglone is responsible for reduction and reduces polyhalogenated alkanes in either an inner-sphere electron transfer, or in a combined reaction involving outer-sphere transfers and X-philic reactions (*170*).

One seemingly conflicting prior study concluded that the reaction between Fe(II)P and NACs occurs by an axial inner-sphere mechanism (*171*). This result was obtained in1:1 *N*-methylpyrrolidone-aceteic acid, however, whereas all other results considered here were obtained in aqueous solutions. Generally, metalloporphyrins are known to participate in both outer- and inner-sphere reactions (*172*). and, in cases where the reaction is outer-sphere, analysis based on the Marcus theory for electron transfer is common and has been reviewed previously (*172*).

Based on the agreement of the Fe(II)P data with the Marcus/Eberson model—as well as the simplicity of performing and analyzing Fe(II)P experiments—we chose it as a model reductant for formulating a FER using calculated E^1_{NAC} values and for testing the applicability of the FER to energetic NACs.

6.4.2. Calculation of E^1_{NAC} and Use in FER Calibration

Use of the Marcus/Eberson model requires data for E^1_{NAC} in order to calculate $\Delta G°'$. Measured data for E^1_{NAC} are often lacking or difficult to obtain, especially for novel energetic NACs (e.g., due to lack of synthesized material or experimental hazards). To overcome this, it is desirable to use calculated descriptor values, which in this case were obtained using molecular modeling. While direct calculation of $\Delta G°$ is impractical at this time due to the computational expensive, calculated values of E^1_{NAC} can be combined with a measured E^1_{red} to determine $\Delta G°'$. Multiple efforts have been made to determine E^1_{NAC} using various computational techniques (*59-62*), We have compiled and compared the results of these studies previously (*60*). Here we extend that work by presenting the results of a new method for calculating E^1_{NAC} using DFT combined with the COSMO solvation model.

In order to determine which computational method gives results that are most consistent with experimental data, a subset of the calculated E^1_{NAC} values was compared to a previously compiled set of measured E^1_{NAC} (*63*). The measured dataset is shown in Table 6.1 along with the corresponding computed values determined at the levels of theory used in this study. Deviations between the calculated and measured datasets were analyzed by calculating the mean absolute deviation (MAD), root mean square deviation (RMSD), and the largest positive and negative deviation between the datasets.

Table 6.1. Calculated one-electron reduction potentials (E^1_{NAC}) and comparison to a set of measured values. Calculated values were determined with density functional theory (DFT) using the the 6-311++G(2d,2p) basis set with the specified exchange correlation functionals. Solvation was accounted for using the COSMO model.

Abbr. [a]	Measured E^1_{NAC} (V) [b]	Calculated E^1_{NAC} (V)						
		LDA	**PBE**	**B3LYP**	**PBE0**	**M06-2X**	**B3LYP***	**M06-2X***
NB	-0.486	-0.512	-0.640	-0.479	-0.578	-0.476	-0.435	-0.432
2-CH_3-NB	-0.590	-0.659	-0.771	-0.616	-0.695	-0.630	-0.506	-0.526
3-CH_3-NB	-0.475	-0.561	-0.690	-0.522	-0.602	-0.490	-0.457	-0.441
4-CH_3-NB	-0.500	-0.594	-0.726	-0.569	-0.637	-0.552	-0.481	-0.479
3-Cl-NB	-0.405	-0.272	-0.812	-0.400	-0.487	-0.571	-0.394	-0.490
4-Cl-NB	-0.450	-0.475	-0.599	-0.444	-0.539	-0.440	-0.417	-0.410
4-NH_2-NB	-0.568	-0.964	-1.043	-0.753	-0.863	-0.737	-0.576	-0.591
3-$COCH_3$-NB	-0.437	-0.439	-0.586	-0.469	-0.538	-0.460	-0.430	-0.422
4-$COCH_3$-NB	-0.356	-0.174	-0.354	-0.304	-0.375	-0.352	-0.345	-0.357
1,2-DNB	-0.287	0.033	-0.160	-0.121	-0.238	-0.344	-0.251	-0.346
1,3-DNB	-0.345	-0.421	-0.581	-0.390	-0.505	-0.384	-0.389	-0.376
1,4-DNB	-0.257	0.197	0.011	0.059	-0.075	-0.117	-0.158	-0.214
2,4-DNT	-0.397	-0.542	-0.638	-0.486	-0.618	-0.404	-0.439	-0.388
2,6-DNT	-0.402	-0.318	-0.718	-0.569	-0.682	-0.525	-0.481	-0.462
TNT	-0.253	-0.232	-0.384	-0.223	-0.325	-0.252	-0.303	-0.296
2-CHO	-0.355	-0.151	-0.345	-0.271	-0.361	-0.341	-0.328	-0.350
4-CHO	-0.322	-0.065	-0.255	-0.216	-0.273	0.003	-0.299	-0.141
4-CH_2OH	-0.478	-0.554	-0.642	-0.501	-0.624	-0.561	-0.447	-0.484
2-ADNT	-0.417	-0.586	-0.729	-0.554	-0.642	-0.466	-0.474	-0.426
4-ADNT	-0.449	-0.707	-0.753	-0.629	-0.700	-0.571	-0.512	-0.490
2,4-DANT	-0.502	-0.870	-0.995	-0.810	-0.876	-0.775	-0.606	-0.614
MAD [c]		*0.164*	*0.220*	*0.099*	*0.146*	*0.082*	*0.043*	*0.045*
RMSD [d]		*0.044*	*0.065*	*0.018*	*0.030*	*0.015*	*0.003*	*0.004*
Largest Positive Deviation		*0.454* [e]	*0.268* [e]	*0.316* [e]	*0.182* [e]	*0.325* [f]	*0.099* [e]	*0.181* [f]
Largest Negative Deviation		*-0.396* [g]	*-0.493* [h]	*-0.308* [h]	*-0.374* [h]	*-0.273* [h]	*-0.104* [h]	*-0.112* [h]

a) Abbreviations defined in the List of Abbreviations (page xiii). *b*) Dataset previously compiled by Phillips et al. (*63*). *c*) Mean absolute deviation. *d*) Root mean square deviation. *e*) Deviant value for 1,4-DNB. *f*) Deviant value for 4-CHO. *g*) Deviant value for 4-NH_2-NB. *h*) Deviant value for 2,4-DANT.

The lowest MAD and RMSD correspond with the M06-2X and B3LYP datasets, respectively (Table 6.1). Linear fits of these datasets plotted against the measured dataset (shown in Appendix C, Figure C.1 and Figure C.2) showed slopes steeper than 1. To account for this deviation, a linear transformation was applied to the computed data based on the fit. The corrected datasets are given in Table 1.1 as B3LYP* and M06-2X*. The MAD and RMSD for these B3LYP* and M06-2X* are very similar, but the values for B3LYP* are slightly smaller. The magnitude of the largest negative deviation is similar between the datasets, but B3LYP* produces a smaller largest positive deviation. Based on this analysis, it was conclude that the B3LYP* dataset is the most consistant with the experimental results.

In order to test the reliability of the calculated E^{1}_{NAC} for calibrating FERs, values calculated using the B3LYP* method were used to determine $\Delta G^{\circ\prime}$, which were then used to replot the Fe(II)P correlation shown in Figure 6.2A. The resulting Marcus plot is shown in Figure 6.3 along with a fit to Equation 6.5. The data show minimal scatter, suggesting that use of the calculated E^{1}_{NAC} in place of measured values is adequate. The calibrated FER is given in Equation 6.7.

$$\log k_{\mathrm{red}} = 10 - \log\left(1 + 0.1 \times \exp\left\{\left[\frac{30.31}{4}\left(1 + \frac{\Delta G^{\circ\prime}}{30.31}\right)^{2}\right] \Big/ 0.592\right\}\right) \tag{6.7}$$

From this analysis, the fitted value of λ is 30.31 ± 0.60, which is similar to the value of 28.96 ± 0.79 for the plot of the data to $\Delta G^{\circ\prime}$ determined from measured values of E^{1}_{NAC} (shown in Figure 6.2A). This further supports the ability of the calculated values to approximate the measured results. Equation 6.7 can be written in terms of E^{1}_{NAC} (through substitution of Equation 6.4 for $\Delta G^{\circ\prime}$ and 0.065 V for E^{1}_{red} (*30*)) and simplified to obtain

Equation 6.8. This FER can potentially be used to predict log(k_{red}) directly from values of E^1_{NAC} calculated using the method described for the B3LYP* dataset.

$$\log k_{red} = 10 - \log\left(1 + 0.1 \times \exp\left\{12.80\left(1 - 0.7608\left[E^1_{NAC} - 0.065\ \text{V}\right]\right)^2\right\}\right) \quad (6.8)$$

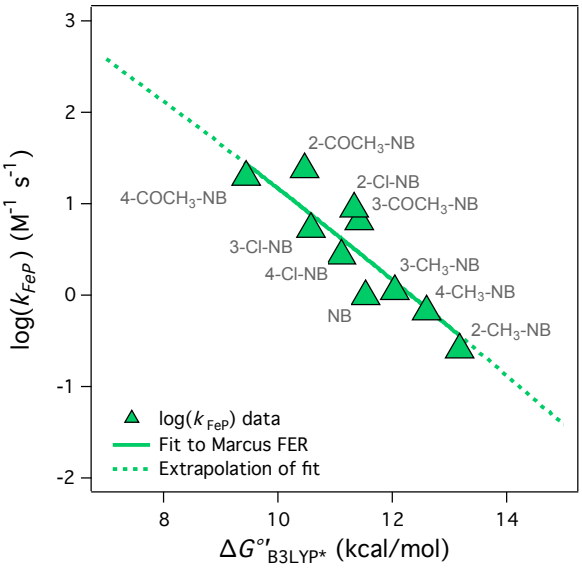

Figure 6.3. Marcus plot of log(k_{red}) for NAC reduction by Fe(II)P (obtained from the literature (*30*)) with $\Delta G°'$ determined from E^1_{NAC} calculated at the B3LYP/6-311++G(2d,2p) level with an applied linear transformation based on correlation to a measured dataset (B3LYP* in Table 6.1). A fit of the data to Equation 6.5 is shown along with the extrapolated FER.

6.4.3. Validation of the FER for Energetic NACs

In order to test applicability of the FER given in Equations 6.7and 6.8 for predicting rate constants for energetic compounds, we measured rate constants for reduction of three energetic NACs—2,4-DNT, TNT and DNAN—by Fe(II)P/cysteine. Rate constants were also measured for three non-energetic NACs, NB, 4-Cl-NB, and 1,3-DNB in order to check the agreement between our results and the data used to calibrate the FER shown in Equation 6.5.

A typical analysis of the measured data is shown in Figure 6.4 for 2,4-DNT. Data for the other compounds can be found in Appendix C, Table C.7. Concentration vs. time data for NAC disappearance at different Fe(II)P concentrations was fit to pseudo-first order kinetics (*30, 31*) to obtain observed rate constants (k_{obs}). These k_{obs} were plotted against [Fe(II)P] and fit to a line to obtain the second-order rate constant $k_{Fe(II)P}$. Data for NB, 4-Cl-NB, and 2,4-DNT were fit in this manner. In some cases (1,3-DNB, TNT, and DNAN) the concentration vs. time plots showed rate increases that are not captured by the first-order model. This effect was especially pronounced for DNAN (Figure 6.5), but was also evident in concentration vs. time plots for 1,3-DNB and TNT (Appendix C, Table C.7). The deviation from first-order kinetics is likely the result of secondary reactions, but this was not investigated further.

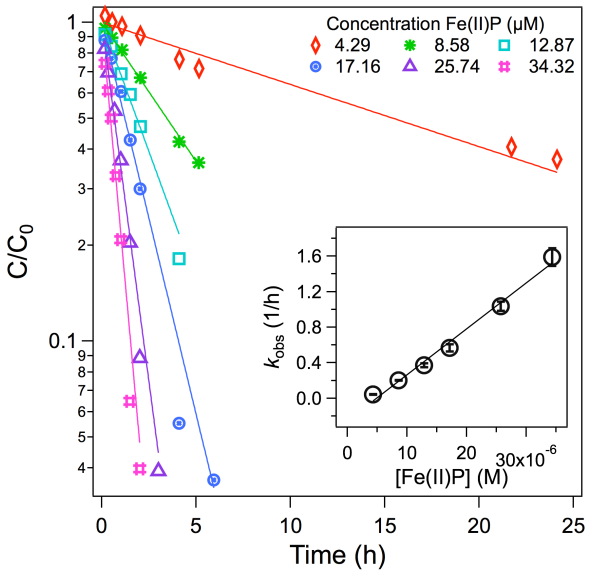

Figure 6.4. Concentration vs. time plots of 2,4-DNT disappearance at various [Fe(II)P] with pseudo-first-order fits. Inset: k_{obs} from the pseudo-first order fits vs. nominal [Fe(II)P] with linear fit.

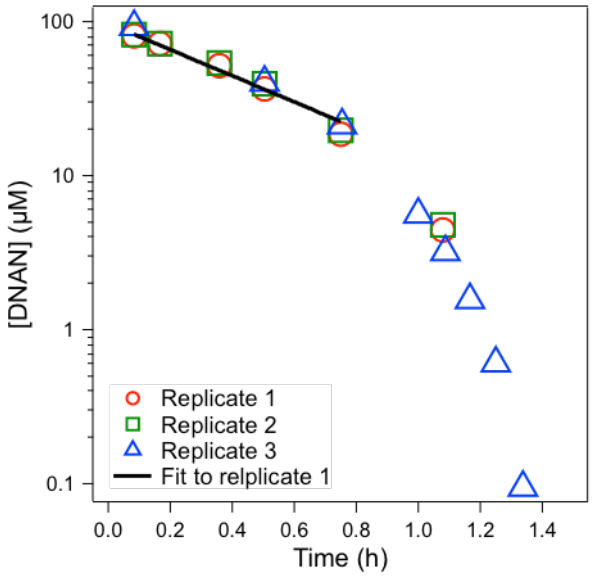

Figure 6.5. DNAN disappearance at 34.32 µM FeP with an initial portion of the data fit to a pseudo-first-order model.

In the absence of a comprehensive kinetic model for the cases that show deviation from first-order behavior, the initial portion of the data alone were fit to a first-order model (similar to the method of initial rates (*7*)). This treatment resulted in fitting approximately one to three half-lives of NAC disappearance data. It is likely that the kinetics at the beginning of the experiment were dominated by simple reduction of the NACs (i.e., according to Equation 6.1), making this simplification a satisfactory approximation of the rate constant for that process. Details regarding data fitting for all the NACs evaluated are given in Appendix C, Table C.7. The resulting $\log(k_{Fe(II)P})$ values are reported in Table 6.2.

Table 6.2. FER verification and validation data. k_{FeP} were determined from data presented in Appendix C, Table C.7.

NAC	$E^{1}_{NAC,B3LYP*}$	$\Delta G^{\circ\prime}_{B3LYP*}$	$k_{Fe(II)P}$ (L M^{-1} s^{-1})	log(k_{FeP})
NB	-0.435	11.5	1.06 ± 0.16	0.026
4-Cl-NB	-0.417	11.1	1.946 ± 0.083	0.289
1,3-DNB	-0.389	10.5	16.6 ± 0.77	1.22
2,4-DNT	-0.439	11.6	14.34 ± 0.76	1.156
TNT	-0.303	8.49	112.1 ± 3.1	2.050
DNAN	-0.513	13.3	17.50 ± 0.55	1.243

log($k_{Fe(II)P}$) values for the non-energetic compounds (NB, 4-Cl-NB, and 1,3-DNB) were used to check the agreement between our results and the data used to calibrate the FER. These data were appended to a plot of the calibration data from Figure 6.3 (shown in Figure 6.6) by plotting the data vs. the associated $\Delta G^{\circ\prime}$ value determined from E^{1}_{NAC} calculated using the B3LYP* method ($\Delta G^{\circ\prime}_{B3LYP*}$). The data agree well with the FER, thereby supporting the agreement of our experimental data with the calibration data. Following method verification, log($k_{Fe(II)P}$) data for the energetic compounds tested—2,4-DNT, TNT, and DNAN—were appended to Figure 6.6 to test the validity of the FER to energetic compounds. The data point for TNT plots in line with the extrapolated FER, suggesting that the FER accurately predicts log($k_{Fe(II)P}$) for TNT. The data point for 2,4-DNT falls slightly outside the range of scatter, but is still within one log value. The data point for DNAN is an obvious outlier.

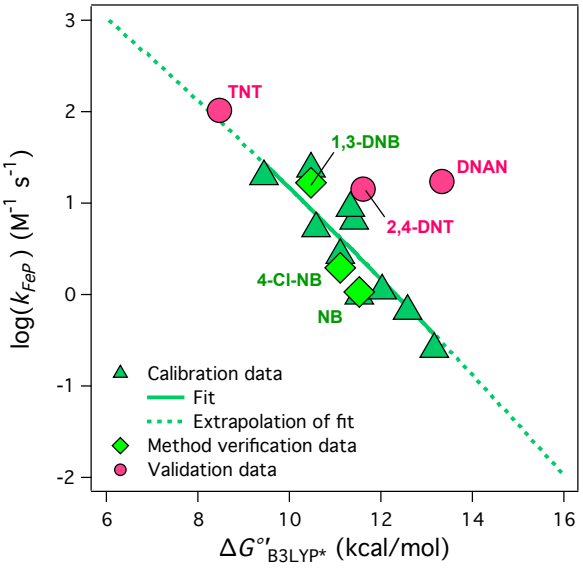

Figure 6.6. Comparison of newly collected log($k_{Fe(II)P}$) data to the calibration dataset and FER. Data for non-energetic NACs were used to verify agreement of the new data with the calibration data (method verification data). Data for energetic NACs were used to test the validity of the FER to energetic compounds (validation data).

Potential reasons for DNAN appearing as an outlier in Figure 6.6 include (*i*) error in log($k_{Fe(II)P}$), (*ii*) error in $\Delta G^{\circ\prime}_{B3LYP*}$, or (*iii*) a fundamental difference in the reduction mechanism. It seems unlikely that error in log(k_{FeP}) alone is responsible for the observed deviation, since the measured log($k_{Fe(II)P}$) for DNAN is close to two orders-of-magnitude larger than the FER prediction. A more likely explanation is inaccuracy in the calculated value $E^1_{NAC,B3LYP*}$, which was used to determine $\Delta G^{\circ\prime}_{B3LYP*}$. The largest negative deviation reported for $E^1_{NAC,B3LYP*}$ in Table 6.1 is -0.104 V (for 2,4-DANT). If this deviation is propagated through to the calculation of $\Delta G^{\circ\prime}$, it results in a positive bias of about 4 kcal mol^{-1}. This is similar to the degree of disagreement between the data point for DNAN and the FER on the $\Delta G^{\circ\prime}$ axis, suggesting that error in the calculation of $E^1_{NAC,B3LYP*}$ may explain the observed deviation. However, it cannot be ruled out that the disagreement is related to a difference in the mechanism of DNAN reduction, potentially

related to the presence of the methoxy group, which is not represented in the other NACs considered.

These results illustrate the challenges associated with applying FERs to a structurally diverse set of compounds. It is expected that the challenges will be even greater when attempting to apply this FER to more complex energetic NACs, including those with multiple ring structures such as CL-20. To fully resolve this issue, more reduction rate data for these energetic compounds will be required. For the present, it is suggested that the FER proposed here—as well as correlations to E^1_{NAC} that have been published elsewhere—be applied primarily as a screening tool to direct and inform experimental determination of NAC reduction rates.

Acknowledgements

This work was supported by the Strategic Environmental Research and Development Program (SERDP) under ER1735. This report has not been subject to review by SERDP and therefore does not necessarily reflect their views and no official endorsement should be inferred. Alexandra J. Salter-Blanc was supported as an OHSU Graduate Research Scholar during a portion of this study. A portion of this research was performed using the PNNL Institutional Computing (PIC) facility and the Chinook, Spokane, Barracuda, and Cascade computing resources at the Molecular Science Computing Facility at EMSL, a national scientific user facility sponsored by the Department of Energy's Office of Biological and Environmental Research located at Pacific Northwest National Laboratory, DE-AC06-76RLO 1830. We also acknowledge EMSL for supporting the development of NWChem. The Pacific Northwest National

Laboratory is operated by Battelle Memorial Institute. Structure database management and sorting was performed using Instant JChem (Instant JChem 5.9.4, 2012, ChemAxon [http://www.chemaxon.com]).

Chapter 7. Summary and Conclusions

7.1. Part I. Remediation of 1,2,3-Trichloropropane with Zerovalent Zinc

Part I of this dissertation details the evaluation of ZVZ for treatment of TCP-contaminated groundwater. The included chapters build off of prior results, which suggest that the kinetics of TCP reduction by ZVZ are fast enough for ZVZ to be a viable reductant in engineered treatment systems while ZVI is not (*38*). These results concerning ZVZ, however, were determined under controlled laboratory conditions (batch experiments containing reagent-grade ZVZ in DI water), so the efficacy of ZVZ for treatment of TCP in the field was at that point not yet well defined. In Chapters 2-4, the viability of ZVZ for remediating TCP contamination is examined under conditions that increasingly mimic those of potential engineered treatment systems, including *ex situ* wellhead treatment and *in situ* permeable reactive barriers.

In Chapter 2, the effects of solution chemistry—specifically pH and groundwater chemistry—on the kinetics of TCP reduction by ZVZ are examined. The results suggest that the kinetics of TCP reduction are controlled by solubility-related changes to a ZnO shell on the surface of the ZVZ and the morphology of that film. Alkaline groundwater is seen to inhibit the reduction of TCP through promotion of a passivating "Type II" ZnO film. This inhibition is not observed in acidic groundwater, however, the results suggest treatment systems will operate in the alkaline range. Even with the effects of groundwater taken into account, the results suggest ZVZ will produce TCP reduction kinetics similar to, or faster than ZVI.

Chapter 3 summarizes work performed concurrently to that presented in Chapter 2, but with an increased focus on gathering results to inform a pilot-scale assessment of ZVZ for treating TCP contamination. The kinetics of TCP reduction by less expensive, commercially available, industrial-grade ZVZ were measured in batch reactor experiments and compared to results gathered with reagent-grade ZVZ. Two materials were found to produce kinetics similar to those measured with reagent-grade materials and were not affected by the presence of oxygen. These ZVZ materials were further tested in bench-scale column experiments containing ZVZ or ZVZ mixed with sand. Rate constants for TCP reduction in the columns were measured and compared to the batch reactor results using scaling calculations proposed in the chapter. The potential of promoting faster TCP reduction by decreasing the pH of the column influent (based on the results presented in Chapter 2) was also tested. The results, however, suggest that such pH perturbations are unlikely to have a significant effect in large-scale treatment scenarios.

Chapter 4 details the design, execution, and analysis of a field-scale pilot test of two industrial-grade ZVZ materials for treatment of groundwater at a TCP-contaminated site in Southern California. Results from Chapter 3, including TCP reduction kinetics measured in bench-scale column experiments and the scaling calculations proposed, were used to design two phases of large-scale column experiments that were run for 8-12 weeks. The kinetics of TCP degradation in these columns over the course of operation were evaluated and justified based on characterization of the column materials post-operation. The kinetics were found to be comparable to those measured in bench-scale

batch reactor and column experiments. Overall, the results suggest that ZVZ shows promise for field-scale treatment of TCP contaminated groundwater.

7.2. Part II. Prediction of the Environmental Fate of Novel Munitions Compounds

While Part I of this dissertation focuses on the study of chemical kinetics in relation to remediation of existing contamination, Part II focuses on preventing or limiting future contamination by designing and using chemicals with favorable environmental fate properties. Specifically, the chapters were motivated by the goal of developing models in the form of QSARs or LFERs to predict degradation rates of chemicals used in existing and future munitions formulations. Progress toward this goal is made for two environmental degradation pathways relevant to groundwater—hydrolysis and reduction—with emphasis on NACs, an important family of compounds used in munitions.

Chapter 5 addresses uncertainties regarding the mechanism of NAC degradation by alkaline hydrolysis that hinder the development of models to predict the kinetics of this process. The focus of the chapter is on TNT, which has been heavily used in munitions in the past, and DNAN, which is replacing TNT in some modern munitions formulations. Potential mechanisms of alkaline hydrolysis are proposed for each compound based on a review of the relevant literature. Alkaline hydrolysis kinetics for TNT and DNAN are reported. Information gathered from the kinetic experiments is also combined with results form molecular modeling to evaluate the probability of the candidate mechanisms. The results suggest that the initial step in the alkaline hydrolysis of TNT is either Meisenheimer complex formation at the 1 or 3 position (as defined in Figure 5.3) or proton abstraction from the methyl group. For DNAN the likely initial step

is suggested to be Meisenheimer complex formation at the 1 position (as defined in Figure 5.3). The results lead to a better understanding of the mechanisms and kinetics of TNT and DNAN hydrolysis, however, potential mechanistic differences between the compounds suggest it is not reliable to extrapolate results from these experiments to other compounds using a predictive model.

Chapter 6 details the development of a model to predict rates for NAC degradation by reduction. First, reduction rate constant data (log(k)) for NAC reduction by juglone, lawsone, iron porphyrin, tiron, and DFOB are analyzed for agreement with a Marcus theory based model. The results lead to mechanistic conclusions regarding the rate limiting steps in these reactions. A FER is then developed relating log(k) for NAC reduction by iron porphyrin to $\Delta G^{\circ\prime}$ for the reaction. $\Delta G^{\circ\prime}$ for FER calibration is calculated using values of E^1 for the NACs determined using molecular modeling. The FER is then validated with newly gathered log(k) data for energetic and non-energetic NACs. The results suggest that the FER calibration method is generally effective, but also illustrate the challenges associated with calibrating FERs in the absence of calculated descriptor data.

References

(1) Capellos, C.; Bielski, B. H. J. *Kinetic Systems: Mathematical Descriptions of Chemical Kinetics in Solution*; Wiley: New York, **1972**.

(2) McQuarrie, D. A.; Simon, J. D. *Physical Chemistry: A Molecular Approach*; University Science Books: Sausalito, **1997**.

(3) Schwarzenbach, R. P.; Gschwend, P. M.; Imboden, D. M. *Environmental Organic Chemistry;* 2nd ed.; Wiley: Hoboken, NJ, **2003**.

(4) Maskill, H. *The Physical Basis of Organic Chemistry*; Oxford University: Oxford, **1989**.

(5) Benson, S. W. *The Foundations of Chemical Kinetics*; McGraw-Hill: New York, **1960**.

(6) Stone, A. T.; Morgan, J. J. Kinetics of chemical transformation in the environment. In: *Aquatic Chemical Kinetics*; Wiley: New York, **1990**; pp. 1-41.

(7) Brezonik, P. L. *Chemical Kinetics and Process Dynamics in Aquatic Systems*; Lewis: Boca Raton, **1994**.

(8) Matheson, L. J.; Tratnyek, P. G. Reductive dehalogenation of chlorinated methanes by iron metal. *Environ. Sci. Technol.* **1994**, *28*, 2045-2053.

(9) Arnold, W. A.; Roberts, A. L. Pathways of chlorinated ethylene and chlorinated acetylene reaction with Zn(0). *Environ. Sci. Technol.* **1998**, *32*, 3017-3025.

(10) Arnold, W. A.; Roberts, A. L. Pathways and kinetics of chlorinated ethylene and chlorinated acetylene reaction with Fe(0) particles. *Environ. Sci. Technol.* **2000**, *34*, 1794-1805.

(11) Salter-Blanc, A. J.; Bylaska, E. J.; Ritchie, J. J.; Tratnyek , P. G. Mechanisms and kinetics of alkaline hydrolysis of the energetic nitroaromatic compounds 2,4,6-trinitrotoluene (TNT) and 2,4-Dinitroanisole (DNAN). *Environ. Sci. Technol.* **2013**, *47*, 6790-6798.

(12) Ramachandran, B. R.; Halpern, A. M. A novel experiment in chemical kinetics: The A $\rightleftharpoons$ B $\rightarrow$ C reaction system. *J. Chem. Educ.* **1997**, *74*, 975-978.

(13) Mills, A.; Seth, A.; Peters, G. Alkaline hydrolysis of trinitrotoluene, TNT. *Phys. Chem. Chem. Phys.* **2003**, *5*, 3921-3927.

(14) Emmrich, M. Kinetics of the Alkaline Hydrolysis of 2,4,6-Trinitrotoluene in Aqueous Solution and Highly Contaminated Soils. *Environ. Sci. Technol.* **1999**, *33*, 3802.

(15) Harris, J. C. Rate of Hydrolysis. In: *Handbook of Chemical Property Estimation Methods*; McGraw-Hill: New York, **1982**; pp. 7.1-7.48.

(16) Church, C. D.; Pankow, J. F.; Tratnyek, P. G. Hydrolysis of tert-butyl formate: Kinetics, products, and implications for the environmental impact of MTBE. *Environ. Toxicol. Chem.* **1999**, *18*, 2789-2796.

(17) Scherer, M. M.; Balko, B. A.; Tratnyek, P. G. The role of oxides in reduction reactions at the metal-water interface. In: *Mineral-Water Interfacial Reactions: Kinetics and Mechanisms*; Sparks, D. L.; Grundl, T. J., Eds.; American Chemical Society: Washington, DC, **1998**; ACS Symposium Series, *Vol. 715*; pp. 301-322.

(18) Salter-Blanc, A. J.; Tratnyek, P. G. Effects of solution chemistry on the dechlorination of 1,2,3-trichloropropane by zero-valent zinc. *Environ. Sci. Technol.* **2011**, *45*, 4073-4079.

(19) Schlicker, O.; Ebert, M.; Fruth, M.; Weidner, M.; Wüst, W. F.; Dahmke, A. Degradation of TCE with iron: the role of competing chromate and nitrate reduction. *Ground Water* **2000**, *38*, 403-409.

(20) Liu, Y.; Phenrat, T.; Lowry, G. V. Effect of TCE concentration and dissolved groundwater solutes on NZVI-promoted TCE dechlorination and H_2 evolution. *Environ. Sci. Technol.* **2007**, *41*, 7881-7887.

(21) Klausen, J.; Vikesland, P. J.; Kohn, T.; Burris, D. R.; Ball, W. P.; Roberts, A. L. Longevity of granular iron in groundwater treatment processes: solution composition effects on reduction of organohalides and nitroaromatic compounds. *Environ. Sci. Technol.* **2003**, *37*, 1208-1218.

(22) Kohn, T.; Kane, S. R.; Fairbrother, D. H.; Roberts, A. L. Investigation of the inhibitory effect of silica on the degradation of 1,1,-trichloroethane by granular iron. *Environ. Sci. Technol.* **2003**, *37*, 5806-5812.

(23) Kohn, T.; Roberts, A. L. The effect of silica on the degradation of organohalides in granular iron columns. *J. Contam. Hydrol.* **2006**, *83*, 70-88.

(24) Agrawal, A.; Ferguson, W., J.; Gardner, B., O.; Christ, J., A.; Bandstra, J. Z.; Tratnyek, P. G. Effects of carbonate species on the kinetics of dechlorination of 1,1,1-trichloroethane by zero-valent iron. *Environ. Sci. Technol.* **2002**, *36*, 4326-4333.

(25) Devlin, J. F.; Allin, K. O. Major anion effects on the kinetics and reactivity of granular iron in glass-encased magnet batch reactor experiments. *Environ. Sci. Technol.* **2005**, *39*, 1868-1874.

(26) Kim, J. S.; Shea, P. J.; Yang, J. E.; Kim, J.-E. Halide salts accelerate degradation of high explosives by zerovalent iron. *Environmental Pollution (Amsterdam, Netherlands)* **2007**, *147*, 634-641.

(27) Sposito, G. Electron shuttling by natural organic matter: Twenty years after. In: *Aquatic Redox Chemistry*; Tratnyek, P. G.; Grundl, T. J.; Haderlein, S. B., Eds.; American Chemical Society: Washington, DC, **2011**; ACS Symposium Series, *Vol. 1071*; pp. 113-127.

(28) Uchimiya, M.; Stone, A. T. Reversible redox chemistry of quinones: Impact on biogeochemical cycles. *Chemosphere* **2009**, *77*, 451-458.

(29) Tratnyek, P. G.; Macalady, D. L. Oxidation-reduction reactions in the aquatic environment. In: *Handbook of Property Estimation Methods for Chemicals: Environmental and Health Sciences*; Mackay, D.; Boethling, R. S., Eds.; Lewis: Boca Raton, FL, **2000**; pp. 383-415.

(30) Schwarzenbach, R. P.; Stierli, R.; Lanz, K.; Zeyer, J. Quinone and iron porphyrin mediated reduction of nitroaromatic compounds in homogeneous aqueous solution. *Environ. Sci. Technol.* **1990**, *24*, 1566-1574.

(31) Hofstetter, T. B.; Heijman, C. G.; Haderlein, S. B.; Holliger, C.; Schwarzenbach, R. P. Complete reduction of TNT and other (poly)nitroaromatic compounds under iron-reducing subsurface conditions. *Environ. Sci. Technol.* **1999**, *33*, 1479-1487.

(32) Hartenbach, A.; Hofstetter, T. B.; Berg, M.; Bolotin, J.; Schwarzenbach, R. P. Using nitrogen isotope fractionation to assess abiotic reduction of nitroaromatic compounds. *Environ. Sci. Technol.* **2006**, *40*, 7710-7716.

(33) Hartenbach, A. E.; Hofstetter, T. B.; Aeschbacher, M.; Sander, M.; Kim, D.; Strathmann, T. J.; Arnold, W. A.; Cramer, C. J.; Schwarzenbach, R. P. Variability of nitrogen isotope fractionation during the reduction of nitroaromatic compounds with dissolved reductants. *Environ. Sci. Technol.* **2008**, *42*, 8352-8359.

(34) Tratnyek, P. G.; Scherer, M. M.; Johnson, T. J.; Matheson, L. J. Permeable reactive barriers of iron and other zero-valent metals. In: *Chemical Degradation Methods for Wastes and Pollutants: Environmental and Industrial Applications*; Tarr, M. A., Ed.; Marcel Dekker: New York, **2003**; pp. 371-421.

(35) Vikesland, P. J.; Klausen, J.; Zimmermann, H.; Roberts, A. L.; Ball, W. P. Longevity of granular iron in groundwater treatment processes: Changes in solute transport properties over time. *J. Contam. Hydrol.* **2003**, *64*, 3-33.

(36) Johnson, T. L.; Scherer, M. M.; Tratnyek, P. G. Kinetics of halogenated organic compound degradation by iron metal. *Environ. Sci. Technol.* **1996**, *30*, 2634-2640.

(37) Tratnyek, P., G.; Sarathy, V.; Kim, J.-H.; Chang, Y.-S.; Bae, B., Effects of particle size on the kinetics of degradation of contaminants. In: *International Environmental Nanotechnology Conference: Applications and Implications (7-9 October 2008),* Chicago, IL, U.S. Environmental Protection Agency, **2009**, *Vol. EPA 905-R09-032*, pp. 67-72.

(38) Sarathy, V.; Tratnyek, P. G.; Salter, A. J.; Nurmi, J. T.; Johnson, R. L.; O'Brien Johnson, G. Degradation of 1,2,3-trichloropropane (TCP): Hydrolysis, elimination, and reduction by iron and zinc. *Environ. Sci. Technol.* **2010**, *44*, 787-793.

(39) Salter-Blanc, A. J.; Bylaska Eric, J.; Johnston, H.; Tratnyek , P. G. Free energy relationships for predicting reduction rates of energetic nitroaromatic compounds using calculated one-electron reduction potentials. *Environ. Sci. Technol.* **2014**, in prep.

(40) Donaldson, W. T. The role of property-reactivity relationships in meeting the EPA's needs for environmental rate constants. *Environ. Toxicol. Chem.* **1992**, *11*, 887-891.

(41) Tratnyek, P. G.; Weber, E. J.; Schwarzenbach, R. P. Quantitative structure-activity relationships for chemical reductions of organic contaminants. *Environ. Toxicol. Chem.* **2003**, *22*, 1733-1742.

(42) Atkins, P. W. *Physical Chemistry;* 4th Edition ed.; W. H. Freeman and Company: New York, **1990**.

(43) Eberson, L. *Electron Transfer Reactions in Organic Chemistry*; Springer-Verlag: Berlin, **1987**.

(44) Marcus, R. A. Chemical and electrochemical electron-transfer theory. *Ann. Rev. Phys. Chem.* **1964**, *15*, 155-196.

(45) Scandola, F.; Balzani, V.; Schuster, G. B. Free-energy relationships for reversible and irreversible electron-transfer processes. *J. Am. Chem. Soc.* **1981**, *103*, 2519-2523.

(46) Lund, T.; Lund, H. Single electron transfer as rate-determining step in an aliphatic nucleophilic substitution. *Acta Chem. Scand.* **1986**, *40B*, 470-485.

(47) Cwiertny, D. M.; Arnold, W. A.; Kohn, T.; Rodenburg, L. A.; Roberts, A. L. Reactivity of alkyl polyhalides toward granular iron: Development of QSARs and reactivity cross correlations for reductive dehalogenation. *Environ. Sci. Technol.* **2010**, *44*, 7928-7936.

(48) Shorter, J. *Correlation Analysis in Organic Chemistry: An Introduction to Linear Free-Energy Relationships*; Chlarendon Press: Oxford, **1973**.

(49) Brönsted, J. N.; Pederson, K. The catalytic decomposition of nitramide and its physico-chemical applications. *Z. physik. Chem.* **1924**, *108*, 185-235.

(50) Hammett, L. P. The effect of structure upon the reactions of some organic compounds. Benzene derivatives. *J. Am. Chem. Soc.* **1937**, *59*, 96-103.

(51) Hammett, L. P.; Pfluger, H. L. The rate of addition of methyl esters to trimethylamine. *J. Am. Chem. Soc.* **1933**, *55*, 4079-4089.

(52) Burkhardt, N. G.; Ford, W. G. K.; Singleton, E. The hydrolysis of arylsulfuric acids. I. *Journal of the Chemical Society* **1936**, 17-25.

(53) Brezonik, P. L. Principles of linear free-energy and structure-activity relationships and their applications to the fate of chemicals in aquatic systems. In: *Aquatic Chemical Kinetics: Reaction Rates of Process in Natural Waters*; Wiley-Interscience: New York, **1990**; pp. 113-143.

(54) Shorter, J. *Correlation Analysis of Organic Reactivity with Particular Reference to Multiple Regression*; Wiley: Chichester, England, **1982**.

(55) Marston, G.; Monks, P. S.; Wayne, R. P. Correlations between rate parameters and molecular properties. In: *General Aspects of the Chemistry of Radicals*; Wiley: Chichester, **1999**; pp. 429-471.

(56) Cramer, C. J. *Essentials of Computational Chemistry: Theories and Models*; John Wiley & Sons: Chichester, **2002**.

(57) Cramer, C. J.; Famini, G. R.; Lowrey, A. H. Use of calculated quantum chemical properties as surrogates for solvatochromic parameters in structure-activity relationships. *Acc. Chem. Res.* **1993**, *26*, 559-605.

(58) Karelson, M.; Lobanov, V. S.; Katritzky, A. R. Quantum-chemical descriptors in QSAR/QSPR studies. *Chem. Rev.* **1996**, *96*, 1027-1043.

(59) Zubatyuk, R. I.; Gorb, L.; Shishkin, O. V.; Qasim, M.; Leszczynski, J. Exploration of density functional methods for one-electron reduction potential of nitrobenzenes. *J. Comput. Chem.* **2010**, *31*, 144-150.

(60) Bylaska, E. J.; Salter-Blanc, A. J.; Tratnyek, P. G. One-electron reduction potentials from chemical structure theory calculations. In: *Aquatic Redox Chemistry*; Tratnyek, P. G.; Grundl, T. J.; Haderlein, S. B., Eds.; American Chemical Society: Washington, DC, **2011**; ACS Symposium Series, *Vol. 1071*; pp. 37-64.

(61) Uchimiya, M.; Gorb, L.; Isayev, O.; Qasim, M. M.; Leszczynski, J. One-electron standard reduction potentials of nitroaromatic and cyclic nitramine explosives. *Environ. Pollut.* **2010**, *158*, 3048-3053.

(62) Phillips, K. L.; Chiu, P. C.; Sandler, S. I. Reduction rate constants for nitroaromatic compounds estimated from adiabatic electron affinities. *Environ. Sci. Technol.* **2010**, *44*, 7431-7436.

(63) Phillips, K. L.; Sandler, S. I.; Chiu, P. C. A method to calculate the one-electron reduction potentials for nitroaromatic compounds based on gas-phase quantum mechanics. *J. Comput. Chem.* **2011**, *32*, 226-239.

(64) Scherer, M. M.; Balko, B. A.; Gallagher, D. A.; Tratnyek, P. G. Correlation analysis of rate constants for dechlorination by zero-valent iron. *Environ. Sci. Technol.* **1998**, *32*, 3026-3033.

(65) Colón, D.; Weber, E. J.; Anderson, J. L. QSAR study of the reduction of nitroaromatics by Fe(II) species. *Environ. Sci. Technol.* **2006**, *40*, 4976-4982.

(66) National Toxicology Program 11th Report on Carcinogens. In: U.S. Department of Health and Human Services, Public Health Service, National Institutes of Health, Bethesda, MD: **2005**.

(67) California Department of Public Health 1,2,3-Trichloropropane. http://www.cdph.ca.gov/certlic/drinkingwater/Pages/123TCP.aspx, **2009** (Accessed 30 November 2010).

(68) Tratnyek, P. G.; Sarathy, V.; Fortuna, J. H., Fate and remediation of 1,2,3-trichloropropane. In: *International Conference on Remediation of Chlorinated and Recalcitrant Compounds, 6th,* Monterey, CA, **2008**, Paper C-047.

(69) Bylaska, E. J.; Glaesemann, K. R.; Felmy, A. R.; Vasiliu, M.; Dixon, D. A.; Tratnyek, P. G. Free energies for degradation reactions of 1,2,3-trichloropropane from ab initio electronic structure theory. *J. Phys. Chem. A* **2010**, *114*, 12269–12282.

(70) Boronina, T.; Klabunde, K. J.; Sergeev, G. Destruction of organohalides in water using metal particles: Carbon tetrachloride/water reactions with magnesium, tin, and zinc. *Environ. Sci. Technol.* **1995**, *29*, 1511-1517.

(71) Roberts, A. L.; Totten, L. A.; Arnold, W. A.; Burris, D. R.; Campbell, T. J. Reductive elimination of chlorinated ethylenes by zero-valent metals. *Environ. Sci. Technol.* **1996**, *30*, 2654-2659.

(72) Feng, J.; Lim, T.-T. Pathways and kinetics of carbon tetrachloride and chloroform reductions by nano-scale Fe and Fe/Ni particles: comparison with commercial micro-scale Fe and Zn. *Chemosphere* **2005**, *59*, 1267-1277.

(73) Tratnyek, P. G.; Salter, A. J.; Nurmi, J. T.; Sarathy, V. Environmental applications of zerovalent metals: Iron vs. zinc. In: *Nanoscale Materials in Chemistry: Environmental Applications*; Erickson, L. E.; Koodali, R. T.; Richards, R. M., Eds.; American Chemical Society, **2010**, *Vol. 1045*; pp. 165-178.

(74) Salter, A. J.; Johnson, R. L.; Tratnyek Paul, G., Degradation of 1,2,3-trichloropropane by zero-valent zinc: Laboratory assessment for field application. In: *International Conference on Remediation of Chlorinated and Recalcitrant Compounds, 7th,* Monterey, CA, **2010**, Paper No. D-056.

(75) Zhang, X. G. *Corrosion and Electrochemistry of Zinc*; Plenum: New York, **1996**.

(76) Pourbaix, M. *Atlas of Electrochemical Equilibria in Aqueous Solutions*; National Association of Corrosion Engineers: Houston, TX, **1974**.

(77) Roetheli, B. E.; Cox, G. L.; Littreal, W. B. Effect of pH on the corrosion products and corrosion rate of zinc in oxygenated aqueous solutions. *Metals and Alloys* **1932**, *3*, 73-76.

(78) Diomidis, N.; Celis, J. P. Anodic film formation on zinc in alkaline electrolytes containing silicate and tetraborate ions. *J. Electrochem. Soc.* **2007**, *154*, C711-C718.

(79) Powers, R. W. Anodic films on zinc. *J. Electrochem. Soc.* **1969**, *116*, 1652-1659.

(80) Lehrman, L.; Shuldener, H. L. Action of sodium silicate as a corrosion inhibitor in water piping. *Indus. Eng. Chem.* **1952**, *44*, 1765-1769.

(81) Shalaby, L. A.; Abbas, H. The behaviour of zinc and zinc-silver alloys in the presence of some inhibitors. *Corros. Sci.* **1973**, *13*, 545-552.

(82) Huot, J.-Y. The effects of silicate ion on the corrosion of zinc posder in alkaline solutions. *J. Appl. Electrochem.* **1992**, *22*, 443-447.

(83) Keping, H.; Xiangrong, Y.; Jingli, F. A protective coating of silicate on zincplate. *Materials and Corrosion* **1997**, *48*, 110-112.

(84) Diomidis, N.; Celis, J.-P. Effect of hydrodynamics on zinc anodizing in silicate-based electrolytes. *Surf. Coat. Technol.* **2005**, *195*, 307-313.

(85) Dikinis, V.; Niaura, G.; Rėzaitė, V.; Demčenko, I.; Šarmaitis, R. Formation of conversion silicate films on Zn and their properties. *Trans. Inst. Met. Finish.* **2007**, *85*, 87-91.

(86) Matthess, G. *The Properties of Groundwater*; Wiley: New York, **1982**.

(87) Langmuir, D. *Aqueous Environmental Geochemistry*; Prentice-Hall, Inc.: Upper Saddle River, NJ, **1997**.

(88) Hem, J. D. *Study and Interpretation of the Chemical Characteristics of Natural Water;* 2nd ed.; U.S. Geological Survey: Washington, DC, **1970**, *Vol. 1473*.

(89) OEHHA Public Health Goals for 1,2,3-Trichloropropane in Drinking Water, Office of Environmental Health and Hazard Assesment (OEHHA), California Environmental Protection Agency. **2009**.

(90) Vega, M.; Pardo, R.; Herguedas, M. M.; Barrado, E.; Castrillejo, Y. Pseudopolarographic determination of stability constants of labile zinc complexes in fresh water. *Anal. Chim. Acta* **1995**, *310*, 131-138.

(91) Salter-Blanc, A. J.; Suchomel, E. J.; Fortuna, J. H.; Nurmi , J. T.; Walker, C.; Krug, T.; O'Hara, S.; Ruiz, N.; Morley, T.; Tratnyek , P. G. Evaluation of zerovalent zinc for treatment of 1,2,3-trichloropropane contaminated groundwater: Laboratory and field assessment. *Ground Wat. Monitor. Remed.* **2012**, *32*, 42-52.

(92) National Toxicology Program Report on Carcinogens, 12th Edition, U.S. Department of Health and Human Services, Public Health Service, **2011**.

(93) Kielhorn, J.; Könnecker, G.; Pohlenz-Michel, C.; Schmidt, S.; Mangelsdorf, I. 1,2,3-Trichloropropane, World Health Organization, Geneva, **2003**.

(94) U.S. EPA Drinking Water Contaminant Candidate List 3-Final. *Fed. Regist.* **2009**, *74*, 51850-51862.

(95) ATSDR Detailed data for the 2011 priority list of hazardous substances, Division of Toxicology and Environmental Medicine, Agency for Toxic Substances and Disease Registry, U.S. Department of Health and Human Services. **2011**.

(96) U.S. EPA Basic questions and answers for the drinking water strategy contaminant groups effort, Office of Water (4607M), U.S. Environmental Protection Agency, EPA 815-11-002, **2011**.

(97) Bosma, T.; Kruizinga, E.; DeBruin, E.; Poelarends, G.; Janssen, D. Utilization of trihalogenated propanes by Agrobacterium radiobacter AD1 through heterologous expression of the haloalkane dehalogenase from Rhodococcus sp. strain m15-3. *Appl. Environ. Microbiol.* **1999**, *65*, 4575-4581.

(98) Bosma, T.; Damborsky, J.; Stucki, G.; Janssen, D. B. Biodegradation of 1,2,3-trichloropropane through directed evolution and heterologous expression of a haloalkane dehalogenase gene. *Appl. Environ. Microbiol.* **2002**, *68*, 3582-3587.

(99) Vannelli, T.; Logan, M.; Arciero, D. M.; Hooper, A. B. Degradation of halogernated aliphatic compounds by the ammonia-oxidizing bacterium *Nitrosomonas europaea*. *Appl. Environ. Microbiol.* **1990**, *56*, 1169-1171.

(100) Pavlova, M.; Klvana, M.; Prokop, Z.; Chaloupkova, R.; Banas, P.; Otyepka, M.; Wade, R. C.; Tsuda, M.; Nagata, Y.; Damborsky, J. Redesigning dehalogenase access tunnels as a strategy for degrading an anthropogenic substrate. *Nat. Chem. Biol.* **2009**, *5*, 727-733.

(101) Yan, J.; Rash, B. A.; Rainey, F. A.; Moe, W. M. Isolation of novel bacteria within the Chloroflexi capable of reductive dechlorination of 1,2,3-trichloropropane. *Environ. Microbiol.* **2009**, *11*, 833-843.

(102) Monincová, M.; Prokop, Z.; Vévodová, J.; Nagata, Y.; Damborsky, J. Weak activity of haloalkane dehalogenase LinB with 1,2,3-trichloropropane revealed by X-ray crystallography and microcalorimetry. *Appl. Environ. Microbiol.* **2007**, *73*, 2005-2008.

(103) Pagan, M.; Cooper, W. J.; Joens, J. A. Kinetic studies of the homogeneous abiotic reactions of several chlorinated aliphatic compounds in aqueous solution. *Applied Geochemistry* **1998**, *13*, 779-785.

(104) Hunter, F. Fenton's treatment of 1,2,3-trichloropropane: chemical reaction byproducts, pathways, and kinetics. In: *Proceedings of the International Symposium on Chemical Oxidation: Technology for the Nineties*; Technomic: Lancaster, PA, **1997**, *Vol. 6*; pp. 50-71.

(105) Huang, K. C.; Zhao, Z. Q.; Hoag, G. E.; Dahmani, A.; Block, P. A. Degradation of volatile organic compounds with thermally activated persulfate oxidation. *Chemosphere* **2005**, *61*, 551-560.

(106) U.S. EPA 2011 Edition of the Drinking Water Standards and Health Advisories, Office of Water, U.S. Environmental Protection Agency: Washington, D.C., EPA 820-R-11-002, **2011**.

(107) U.S. EPA Secondary Drinking Water Regulations: Guidance for Nuisance Chemicals, Office of Water (WH-550A), U.S. Environmental Protection Agency, EPA 810/K-92-00, **1992**.

(108) Johnson, R. L.; Thoms, R. B.; O'Brien Johnson, R.; Nurmi, J. T.; Tratnyek, P. G. Mineral precipitation upgradient from a zero-valent iron permeable reactive barrier. *Ground Wat. Monitor. Remed.* **2008**, *28*, 56-64.

(109) Nurmi, J. T.; Tratnyek, P. G.; Johnson, R. L.; Thoms, R. B.; O'Brien Johnson, R., Reduction of TNT and RDX by core material from an iron permeable reactive barrier. In: *International Conference on Remediation of Chlorinated and Recalcitrant Compounds, 6th,* Monterey, CA, **2008**, *Vol.* pp. Paper M-009.

(110) Talmage, S. S.; Opresko, D. M.; Maxwell, C. J.; Welsh, C. J. E.; Cretella, F. M.; Reno, P. H.; Daniel, F. B. Nitroaromatic munition compounds: Environmental effects and screening values. *Rev. Envrion. Contam. Toxicol.* **1999**, *161*, 1-156.

(111) Juhasz, A. L.; Naidu, R. Explosives: Fate, dynamics, and ecological impact in terrestrial and marine environments. *Rev. Environ. Contam. Toxicol.* **2007**, *191*, 163-215.

(112) Anastas, P. T.; Warner, J. C. *Green Chemistry: Theory and Practice*; Oxford University Press: Oxford, **1998**.

(113) Talawar, M. B.; Sivabalan, R.; Mukundan, T.; Muthurajan, H.; Sikder, A. K.; Gandhe, B. R.; Rao, A. S. Environmentally compatible next generation green energetic materials (GEMs). *J. Hazard. Mater.* **2009**, *161*, 589-607.

(114) Huynh, M. H. V.; Hiskey, M. A.; Meyer, T. J.; Wetzler, M. Green primaries: Environmentally friendly energetic complexes. *Proc. Natl. Acad. Sci. USA* **2006**, *103*, 5409-5412.

(115) Walker, J. D. QSARs promote more efficient use of chemical testing resources—Carpe diem. *Environ. Toxicol. Chem.* **2003**, *22*, 1651-1652.

(116) Mackay, D.; Webster, E. A perspective on environmental models and QSARs. *SAR QSAR Environ. Res.* **2003**, *14*, 7-16.

(117) Gray, N. Insensitive munitions—New explosives on the horizon. In: *Army AL&T*; Defense Dept., Army, Army Material Command: **2008**, pp. 34-35.

(118) Chow, T. M.; Wilcoxon, M. R.; Piwoni, M. D.; Maloney, S. W. Analysis of new generation explosives in the presence of U.S. EPA Method 8330 energetic compounds by high-performance liquid chromatography. *J. Chromatogr. Sci.* **2009**, *47*, 40-43.

(119) Sikder, A. K.; Sikder, N. A review of advanced high performance, insensitive and thermally stable energetic materials emerging for military and space applications. *J. Hazard. Mater.* **2004**, *112*, 1-15.

(120) Millar, R. W.; Hamid, J.; Endsor, R.; Swinton, P. F.; Cooper, J. Selection and synthesis of energetic heterocyclic compounds suitable for use in insensitive explosive and propellant compositions. *Propellants, Explosives, Pyrotechnics* **2008**, *33*, 66-72.

(121) Monteil-Rivera, F.; Halasz, A.; Groom, C.; Zhao, J.-S.; Thiboutot, S.; Ampleman, G.; Hawari, J. Fate and transport of explosives in the environment: A chemist's view. In: *Ecotoxicology of Explosives*; Sunahara, G. I.; Lotufo, G.; Kuperman, R. G.; Hawari, J., Eds.; CRC Press: Boca Raton, **2009**; pp. 5-33.

(122) Strathmann, T. J. Redox reactivity of organically complexed iron(II) species with aquatic contaminants. In: *Aquatic Redox Chemistry*; Tratnyek, P. G.; Grundl, T. J.; Haderlein, S. B., Eds.; American Chemical Society: Washington, DC, **2011**; ACS Symposium Series, *Vol. 1071*; pp. 283-313.

(123) Saupe, A.; Garvens, H. J.; Heinze, L. C. S. Alkaline hydrolysis of TNT and TNT in soil followed by thermal treatment of the hydrolyzates. *Chemosphere* **1998**, *36*, 1725-1744.

(124) Emmrich, M. Kinetics of the alkaline hydrolysis of important nitroaromatic co-contaminants of 2,4,6-trinitrotoluene in highly contaminated soils. *Environ. Sci. Technol.* **2001**, *35*, 874-877.

(125) Karasch, C.; Popovic, M.; Qasim, M.; Bajpai, R. K. Alkali hydrolysis of trinitrotoluene. *Applied Biochemistry and Biotechnology - Part A Enzyme Engineering and Biotechnology* **2002**, *98-100*, 1173-1185.

(126) Felt, D. R.; Larson, S. L.; Valente, E. J. UV-VIS spectroscopy of 2,4,6-trinitrotoluene-hydroxide reaction. *Chemosphere* **2002**, *49*, 287-295.

(127) Thorn, K. A.; Thorne, P. G.; Cox, L. G. Alkaline hydrolysis/polymerization of 2,4,6-trinitrotoluene: characterization of products by ^{13}C and ^{15}N NMR. *Environ. Sci. Technol.* **2004**, *38*, 2224-2231.

(128) Bajpai, R.; Parekh, D.; Herrmann, S.; Popoviƒá, M.; Paca, J.; Qasim, M. A kinetic model of aqueous-phase alkali hydrolysis of 2,4,6-trinitrotoluene. *J. Hazard. Mater.* **2004**, *106*, 55-66.

(129) Felt, D. R.; Larson, S. L.; Hansen, L. D. Molecular weight distribution of the final products of TNT-hydroxide reaction, US Army Corps of Engineers, Engineer Research and Development Center, ERDC/EL TR-01-16, **2001**.

(130) Bernasconi, C. F. Kinetic and spectral study of some reactions of 2,4,6-trinitrotoluene in basic solution. I. Deprotonation and Janovsky complex formation. *J. Org. Chem.* **1971**, *36*, 1671-1679.

(131) Fyfe, C. A.; Malkiewich, C. D.; Damji, S. W. H.; Norris, A. R. Flow nuclear magnetic resonance investigation of the transient and stable species formed by the attack of alkoxide ions on 2,4,6-trinitrotoluene. *J. Am. Chem. Soc.* **1976**, *98*, 6983-6988.

(132) Hill, F. C.; Sviatenko, L. K.; Gorb, L.; Okovytyy, S. I.; Blaustein, G. S.; Leszczynski, J. DFT M06-2X investigation of alkaline hydrolysis of nitroaromatic compounds. *Chemosphere* **2012**, *88*, 635-643.

(133) Qasim, M. M.; Moore, B.; Taylor, L.; Honea, P.; Gorb, L.; Leszczynski, J. Structural characteristics and reactivity relationships of nitroaromatic and nitramine explosives - A review of our computational chemistry and spectroscopic research. *International Journal of Molecular Sciences* **2007**, *8*, 1234-1264.

(134) Qasim, M.; Gorb, L.; Magers, D.; Honea, P.; Leszczynski, J.; Moore, B.; Taylor, L.; Middleton, M. Structure and reactivity of TNT and related species: Application of spectroscopic approaches and quantum-chemical approximations toward understanding transformation mechanisms. *J. Hazard. Mater.* **2009**, *167*, 154-163.

(135) Valiev, M.; Bylaska, E. J.; Govind, N.; Kowalski, K.; Straatsma, T. P.; Van, D. H. J. J.; Wang, D.; Nieplocha, J.; Apra, E.; Windus, T. L.; de, J. W. A. NWChem: A comprehensive and scalable open-source solution for large scale molecular simulations. *Comput. Phys. Commun.* **2010**, *181*, 1477-1489.

(136) Hohenberg, P.; Kohn, W. Inhomogeneous electron gas. *Phys. Rev. B* **1964**, *136*, 864-871.

(137) Lee, C.; Yang, W.; Parr, R. G. Development of the Colle-Salvetti correlation-energy formula into a functional of electron density. *Phys. Rev. B* **1988**, *37*, 785-789.

(138) Becke, A. D. Density-functional thermochemistry. III. The role of exact exchange. *J. Chem. Phys.* **1993**, *98*, 5648-5652.

(139) Møller, C.; Plesset, M. S. Note on an approximation treatment for many-electron systems. *Phys. Rev.* **1934**, *46*, 618-622.

(140) Feller, D.; Schuchardt, K. *Extensible Computational Chemistry Environment Basis Set Database, Version 9/12/01*; Molecular Science Computing Facility, Environmental and Molecular Sciences Laboratory, Pacific Northwest Laboratory: Richland, Washington, USA, **2001**.

(141) Klamt, A.; Schüürmann, G. COSMO: A new approach to dielectric screening in solvents with explicit expressions for the screening energy and its gradient. *J. Chem. Soc., Perkin Trans. 2* **1993**, 799-803.

(142) Stefanovich, E. V.; Truong, T. N. Optimized atomic radii for quantum dielectric continuum solvation models. *Chem. Phys. Lett.* **1995**, *244*, 65-74.

(143) Sitkoff, D.; Sharp, K. A.; Honig, B. Accurate calculation of hydration free energies using macroscopic solvent models. *J. Phys. Chem.* **1994**, *98*, 1978-1988.

(144) Ben-Naim, A.; Marcus, Y. Solvation thermodynamics of nonionic solutes. *J. Chem. Phys.* **1984**, *81*, 2016-2027.

(145) Buncel, E.; Norris, A. R.; Russel, K. E. The interaction of aromatic nitro-compounds with bases. *Q. Rev. Chem. Soc.* **1968**, *22*, 123-146.

(146) Terrier, F. Rate and equilibrium studies in Jackson-Meisenheimer complexes. *Chem. Rev.* **1982**, *82*, 77-152.

(147) Bruckner, R. *Advanced Organic Chemistry: Reaction Mechanisms*; Hardcourt/Academic Press, **2002**.

(148) Urbanski, T. *Chemistry and Technology of Explosives*; New York: Macmillan, **1964**.

(149) Rochester, C. H. Correlation of reaction rates with acidity functions in strongly basic media Part 1. Reaction of 2,4-dinitroanisole with aqueous sodium hydroxide. *Trans. Faraday Soc.* **1963**, *59*, 2826-2828.

(150) Murto, J.; Tommila, E. The influence of the solvent on reaction velocity XXI. The reaction of 2,4-dinitrophyl alkyl ether with hydroxyl ion in water and in methanol-water and ethanol-water mixtures. *Acta Chem. Scand.* **1962**, *16*, 63-70.

(151) Kelly, C. P.; Cramer, C. J.; Truhlar, D. G. SM6: A density functional theory continuum solvation model for calculating aqueous solvation free energies of neutrals, ions, and solute–water clusters. *Journal of Chemical Theory and Computation* **2005**, *1*, 1133-1152.

(152) Zhao, Y.; Truhlar, D. G. Density functionals with broad applicability in chemistry. *Acc. Chem. Res.* **2008**, *41*, 157-167.

(153) ASTM Standard E 2552 *Standard guide for assessing the environmental and human health impacts of new energetic compounds*; ASTM International: West Conshohocken, PA, **2008**.

(154) Schwarzenbach, R. P.; Gschwend, P. M.; Imboden, D. M. Chemical transformations II: Redox reactions (Ch. 14). In: *Environmental Organic Chemistry*; 2nd ed.; Wiley: Hoboken, NJ, **2003**; pp. 555-610.

(155) Larson, R. A.; Weber, E. J. Chapter 3. Reduction. In: *Reaction Mechanisms in Environmental Organic Chemistry*; Lewis: Chelsea, MI, **1994**; pp. 169-215.

(156) Meisel, D. Free energy correlation of rate constants for electron transfer between organic systems in aqueous solutions. *Chem. Phys. Lett.* **1975**, *34*, 263-266.

(157) Tratnyek, P. G.; Hoigné, J. Kinetics of reactions of chlorine dioxide (OClO) in water. II. Quantitative structure-activity relationships for phenolic compounds. *Water Res.* **1994**, *28*, 57-66.

(158) Tratnyek, P. G. Correlation analysis of the environmental reactivity of organic substances. In: *Perspectives in Environmental Chemistry*; Macalady, D. L., Ed.; Oxford: New York, **1998**; pp. 167-194.

(159) Canonica, S.; Tratnyek Paul, G. Quantitative structure-activity relationships for oxidation reactions of organic chemicals in water. *Environ. Toxicol. Chem.* **2003**, *22*, 1743-1754.

(160) Ferry, J. L.; Glaze, W. H. Photocatalytic reduction of nitroorganics over illuminated titanium dioxide: Electron transfer between excited-state TiO2 and nitroaromatics. *J. Phys. Chem. B* **1998**, *102*, 2239-2244.

(161) Naka, D.; Kim, D.; Strathmann, T. J. Abiotic reduction of nitroaromatic compounds by aqueous iron(ll)-catechol complexes. *Environ. Sci. Technol.* **2006**, *40*, 3006-3012.

(162) Kim, D.; Duckworth, O. W.; Strathmann, T. J. Hydroxamate siderophore-promoted reactions between iron(II) and nitroaromatic groundwater contaminants. *Geochim. Cosmochim. Acta* **2009**, *73*, 1297-1311.

(163) Mukherjee, T. One-electron reduction of juglone (5-hydroxy-1,4-naphthoquinone): A pulse radiolysis study. *Radiat. Phys. Chem.* **1987**, *29*, 455-462.

(164) Ölinger, K.; Buffington, G. D.; Ernster, L.; Cadenas, E. Effects of superoxide dismutase on the automation of substituted hydro- and semi-naphthoquinones. *Chem.-Biol. Interact.* **1990**, *73*, 53-76.

(165) Naka, D.; Kim, D.; Strathmann, T. J. Abiotic reduction of nitroaromatic compounds by aqueous iron(ll)-catechol complexes. *Environ. Sci. Technol.* **2006**, *40*, 3006-3012.

(166) Eberson, L. Electron-transfer reactions in organic chemistry. *Adv. Phys. Org. Chem.* **1982**, *18*, 79-185.

(167) Evans, M. G.; Polanyi, M. Further considerations on the thermodynamics of chemical equilibria and reaction rates. *Transactions of the Faraday Society* **1936**, *32*, 1333-1360.

(168) Evans, M. G.; Polanyi, M. Inertia and driving force of chemical reactions. *Transactions of the Faraday Society* **1938**, *34*, 11-24.

(169) Perlinger, J. A.; Buschmann, J.; Angst, W.; Schwarzenbach, R. P. Iron porphyrin and mercaptojuglone mediated reduction of polyhalogenated methanes and ethanes in homogeneous aqueous solution. *Environ. Sci. Technol.* **1998**, *32*, 2431-2437.

(170) Perlinger, J. A.; Venkatapathy, R.; Harrison, J. F. Linear free energy relationships for polyhalogenated alkane transformation by electron-transfer mediators in model aqueous systems. *J. Phys. Chem.* **2000**, *104*, 2752.

(171) Ong, J. H.; Castro, C. E. Oxidation of iron(II) porphyrins and hemoproteins by nitro aromatics. *J. Amer. Chem. Soc.* **1977**, *99*, 6740-6745.

(172) Fukuzumi, S. Electron transfer chemistry of porphyrins and metalloporphyrins. In: *The Porphyrin Handbook*; Kardish, K. M.; Smith, K. M.; Guilard, R., Eds.; Academic Press: San Diego, **2000**, *Vol. 8*; pp. 115-151.

Appendix A: Supporting Information to Chapter 2[9]

A.1. Properties and Reactivity of ZVZ

Table A.1. Properties of the ZVZ used in this study.

Material	Designation	Mesh Size [1]	Specific Surface Area (m^2/g) [2]	Bulk Density (g/cm^3) [3]
Zinc Dust 64	Zn64	through 325	0.620	2.60
Zinc Powder 1210	Zn1210	20-60	0.016	2.34
Zinc Powder 1239	Zn1239	200-325	0.160	3.27

[1] Provided by manufacturer. [2] Measured by BET N_2 gas adsorption; methods given in Section 4 of this Supporting Information. [2] Measured as the mass of freely settled ZVZ occupying 10 cm^3.

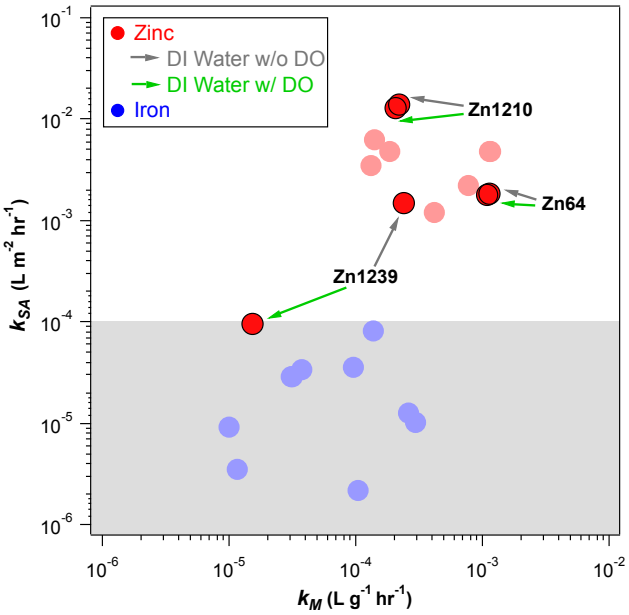

Figure A.1. Comparison of TCP degradation kinetics by industrial-grade ZVZ (this study) to rate constants obtained with reagent-grade ZVZ and reported in Sarathy et al. (*38*). Industrial-grade ZVZ included Zinc Dust 64 (Zn64), Zinc Powder 1210 (Zn1210), and Zinc Powder 1239 (Zn1239). Kinetics were measured in DI water with and without dissolved oxygen (DO). DI water was deoxygenated by sparging with either Ar or Ni gas. The gray shaded region represents values of k_{SA} that are likely too slow to be useful in field application, based on criteria presented in (*38*).

[9] Reprint of the Supporting Information to Salter-Blanc, A. J.; Tratnyek, P. G. Effects of solution chemistry on the dechlorination of 1,2,3-trichloropropane by zero-valent zinc. *Environ. Sci. Technol.* **2011**, *45*, 4073-4079 (*18*).

A.2. Effect of Ionic Strength

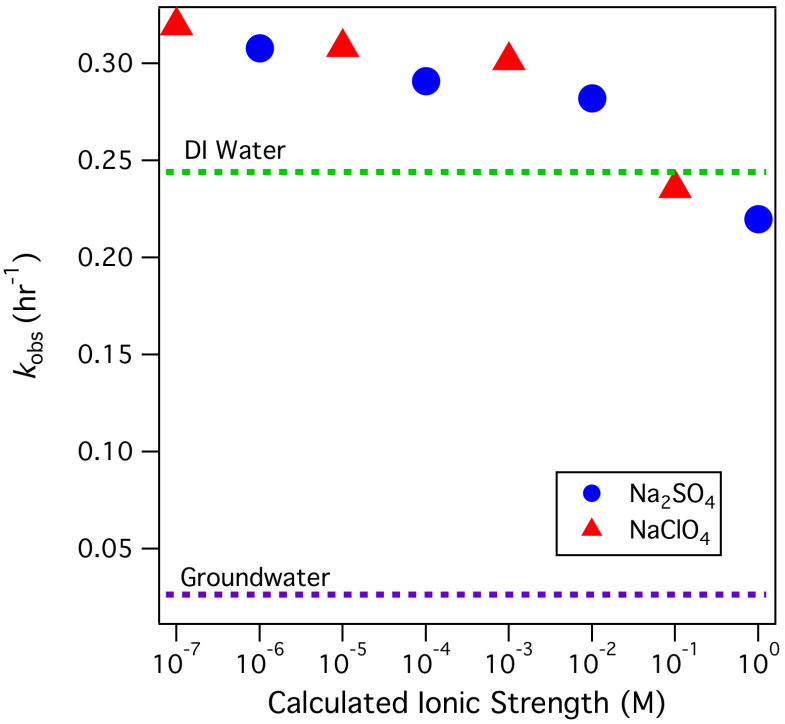

Figure A.2. Observed rate constants, k_{obs}, for TCP disappearance as measured in batch reactors containing various concentrations of $NaSO_4$ and $NaClO_4$ vs. the corresponding calculated ionic strength. Dashed lines represent the k_{obs} values measured in DI water at pH 9.7 and groundwater (SWP) at pH 9.7 (as shown in Figure 2.2).

A.3. Products of TCP Degradation

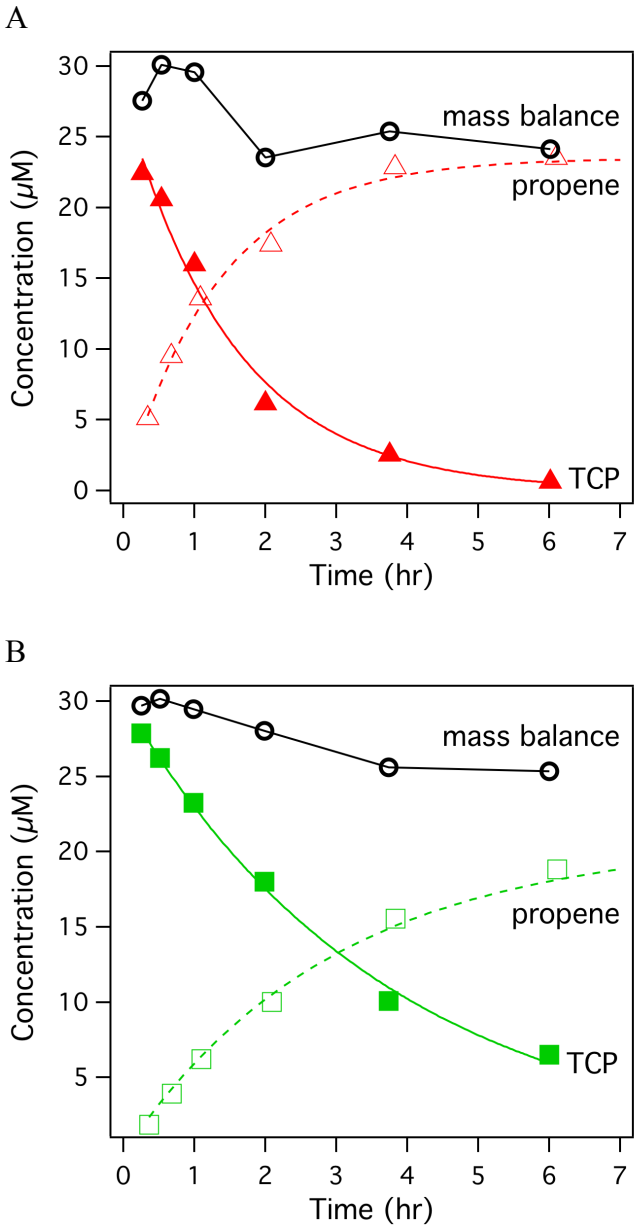

Figure A.3. Disappearance of TCP and appearance of propene using Zn64 in DI water at (***A***) pH 6.9 and (***B***) pH 8.5. Mass balance shown is based on the sum of TCP and propene concentrations. Propene concentrations were determined through direct headspace analysis of the batch reactors by gas chromatography with a GS-Q column (Agilent Technologies, Inc., Santa Clara).

A.4. Characterization of ZVZ Exposed to Solution

A.4.1. Methods

BET measurements. 100-200 mg of material, as received, was placed in a sealed BET vial and weighed (pre-drying weight). The sample in the BET vial was then placed in the VacPrep 061 in which the samples were heated under flowing UHP N_2 at 200°C. At selected times, the samples were allowed to cool and then weighed (after-drying weight). After samples were dried, surface area was measured by N_2 adsorption using a Micrometrics Gemini V surface area and pore size analyzer.

Transmission Electron Microscopy (TEM). High-resolution TEM images were collected using a JEOL JEM 2010 operated at 200 kV, as described previously (*173-175*). The point-to-point resolution of the microscope is 0.194 nm. Imaging of the ZVZ particles was done under a low electron dose in order to minimize any beam-induced damage. All images were digitally recorded using a charge-coupled device (CCD) camera and were analyzed using Gatan Digital Micrograph 3.3.1. TEM images were collected from at least 5 different locations on the grid. The elemental analysis was performed with Oxford Instruments Si(Li) EDS detector equipped with ultra thin window and Link ISIS acquisition software. The sample preparation involved mounting of the ZVZ powders onto the carbon-coated TEM grids, and immediate loading into the TEM airlock to minimize any exposure to atmospheric O_2.

X-ray Photoelectron Spectroscopy (XPS). X-ray photoelectron spectroscopy (XPS) measurements were performed using a Phi 5000 VersaProbe. This system consists of a monochromatic focused Al Kα X-ray (1486.7 eV) source and a hemispherical analyzer. The powder samples were pressed onto a stainless-steel sample-holder using

double-sided scotch tape. During the measurements, the sample-holder was isolated from the ground to avoid differential-charging. The X-ray beam of 25 W with 100 μm in diameter was incident normal to the sample and the emitted photoelectrons were collected at an emission angle of 45° relative to the sample normal. Wide scan data were collected using pass energy of 117.4 eV. High-resolution scans were obtained using pass energy of 23.5 eV. The XPS spectra were referenced to an energy scale with binding energies for Cu $2p_{3/2}$ at 932.67±0.05 eV and Au 4*f* at 84.0±0.05 eV. Low energy electrons at ~1 eV, 40 μA and low energy Ar^+ ions were used to minimize the surface charging. All the XPS spectra were charge-corrected using O 1s spectrum at 530.4eV from ZnO(0001) single crystal as a reference.

X-ray Diffraction (XRD). A Rigaku D/MAX RAPID II microdiffractometer with a curved image plate and a rotating Cr anode operating at 35 kV and 25 mA was used for the X-ray diffraction measurements. An optical prefix consisting of horizontal and vertical mirrors specific to Cr K_α radiation was employed in the incident beam to provide a focused X-rays at the sample position. At the end of the incident beam path, a 0.3 mm collimator was used to provide optimum resolution and signal to noise ratio of the diffraction patterns. The incident beam path from X-ray generator to the collimator is protected by O-ring sealed metal-tubing and it is purged with helium gas to reduce the loss of X-ray flux at the sample position. For micro-diffraction measurements, powder samples were loaded onto a 5 mm diameter with 0.3 mm depth stainless-steel sample-holder. JADE 8.5 from Materials Data Inc., and PDF4+ data base from ICSD were used to analyze X-ray diffraction data. Whole pattern fitting was used for semi-quantification of the phases.

A.4.2. Results

Table A.2. Summary of results from TEM, EDS, and XRD.

ID	Solution	pH	TEM	EDS	XRD (Zn/ZnO) weight %
1	DI Water	6.8	Non-uniform oxide layer		92.6 / 7.4
2	DI Water	9.5	Non-uniform oxide layer	ZnO crystallites	91.6 / 8.4
3	DI Water	11.9	Non-uniform oxide layer	ZnO crystallites	90.0 / 10.0
4	Groundwater (SWP)	6.8	Non-uniform oxide layer with large, needlelike crystallites	ZnO crystallites, trace levels of S, Ca	90.5 / 9.5
5	Groundwater (SWP)	9.8	Thin, compact, uniform oxide layer with oxide projections	ZnO, Ca oxides	93.3 / 6.7
6	Groundwater (SWP)	11.9	Thin, compact, uniform oxide layer with oxide projections	ZnO with increased levels of Mg	94.2 / 5.8
7	None (unexposed)	N/A	Thin, compact, uniform oxide layer	ZnO	93.9 / 6.1

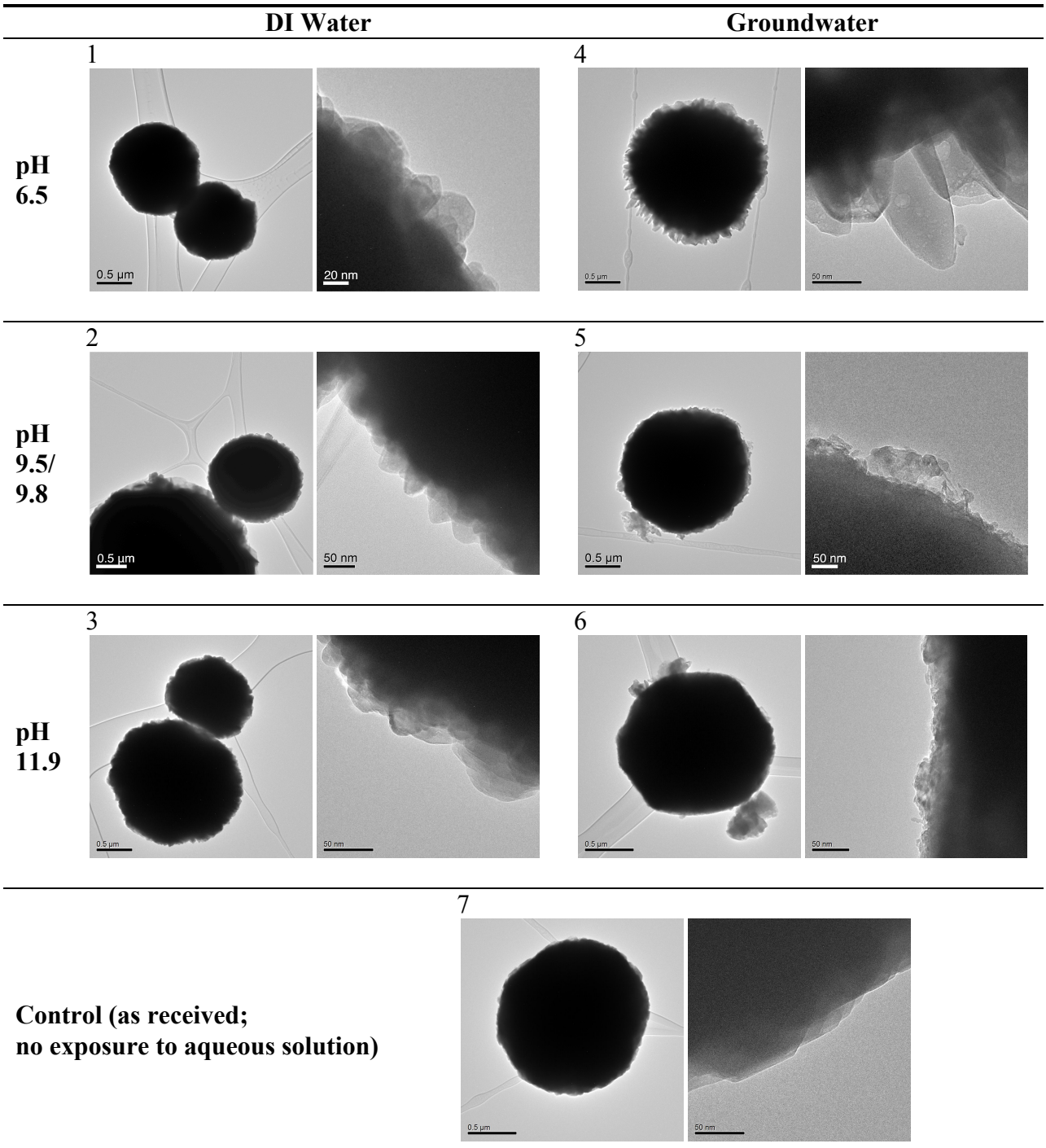

Figure A.4. TEM images of Zn64 exposed to DI water and groundwater for ~24 hr under three different pH conditions. Unexposed Zn64 (as received) shown as a control. Sample 2 was exposed to DI water at pH 9.5; Sample 5 was exposed to groundwater at pH 9.8.

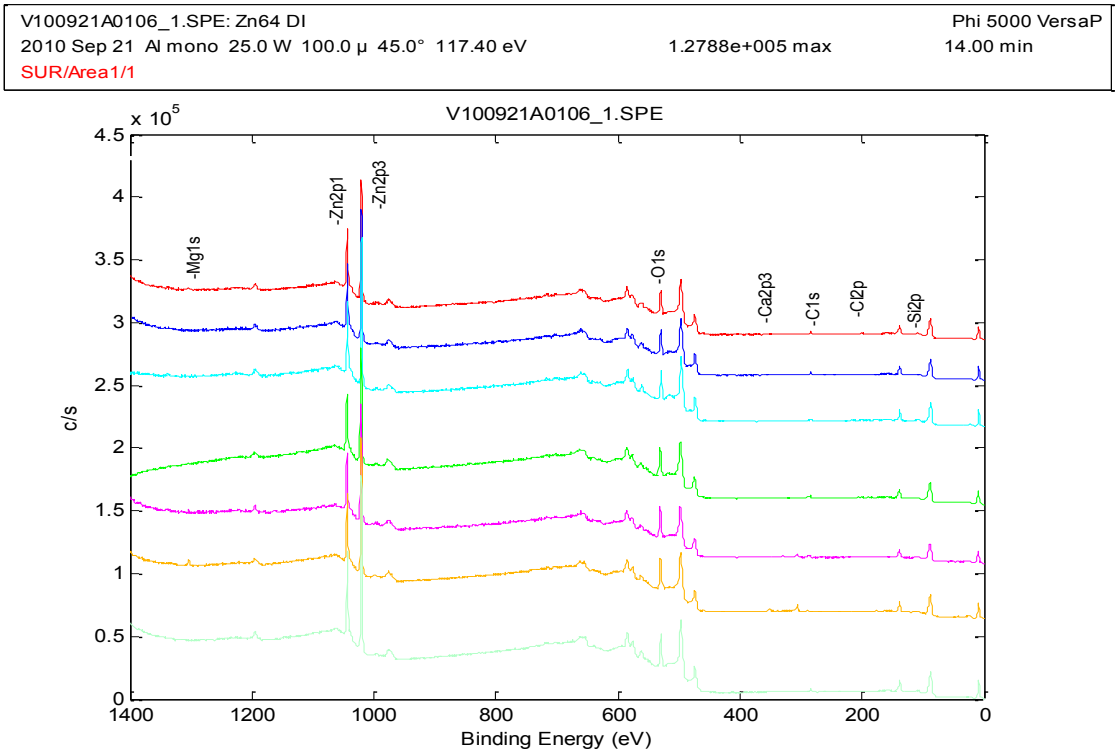

Figure A.5. XPS analysis of Zn64 exposed to DI water and groundwater for ~24 hr under three different pH regimes; results for unexposed Zn64 also shown. Spectra are ordered by sample number from top to bottom: (1) DI Water (DI), pH 6.8; (2) DI, pH 9.5; (3) DI, pH 11.9; (4) Groundwater (GW), pH 6.8; (5) GW, pH 9.8; (6) GW, pH 11.9; (7) unexposed.

Table A.3. Atomic concentrations present on the surface of DI water (DI) and groundwater (GW) exposed ZVZ as determined by XPS.

ID	Solution, pH	Zn2p3	O1s	C1s	Mg1s	Si2p	Cl2p	Ca2p
1	DI, 6.8	44.17	43.67	9.46	1	0.42	1.28	0
2	DI, 9.5	43.76	42.69	10.98	1.62	0.33	0.35	0.28
3	DI, 11.9	47.47	41.99	8.74	0.93	0.27	0.61	0
4	GW, 6.8	37.79	49.01	11.61	0.88	0.21	0.3	0.2
5	GW, 9.8	35.85	49.71	11.06	1.85	0.77	0.08	0.68
6	GW, 11.9	36.55	45.1	10.31	5.71	1.18	0.13	1.02
7	Unexposed	46.06	43.39	9.47	0.4	0.46	0.19	0.03

A.5. Effect of Groundwater Solutes

Table A.4. Summary of conditions and results of batch reactors in the presence of various solutes.

Identifier	Solute(s)	Conc.	SWP Conc. [1] (anion)	pH (initial)	pH (final)	Calculated Ionic Strength (M)	k_{obs} (h^{-1})	k_M (L g^{-1} hr^{-1})
A	NOM-GT [2]	2.5 mg/L	2.3 mg/L [3]	9.05	9.45	---	0.406	1.625×10^{-3}
B	NOM-GT [2]	10 mg/L	2.3 mg/L [3]	9.91	9.75	---	0.401	1.603×10^{-3}
C	H_3BO3	1.62×10^{-5} M	B: 171 μg/L	9.78	9.73	9.72×10^{-5}	0.368	1.470×10^{-3}
D	$CaCO_3$	1 mM	217 mg/L	9.91	9.05	1.00×10^{-3}	0.304	1.217×10^{-3}
E	NaCl	4.5 mM	~160 mg/L	9.83	9.86	4.50×10^{-3}	0.282	1.127×10^{-3}
F	DI Water	---	---	9.53	9.51	---	0.274	1.096×10^{-3}
G	$NaHCO_3$	1.67 mM	217 mg/L (as $CaCO_3$)	9.96	10.00	1.67×10^{-3}	0.271	1.083×10^{-3}
H	Na_2HPO_4	2×10^{-4} M	~0.2 mg/L	10.35	10.31	6.00×10^{-4}	0.013	5.240×10^{-5}
I	KNO_3	1 mM	<0.01 mg/L	10.46	10.46	1.00×10^{-3}	0.225	8.991×10^{-4}
J	Na_2SO_4	1.67 mM	~160 mg/L	10.09	10.01	5.01×10^{-3}	0.211	8.445×10^{-4}
K	Na_2HPO_4	2×10^{-6} M	~0.2 mg/L	9.84	9.74	6.00×10^{-6}	0.270	1.080×10^{-3}
L	DI Water w/o ZVZ	---	---	7.48	8.03	---	---	---
M	$Na_2O_3Si \bullet 9H_2O$	0.89 mM	25 mg/L	10.86	10.76	1.34×10^{-2}	0 [4]	0 [4]
N	SWP	---	---	9.79	10.12	---	0 [4]	0 [4]
O	SWQ	---	---	8.28	8.77	---	0 [4]	0 [4]
P	SWM	---	---	10.43	10.01	---	2.091×10^{-4}	8.363×10^{-7}

1. Concentration reported for Site Water P. **2**. NOM was provided by Baohua Gu (Oak Ridge National Laboratory), who obtained the raw material (NOM-GT) by reverse osmosis of brown water from a wetland pond in Georgetown, SC (*176*). NOM-GT has been characterized extensively by a variety of methods (*177-180*). The carbon content of NOM-GT is 48.3% (*181*). **3**. 3 mg/L total organic carbon. **4**. Pseudo-first-order fit gave negative k_{obs}.

A.6. Geochemical Speciation Modeling for Zn^{2+} in Solution

A.6.1. Methods

Geochemical speciation modeling was performed using the ACT subset of the Geochemist's Workbench modeling package, release 8.0 (RockWare Inc., Golden, CO) with the thermodynamic constants given in the thermo.com.v8.r6+ dataset. Speciation diagrams for groundwater were generated assuming measured Site Water P (SWP) concentrations. In the generation and interpretation of these diagrams, it was assumed that activity (α) was equal to concentration.

A.6.2 Results

Geochemical speciation modeling was performed to predict the Zn^{2+}species present at equilibrium under various solution chemistries, including DI water, SWP, and silicate solutions, over a range of pH. These model systems are similar to the Zn^{2+}-rich solutions associated with actively corroding ZVZ and give information about which solid phases are thermodynamically favored to form on the ZVZ surface under the specified assumptions. Figure A.6 shows the solubility diagrams generated for Zn^{2+} species in DI water and in groundwater. In DI water (Figure A.6A), the dominant Zn^{2+} solid phase is zincite (ZnO), which is present over a range of relevant pHs. The surface analysis described in Section A.4 of this Appendix confirms that ZnO is present on the surface. The shape of the solubility curve for ZnO is similar to the reactivity trend seen for ZVZ reduction of TCP under the same solution conditions. It is possible that, at pH values outside of about 8.5-11.5, the ZnO film covering the ZVZ dissolves to some extent, facilitating the reaction of ZVZ with TCP.

Similar speciation modeling was performed taking into consideration concentrations of groundwater solutes representative of SWP. This modeling (Figure A.6B) predicted Zn_2SiO_4, not ZnO, to be the solid Zn^+ species present at equilibrium and controlling solubility. In the SWP system, the field of solid dominance shown by Zn_2SiO_4 covers a wider range of pH and activity (α) than ZnO. This suggest that, at equilibrium, the solid phase preferentially formed by Zn^{2+} in groundwater is less soluble over a wide range of conditions than that formed in DI water. The species responsible for the formation of this alternative solid phase is silicate anion under the conditions of SWP, although additional modeling (not shown) showed that, in the absence of silicate anions, the presence of phosphate and the formation of hopeite ($Zn_3(PO)_4 \bullet H_2O$) becomes important. This latter result is consistent with the low rate constants observed for TCP degradation in the presence of certain concentrations of phosphate, although the SWP concentration of phosphate is low enough and the concentration of silicate anions is high enough, that Zn_2SiO_4 is the dominant solid.

A predominance diagram for Zn^{2+} species at various concentrations of $SiO_{2(aq)}$ (Figure A.6B) shows that Zn_2SiO_4 is the favored solid at $SiO_{2(aq)}$ concentrations (in DI water) as low as $10^{-8.5}$ M (0.2 ppb). Typical groundwater concentrations of $SiO_{2(aq)}$ range from 5-85 ppm with a median concentration of 17 ppm (*87*), suggesting that, Zn_2SiO_4, not ZnO, will control Zn^{2+} species solubility under the conditions of groundwater remediation systems.

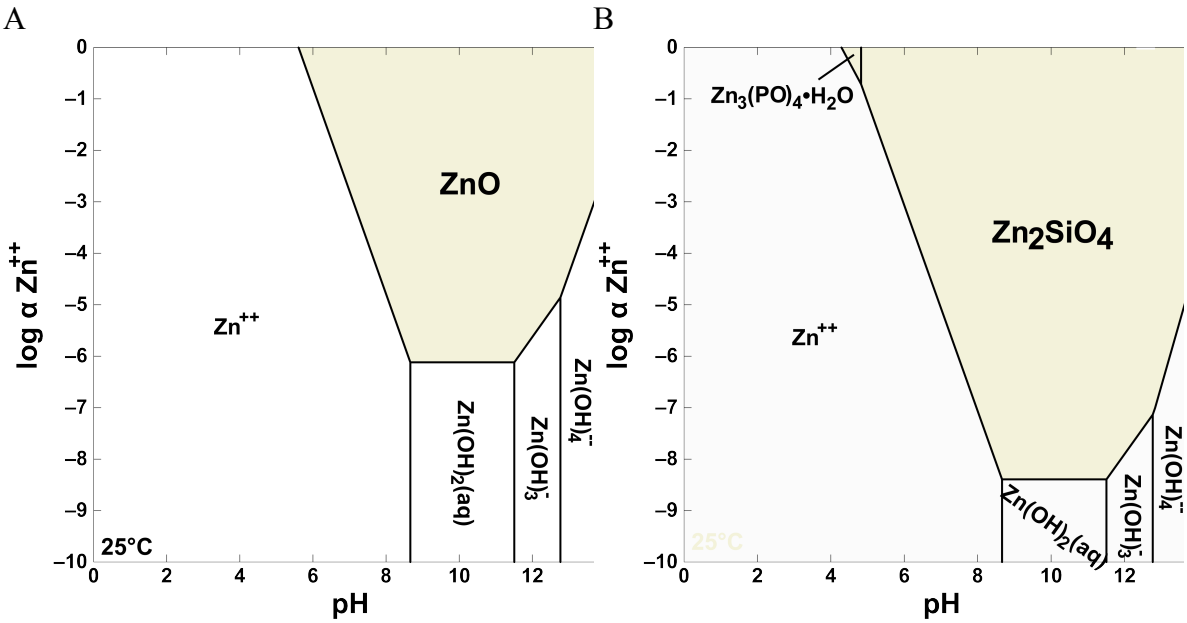

Figure A.6. Solubility of Zn^{2+} solid species in (***A***) DI water and (***B***) groundwater (assuming representative chemistry of SWP, as given in Table A.4).

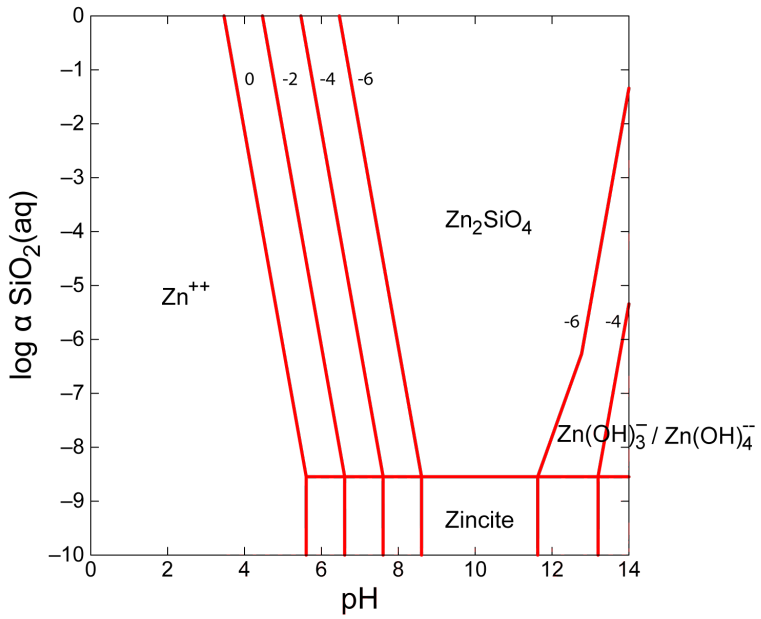

Figure A.7. Predominance diagram for Zn^{2+} species in DI water as a function of SiO_2(aq) and pH. Lines shown represent equilibrium species transitions at $[Zn^{2+}]_{Total}$ of 10^{0}, 10^{-2}, 10^{-4}, 10^{-6}.

A.7. References (Appendix A Only)

(173) Nurmi, J. T.; Tratnyek, P. G.; Sarathy, V.; Baer, D. R.; Amonette, J. E.; Pecher, K.; Wang, C.; Linehan, J. C.; Matson, D. W.; Penn, R. L.; Driessen, M. D. Characterization and properties of metallic iron nanoparticles: Spectroscopy, electrochemistry, and kinetics. *Environ. Sci. Technol.* **2005**, *39*, 1221-1230.

(174) Sarathy, V.; Tratnyek, P. G.; Nurmi, J. T.; Baer, D. R.; Amonette, J. E.; Chun, C.; Penn, R. L.; Reardon, E. J. Aging of iron nanoparticles in aqueous solution: effects on structure and reactivity. *J. Phys. Chem. C* **2008**, *112*, 2286-2293.

(175) Baer, D. R.; Tratnyek, P. G.; Qiang, Y.; Amonette, J. E.; Linehan, J.; Sarathy, V.; Nurmi, J. T.; Wang, C.; Anthony, J. Synthesis, characterization, and properties of zero-valent iron nanoparticles. In: *Environmental Applications of Nanomaterials: Synthesis, Sorbents, and Sensors*; Fryxell, G. E., Ed.; Imperial College Press: London, **2007**; pp. 49-86.

(176) Gu, B.; Schmitt, J.; Chen, Z.; Liang, L.; McCarthy, J. F. Adsorption and desorption of different organic matter fractions on iron oxide. *Geochim. Cosmochim. Acta* **1995**, *59*, 219-229.

(177) Nurmi, J. T.; Tratnyek, P. G. Electrochemical properties of natural organic matter (NOM), fractions of NOM, and model biogeochemical electron shuttles. *Environ. Sci. Technol.* **2002**, *36*, 617-624.

(178) Chen, J.; Gu, B.; LeBoeuf, E. J.; Pan, H.; Dai, S. Spectroscopic characterization of structural and functional properties of natural organic matter fractions. *Chemosphere* **2002**, *48*, 59-68.

(179) Chen, J.; Gu, B.; Royer, R. A.; Burgos, W. D. The roles of natural organic matter in chemical and microbial reduction of ferric iron. *Sci. Total Environ.* **2003**, *307*, 167-178.

(180) Chen, J.; Gu, B.; LeBoeuf, E. J. Fluorescence spectroscopic studies of natural organic matter fractions. *Chemosphere* **2003**, *50*, 639-647.

(181) Royer, R. A.; Burgos, W. D.; Fisher, A. S.; Jeon, B.-H.; Unz, R. F.; Dempsey, B. A. Enhancement of hematite bioreduction by natural organic matter. *Environ. Sci. Technol.* **2002**, *36*, 2897-2904.

Appendix B: Supporting Information to Chapter 5[1]

B.1. Summary of Kinetic Data: TNT

Table B.1. Determination of $k_{1,obs}$ and k_1 for TNT.

Concentration vs. Time Data (at different temperatures)	Determination of k_1

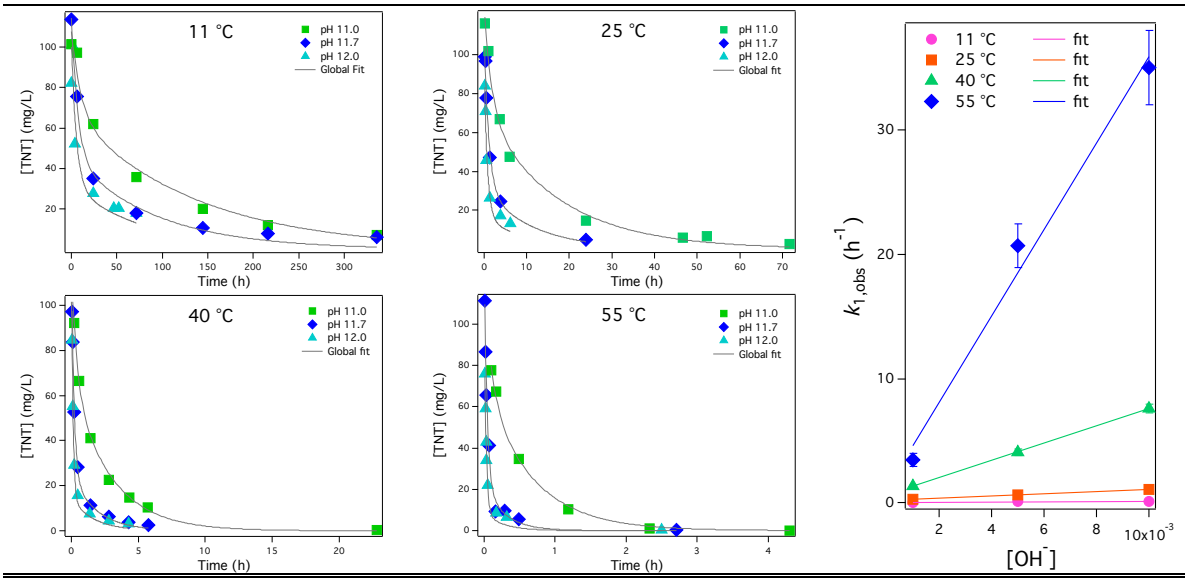

[1] Reprint of the Supporting Information to Salter-Blanc, A. J.; Bylaska, E. J.; Ritchie, J. J.; Tratnyek , P. G. Mechanisms and kinetics of alkaline hydrolysis of the energetic nitroaromatic compounds 2,4,6-trinitrotoluene (TNT) and 2,4-Dinitroanisole (DNAN). *Environ. Sci. Technol.* **2013**, *47*, 6790-6798 (*11*).

Table B.2. Summary of rate constants for TNT (obtained from fits shown in Table B.1).

Temperature (°C)	$[OH^-]$	$k_{1,obs}$ (h^{-1})	k_1 (L mol^{-1} h^{-1})	k_{-1} (h^{-1})	k_2 (h^{-1})
11	0.001	0.042 ± 0.013	9.3 ± 1.5	0.025 ± 0.017	0.0173 ± 0.0081
	0.005	0.091 ± 0.025			
	0.010	0.127 ± 0.034			
25	0.001	0.254 ± 0.044	91 ± 6.4	0.121 ± 0.038	0.121 ± 0.038
	0.005	0.672 ± 0.098			
	0.010	1.08 ± 0.17			
40	0.001	1.359 ± 0.092	690 ± 13	1.00 ± 0.17	0.69 ± 0.10
	0.005	4.04 ± 0.24			
	0.010	7.61 ± 0.35			
55	0.001	3.43 ± 0.49	3480 ± 410	3.5 ± 1.5	4.3 ± 2.1
	0.005	20.7 ± 1.8			
	0.010	35.0 ± 3.0			

B.2. Summary of Kinetic Data: DNAN

Table B.3. Determination of $k_{1,obs}$ and k_1 for DNAN.

Concentration vs. Time Data (at different temperatures)	Determination of k_1

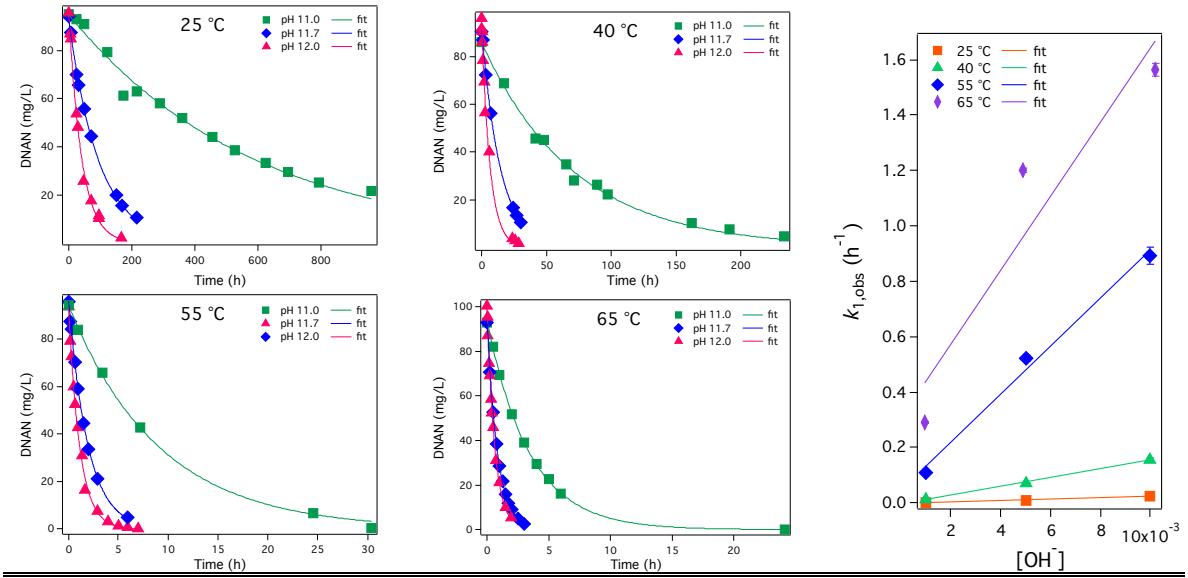

Table B.4. Summary of rate constants for DNAN (obtained from fits shown in Table B.3).

Temperature (°C)	[OH^-]	$k_{1,obs}$ (h^{-1})	k_1 (L mol^{-1} h^{-1})
25	0.001	0.001707 ± 0.000074	2.5686 ± 0.179
	0.005	0.010535 ± 0.00025	
	0.010	0.02436 ± 0.00083	
40	0.001	0.01398 ± 0.00044	15.824 ± 0.88
	0.005	0.07017 ± 0.0010	
	0.010	0.1559 ± 0.0076	
55	0.001	0.1107 ± 0.0050	86.375 ± 7.92
	0.005	0.520 ± 0.011	
	0.010	0.893 ± 0.032	
65	0.001	0.2914 ± 0.0028	133.69 ± 45.8
	0.005	1.2024 ± 0.0095	
	0.010	1.564 ± 0.023	

B.3. Summary of Free Energies Determined Using Molecular Modeling

Table B.5. Computationally-determined free energy values for the possible initial (forward) reactions of TNT and DNAN with hydroxide.

Parent	Reaction	Reaction Site	ΔG_{rxn} (kcal/mol)			$\Delta G^{\ddagger}$ (kcal/mol)		
			B3LYP	MP2	Hill et al. [a]	B3LYP	MP2	Hill et al. [a]
TNT	Meisenheimer complex formation	C1	-3.07	2.26	-14.64	22.2	28.7	14.05
		C3	-0.922	4.23	-12.13	18.0	24.9	12.29
	Direct nitro substitution	C2	-29.4	-21.5	-37.64	22.9	17.7	21.28
		C4	-26.7	-20.2	-34.56	24.8	19.3	21.60
	Proton abstraction	C0	-16.7	-5.92	-9.560	19.0	26.2	13.02
		C3	9.80	12.9	---	17.2	17.2	---
DNAN	Meisenheimer complex formation	C1	7.20	6.15	-9.440	28.5	30.2	16.19
		C3	8.69	11.0	-4.740	22.7	26.6	14.99
		C5	13.4	15.1	-2.320	27.1	30.3	16.61
		C6	39.0	31.4	26.48	39.3	33.0	30.69
	Direct nitro substitution	C2	-19.6	-12.6	-32.23	35.7	29.3	27.92
		C4	-8.92	-1.59	-23.97	38.6	32.3	30.90

a) Data reported in Hill, F. C.; Sviatenko, L. K.; Gorb, L.; Okovytyy, S. I.; Blaustein, G. S.; Leszczynski, J. DFT M06-2X investigation of alkaline hydrolysis of nitroaromatic compounds. *Chemosphere* **2012**, *88*, 635–643.

B.4. Additional Molecular Modeling of DNAN Reaction

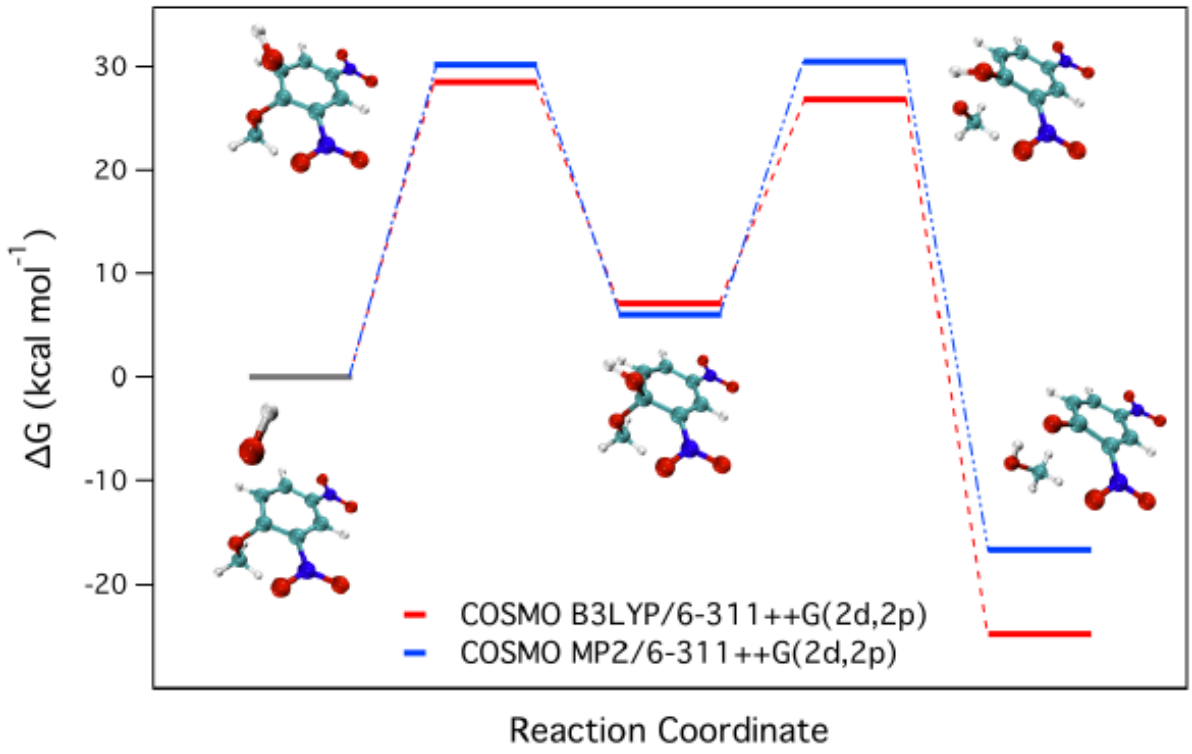

Figure B.1. Reaction coordinate diagram showing the results of a molecular modeling simulation of the reaction between DNAN and OH^- to form 2,4-dinitrophenolate (DNAN + OH^- → → 2,4-dinitrophenolate + $HOCH_3$). The observed intermediate is a Meisenheimer complex with OH addition at the C1 carbon.

Appendix C: Supporting Information to Chapter 6

C.1. Detailed Computational Methods

The first step in calculating the solution phase one-electron reduction potential is to calculate the free energy difference, ΔG_{rxn}, for the one-electron half reaction,

$$Ar\text{-NO}_{2(aq)} + 1e^-_{(g)} \rightarrow Ar\text{-NO}^{\bullet-}_{2(aq)}$$

which was directly calculated from gas phase reaction energy, entropy and solvation energy differences using electronic structure calculations, gas phase entropy estimates, and continuum solvation models. The NWChem program suite was used for these calculations. The electronic structure calculations were carried out using density functional theory (DFT) calculations using the 6-311++G(2d,2p) basis set and the LDA, PBE96, B3LYP, PBE0 and M06-2X exchange correlation functionals. In these calculations the geometries of the neutral and radical anion species were optimized and the vibrational frequencies were determined by using a finite difference approach. The free energies in the gas phase were determined using the gas-phase optimized structures and frequencies as input for free energy formula derived from statistical mechanics.

Solvation energies for solutes that do not react strongly with water can be approximated as a sum of non-covalent electrostatic, cavitation, and dispersion energies. The electrostatic contributions to the solvation energies were estimated by using the self-consistent reaction field theory of Klamt and Schüürmann (COSMO) (*141*), with the cavity defined by a set of overlapping atomic spheres with radii suggested by Stefanovich and Truong (H 1.172Å, C- 2.096Å, C= 1.635Å, O 1.576 Å, and Cl 1.750Å). The dielectric constant of water used for all of the solvation calculations was 78.4. The

cavitation and dispersion contributions to the solvation energy are less straightforward to handle because the interactions take place at short distances. Several methods have been proposed to do this (*143, 182-188*). One of the simplest approaches for estimating these terms are to use empirically derived expressions that depend only the solvent accessible surface area. In this study, the widely used formula of Sitkoff *et al.* (*143*) was used,

$$\Delta G_{cav+disp} = \gamma A + b$$

where *g* and *b* are constants set to 5 cal/mol-Å^2 and 0.86 kcal/mol respectively. Sitkoff *et al.* parameterized the constants *g* and *b* to the experimentally determined free energies of solvation of alkanes (*144*) by using a least-squares fit. The Shrake-Rupley algorithm was used to determine the solvent accessible surface areas.

The reaction energy was then converted to a redox potential using

$$E_{(abs)} = -\frac{\Delta G_{rxn}}{nF}$$

where *n* is the number of electrons transferred and F is the Faraday constant. This type of potential in electrochemistry is known as an absolute potential ($E_{(abs)}$). This type of potential is difficult to directly measure, and instead redox potentials are usually measured relative to an inert electrode, such as the standard hydrogen electrode (SHE), saturated calomel electrode (SCE), or silver/silver-chloride electrode. For measurements using the SHE this means that the free energy differences for the one-electron half reaction are reported in terms of the following overall reaction,

$$Ar\text{-NO}_{2(\text{aq})} + \frac{1}{2}H_{2(g)} \rightarrow Ar\text{-NO}^{\bullet-}_{2(\text{aq})} + H^{+}_{(aq)}$$

The SHE potential is given by

$$E_{SHE} = E_{(abs)} + E^{0}_{H}$$

where E_H^0 is the potential associated with the absolute free energy of the hydrogen electrode reaction.

$$\tfrac{1}{2}\mathrm{H}_{2(g)} \xrightarrow{\Delta G_{rxn}} \mathrm{H}^+_{(aq)} + e^-_{(g)} \qquad E_H^0 = -\frac{\Delta G_{rxn}}{F}$$

The exact value for E_H^o remains unknown despite extensive experimental and computational efforts. In this study a value of $E_H^0 = 98.6$ kcal/mol was used. This value was estimated using value of $\Delta G_s\left(\mathrm{H}^+\right) = -263.98$ kcal/mol reported by Tissandier et al., along with the gas phase values of $\Delta_f G^0\left(\mathrm{H}^+_{(g)}\right)$ and $\Delta_f G^0\left(\mathrm{H}_{2(g)}\right)$, i.e.,

$$\begin{aligned} E_H^0 &= \Delta G_s\left(\mathrm{H}^+\right) + \left(\Delta_f G^o\left(\mathrm{H}^+_{(g)}\right) - \Delta_f G^o\left(\mathrm{H}_{2(g)}\right)\right) \\ &= -263.98 \text{ kcal/mol} + 362.58 \text{ kcal/mol} \\ &= 98.6 \text{ kcal/mol} \end{aligned}$$

C.2. Data and Calculation Details for Figure 6.2

Table C.1. Data and calculation details for juglone.

NAC	E^1_{NAC} [a]	$\Delta G°'$ [b]	k_{JUG} (M^{-1} s^{-1})	log(k_{JUG})	pH (*k* measurement)
NB	-0.485 [c]	9.04	0.079	-1.1	6.79 ± 0.02
2-CH_3-NB	-0.590 [c]	11.5	0.003	-2.5	6.79 ± 0.02
3-CH_3-NB	-0.475 [c]	8.81	0.12	-0.92	6.79 ± 0.02
4-CH_3-NB	-0.500 [c]	9.39	0.051	-1.3	6.79 ± 0.02
2-Cl-NB	*-0.485* [c]	9.04	0.15	-0.82	6.79 ± 0.02
3-Cl-NB	-0.405 [c]	7.20	1.3	0.11	6.79 ± 0.02
4-Cl-NB	-0.450 [c]	8.23	0.5	-0.30	6.79 ± 0.02
2-$COCH_3$-NB	*-0.470* [c]	8.69	0.35	-0.46	6.79 ± 0.02
3-$COCH_3$-NB	*-0.405* [c]	7.20	2.5	0.38	6.79 ± 0.02
4-$COCH_3$-NB	-0.360 [c]	6.16	30	1.5	6.79 ± 0.02
TNT	*-0.300* [d]	4.77	740	2.9	6.60
2-ADNT	*-0.390* [d]	6.85	9.7	0.99	6.60
4-ADNT	*-0.430* [d]	7.77	1.2	0.079	6.60
2,4-DANT	*-0.515* [d]	9.73	0.021	-1.7	6.60
2,6-DANT	*-0.495* [d]	9.27	0.056	-1.3	6.60
4-CH_3-NB	-0.500 [d]	9.39	0.047	-1.3	6.60
4-Cl-NB	-0.450 [d]	8.23	0.48	-0.32	6.60
4-$COCH_3$-NB	-0.358 [d]	6.11	51	1.7	6.60
1,3-DNB	-0.345 [d]	5.81	61	1.8	6.60
1,4-DNB	-0.257 [d]	3.78	6900	3.8	6.60
2-NH_2-NB	*(<-0.560)* [d]		0.0023	-2.6	6.60
3-NH_2-NB	*-0.500* [d]	9.39	0.043	-1.4	6.60

a) Estimated E^1_{NAC} in italics.

b) Calculated using $E^1_{red} = E^1_7$ = -0.093.(*163*) A similar value (-0.095) has also been reported.(*164*)

c) From Schwarzenbach et al., 1990(*30*) and references cited therein.

d) From Hofstetter et al., 1999(*31*) and references cited therein.

Table C.2. Data and calculation details for lawsone.

NAC	E^1_{NAC} [a]	$\Delta G^{\circ\prime}$ [b]	k_{LAW} (M^{-1} s^{-1})	log(k_{LAW})	pH (*k* measurement)
NB	-0.485	1.61	2.4	0.38	6.98 ± 0.02
2-CH_3-NB	-0.590	4.04	0.037	-1.4	6.98 ± 0.02
3-CH_3-NB	-0.475	1.38	2.9	0.46	6.98 ± 0.02
4-CH_3-NB	-0.500	1.96	1.1	0.041	6.98 ± 0.02
2-Cl-NB	*-0.485*	1.61	2.2	0.34	6.98 ± 0.02
3-Cl-NB	-0.405	-0.231	31	1.5	6.98 ± 0.02
4-Cl-NB	-0.450	0.807	11	1.0	6.98 ± 0.02
2-$COCH_3$-NB	*-0.470*	1.27	3.3	0.52	6.98 ± 0.02
3-$COCH_3$-NB	*-0.405*	-0.231	46	1.7	6.98 ± 0.02
4-$COCH_3$-NB	-0.360	-1.27	330	2.5	6.98 ± 0.02

a) From Schwarzenbach et al., 1990(*30*) and references cited therein. Estimated E^1_{NAC} in italics.

b) Calculated using $E^1_{red} = E^1_7$ = -0.415.(*164*)

Table C.3. Data and calculation details for iron porphyrin.

NAC	E^1_{NAC} [a]	$\Delta G^{\circ\prime}$ [b]	k_{FeP} (M^{-1} s^{-1})	log($k_{Fe(II)P}$)	pH (*k* measurement)
NB	-0.485	12.7	0.96	-0.018	7.01 ± 0.02
2-CH_3-NB	-0.590	15.1	0.25	-0.60	7.01 ± 0.02
3-CH_3-NB	-0.475	12.5	1.1	0.041	7.01 ± 0.02
4-CH_3-NB	-0.500	13.0	0.67	-0.17	7.01 ± 0.02
2-Cl-NB	*-0.485*	12.6	8.8	0.94	7.01 ± 0.02
3-Cl-NB	-0.405	10.8	5.3	0.72	7.01 ± 0.02
4-Cl-NB	-0.450	11.9	2.7	0.43	7.01 ± 0.02
2-$COCH_3$-NB	*-0.470*	12.3	23.8	1.38	7.01 ± 0.02
3-$COCH_3$-NB	*-0.405*	10.8	6.3	0.80	7.01 ± 0.02
4-$COCH_3$-NB	-0.360	9.80	19.3	1.29	7.01 ± 0.02

a) From Schwarzenbach et al., 1990(*30*) and references cited therein. Estimated E^1_{NAC} in italics.

b) Calculated using $E^1_{red} = E^{1\prime}$ (one-electron reduction potential under standard environmental conditions) = 0.065.(*30*)

Table C.4. Data and calculation details for Fe(II)/tiron

NAC	E^1_{NAC} [a]	$\Delta G^{\circ\prime}$ [b]	log(k_{tiron}) (k in M^{-1} s^{-1})	pH (k measurement)
4-Cl-NB	-0.450	-5.24	4.4	5.76
4-$COCH_3$-NB	-0.360	-7.31	6.3	5.76
3-Cl-NB	-0.405	-6.27	4.9	5.76
3-CH_3-NB	-0.475	-4.66	3.8	5.76
NB	-0.485	-4.43	4.0	5.76
4-CH_3-NB	-0.500	-4.08	3.5	5.76

a) Measured at pH 7. Correction to pH 5.76 according to methods previously reported (*189*) did not significantly change the value.

b) Calculated using E^1_{red} of -0.677 V, which was determined from the following equation(*122*):

$$E^1_{red} = +0.77 - \frac{RT}{F}\ln\left(\frac{\{Fe^{2+}\}}{\{Fe^{3+}\}}\right)$$

where E^1_{red} is the non-standard, "condition-dependent" reduction potential and +0.77 is the standard one-electron reduction potential for Fe(III)/Fe(II). $\{Fe^{2+}\}$ and $\{Fe^{3+}\}$ were determined through speciation modeling performed in Geochemist's Workbench (release 8.0) with the thermo.com.v8.r6+ thermodynamic dataset with added stability constants for tiron from Naka et al., 2006.(*165*) Our speciation model appeared to deviate from that used by Naka et al. (based on comparison to Figure 3D). Comparing our model with a model produced using MINEQL+ (which agreed with Figure 3D from Naka et al., 2009) it appears the models use different stability constants for the solid phases in the system, which may be the source of disagreement.

Table C.5. Data and calculation details for Fe(II)/DFOB

NAC	E^1_{NAC} [a]	$\Delta G^{\circ\prime}$ [b]	log(k_{DFOB}) (k in $M^{-1} s^{-1}$)	pH (k measurement)
3-Cl-NB	-0.405	-1.43	2.9	9.03
4-Cl-NB	-0.450	-0.392	2.5	9.03
NB	-0.485	0.415	2.2	9.03
3-CH_3-NB	-0.475	0.184	2.1	9.03
4-CH_3-NB	-0.500	1.07	2.0	9.03

a) Measured at pH 7. Correction to pH 9.03 according to methods previously reported (*189*) did not significantly change the value.

b) Calculated using E^1_{red} of -0.480, which was determined using the equation discussed in the footnotes to Table C.4. Additional stability constants for DFOB were obtained from Kim et al., 2009.(*162*) Our speciation model appeared to accurately reproduce Figure 3B from Kim et al., 2009 suggesting agreement of our model to the model used by Kim et al.

C.3. Comparison of Calculated and Measured E^1_{NAC}

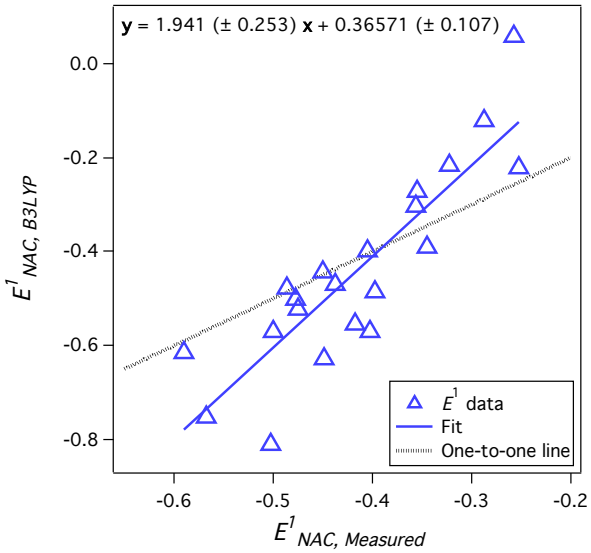

Figure C.1. Plot of E^1_{NAC} calculated at the B3LYP/6-311++G(2d,2p) level of theory plotted vs. associated measured values. A linear fit to the data is shown. The measured data were previously compiled by Phillips, et al.(*63*)

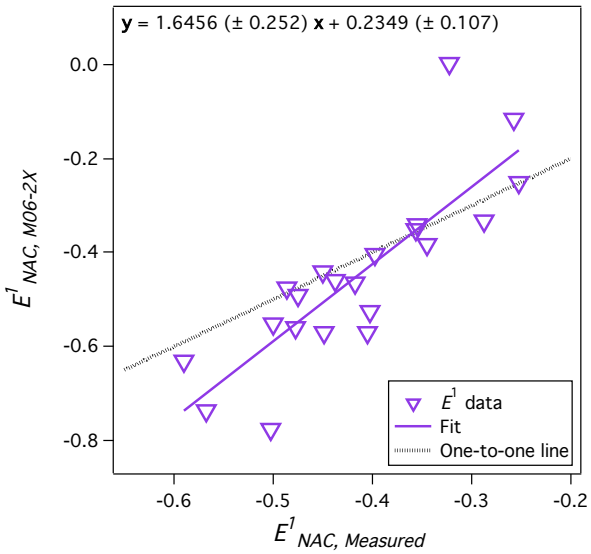

Figure C.2. Plot of E^1_{NAC} calculated at the M06-2X/6-311++G(2d,2p) level of theory plotted vs. associated measured values. A linear fit to the data is shown. The measured data were previously compiled by Phillips, et al.(*63*)

Table C.6. Determination of largest positive and negative error between calculated and measured E^{1}_{NAC}. Largest positive errors denoted with a dagger (†); largest negative errors are denoted with a double dagger (‡).

	Error (vs. Phillips Dataset) (V)						
Abbr.	**LDA**	**PBE**	**B3LYP**	**PBE0**	**M06-2X**	**B3LYP***	**M06-2X***
NB	-0.026	-0.154	0.007	-0.092	0.010	0.051	0.054
2-CH_3-NB	-0.069	-0.181	-0.026	-0.105	-0.040	0.084	0.064
3-CH_3-NB	-0.086	-0.215	-0.047	-0.127	-0.015	0.018	0.034
4-CH_3-NB	-0.094	-0.226	-0.069	-0.137	-0.052	0.019	0.021
3-Cl-NB	0.133	-0.407	0.005	-0.082	-0.166	0.011	-0.085
4-Cl-NB	-0.025	-0.149	0.006	-0.089	0.010	0.033	0.040
4-NH_2-NB	**-0.396** ‡	-0.475	-0.185	-0.295	-0.169	-0.008	-0.023
3-$COCH_3$-NB	-0.002	-0.149	-0.032	-0.101	-0.023	0.007	0.015
4-$COCH_3$-NB	0.182	0.002	0.052	-0.019	0.004	0.011	-0.001
1,2-DNB	0.320	0.127	0.166	0.049	-0.047	0.036	-0.059
1,3-DNB	-0.076	-0.236	-0.045	-0.160	-0.039	-0.044	-0.031
1,4-DNB	**0.454** †	**0.268** †	**0.316** †	**0.182** †	0.140	**0.099** †	0.043
2,4-DNT	-0.145	-0.241	-0.089	-0.221	-0.007	-0.042	0.009
2,6-DNT	0.084	-0.316	-0.167	-0.280	-0.123	-0.079	-0.060
TNT	0.021	-0.131	0.030	-0.072	0.001	-0.050	-0.043
2-CHO	0.204	0.010	0.084	-0.006	0.014	0.027	0.005
4-CHO	0.257	0.067	0.106	0.049	**0.325** †	0.023	**0.181** †
4-CH_2OH	-0.076	-0.164	-0.023	-0.146	-0.083	0.031	-0.006
2-ADNT	-0.169	-0.312	-0.137	-0.225	-0.049	-0.057	-0.009
4-ADNT	-0.258	-0.304	-0.180	-0.251	-0.122	-0.063	-0.041
2,4-DANT	-0.368	**-0.493** ‡	**-0.308** ‡	**-0.374** ‡	**-0.273** ‡	**-0.104** ‡	**-0.112** ‡

C.4. NAC Disappearance Data

Table C.7. Concentration vs. time data for the disappearance of NACs at different [FeP] and the associated k_{obs} vs. [FeP] plots used to determine k_{FeP}. In cases where only the initial portion of the concentration vs. time data was fit to the pseudo-first-order model (denoted with an asterisks (*)) a "zoomed-in" plot of the fitted data is also shown.

NAC	Conc. vs. time plot	k_{obs} vs. [FeP] plot
NB	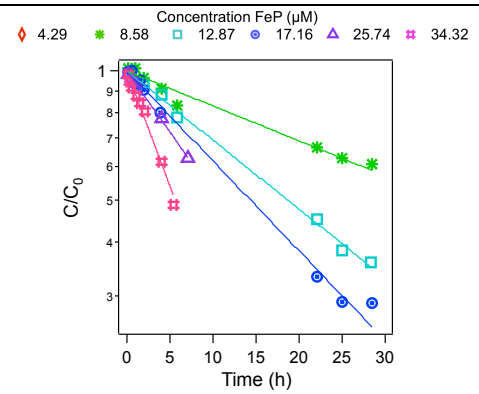	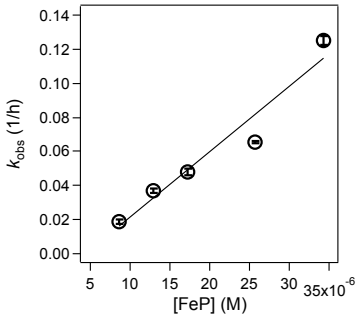
4-Cl-NB	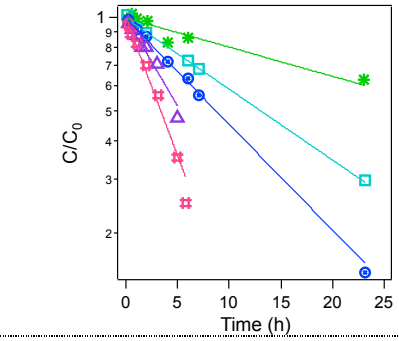	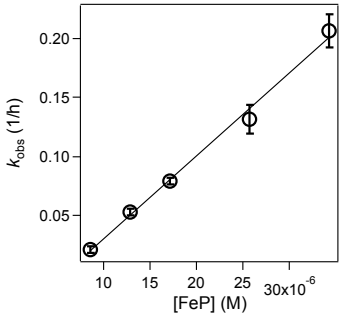
1,3-DNB*	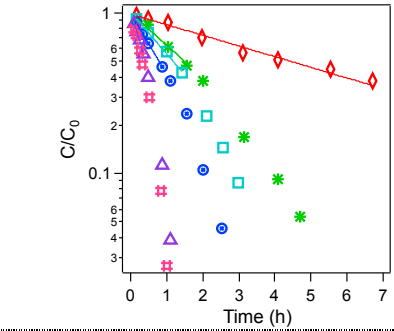	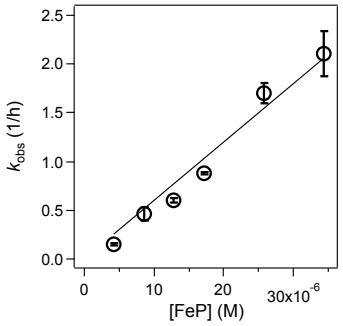

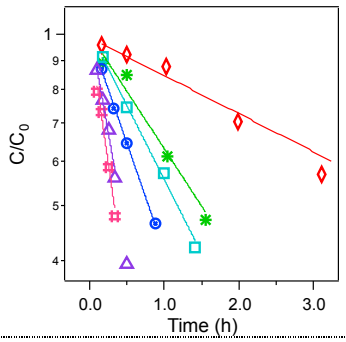

2,4-DNT

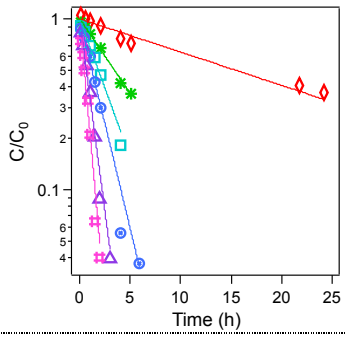

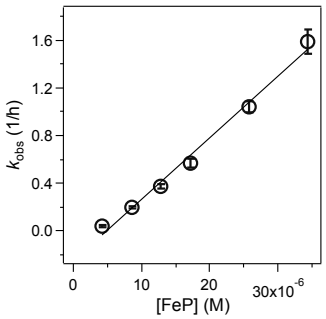

TNT*

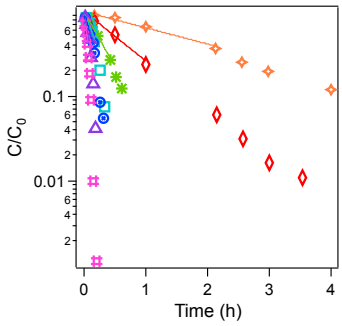

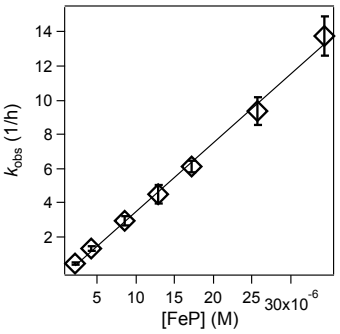

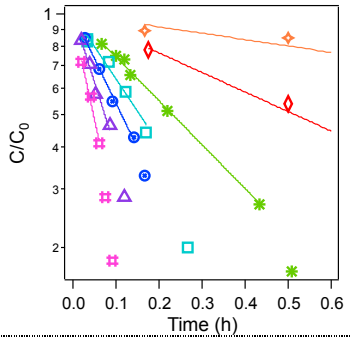

DNAN*

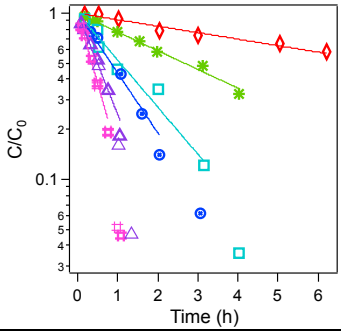

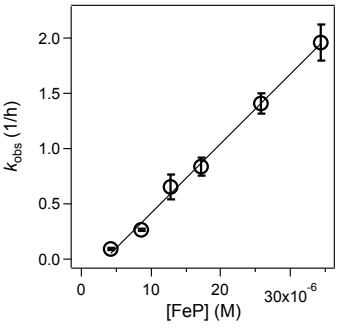

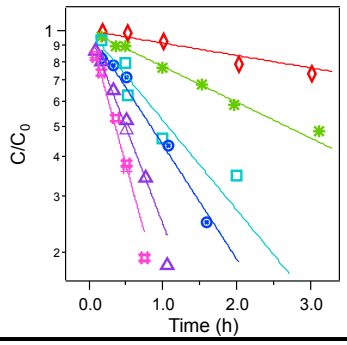
C/C0
1
9
8
7
6
5
4
3
2
0.0
1.0
2.0
3.0
Time (h)

C.5. References in Applendix C Only

(182) Pierotti, R. A. Aqueous solutions of nonpolar gases. *J. Phys. Chem.* **1965**, *69*, 281-288.

(183) Huron, M. J.; Claverie, P. Calculation of the interaction energy of one molecule with its whole surrounding. II. Method of calculating electrostatic energy. *J. Phys. Chem.* **1974**, *78*, 1853-1861.

(184) Floris, F. M.; Tomasi, J.; Pascual Ahuir, J. L. Dispersion and repulsion contributions to the solvation energy: Refinements to a simple computational model in the continuum approximation. *J. Comput. Chem.* **1991**, *12*, 784-791.

(185) Honig, B.; Sharp, K. A.; Yang, A. Macroscopic models of aqueous solutions: Biological and chemical applications. *J. Phys. Chem.* **1993**, *97*, 1101-1109.

(186) Tomasi, J.; Persico, M. Molecular interactions in solution: An overview of methods based on continuous distributions of the solvent. *Chem. Rev.* **1994**, *94*, 2027-2094.

(187) Cramer, C. J.; Truhlar, D. G. Implicit solvation models: Equilibrium, structure, spectra, and dynamics. *Chem. Rev.* **1999**, *99*, 2161-2200.

(188) Eckert, F.; Klamt, A. Fast solvent screening via quantum chemistry: COSMO-RS approach. *AIChE J.* **2002**, *48*, 369-385.

(189) Meisel, D.; Neta, P. One-electron redox potentials of nitro compounds and radiosensitizers. Correlation with spin densities of their radical anions. *J. Am. Chem. Soc.* **1975**, *97*, 5198-5203.

Biographical Sketch

Alexandra Salter-Blanc was born on October 4, 1984 in Portland, Oregon. She received a Bachelor of Arts in Chemistry from George Fox University in 2007. In 2008, she joined the laboratory of Professor Paul G. Tratnyek at the Institute of Environmental Health at Oregon Health & Science University where she has pursued the degree of Doctor of Philosophy in Environmental Science and Engineering.

Peer Reviewed Publications

Salter-Blanc, A. J.; Bylaska, E. J.; Ritchie, J. J.; Tratnyek, P. G. Mechanisms and kinetics of alkaline hydrolysis of the energetic nitroaromatic compounds 2,4,6-trinitrotoluene (TNT) and 2,4-dinitroanisole (DNAN). *Environ. Sci. Technol.* 2013, *47*, 6790-6798.

Johnson, R. L.; Nurmi, J. T.; O'Brien Johnson, G. S.; Fan, D.; O'Brien Johnson, R. L.; Shi, Z.; **Salter-Blanc, A. J.**; Tratnyek, P. G.; Lowry, G.V. Field-scale transport and transformation of carboxymethylcellulose-stabilized nano zero-valent iron. *Environ. Sci. Technol.* 2013, *47*, 1573-1580.

Salter-Blanc, A. J.; Suchomel, E. J.; Fortuna, J. H.; Nurmi, J. T.; Walker, C.; Krug, T.; O'Hara, S.; Ruiz, N.; Morley, T.; Tratnyek , P. G. Evaluation of zerovalent zinc for treatment of 1,2,3-trichloropropane contaminated groundwater: Laboratory and field assessment. *Ground Water Monit. Rem.* 2012, *32*, 42-52.

Salter-Blanc, A. J.; Tratnyek, P. G. Effects of solution chemistry on the dechlorination of 1,2,3-trichloropropane by zerovalent zinc. *Environ. Sci. Technol.* 2011, *45*, 4073-4079.

Sarathy, V.; Tratnyek, P. G.; **Salter, A. J.**; Nurmi, J. T.; Johnson, R. L.; O'Brien Johnson, G. Degradation of 1,2,3-trichloropropane (TCP): Hydrolysis, elimination, and reduction by iron and zinc. *Environ. Sci. Technol.* 2010, *44*, 787-793.

Book Chapters

Bylaska, E. J.; **Salter-Blanc, A. J.**; Tratnyek, P. G. One-electron reduction potentials from chemical structure theory calculations. In *Aquatic Redox Chemistry*; Tratnyek, P. G.; Grundl, T. J.; Haderlein, S. B., Eds.; American Chemical Society: Washington, DC, 2011; *Vol. 1071*; pp. 37-64.

Tratnyek, P. G.; **Salter-Blanc, A. J.**; Nurmi, J. T.; Amonette, J. E.; Liu, J.; Wang, C.; Dohnalkova, A.; Baer, D. R. Reactivity of zerovalent metals in aquatic media: Effects of organic surface coatings. In *Aquatic Redox Chemistry*; Tratnyek, P. G.; Grundl, T. J.; Haderlein, S. B., Eds.; American Chemical Society: Washington, DC, 2011; *Vol. 1071*; pp. 381-406.

Tratnyek, P. G.; **Salter, A. J.**; Nurmi, J. T.; Sarathy, V. Environmental applications of zerovalent metals: Iron vs. zinc. In *Nanoscale Materials in Chemistry: Environmental Applications*; Erickson, L. E.; Koodali, R. T.; Richards, R. M., Eds.; American Chemical Society, 2010; *Vol. 1045*; pp. 165-178.

Conference Proceedings Paper

Salter, A. J.; Johnson, R. L.; Tratnyek, P.G., Degradation of 1,2,3-trichloropropane by zero-valent zinc: Laboratory assessment for field application. In *7th International Conference on Remediation of Chlorinated and Recalcitrant Compounds,* Monterey, CA, 2010, Paper D-056.